

High-Resolution Analysis of F-Actin Meshwork Kinetics and Kinematics using Computational Fluorescent Speckle Microscopy

A dissertation submitted to the
SWISS FEDERAL INSTITUTE OF TECHNOLOGY ZURICH
For the degree of
Doctor of Sciences

Presented by

Aaron Christian Ponti
Dipl. Natw. ETHZ
Born 30.10.1975
Citizen of Breganzona (TI)

Accepted on the recommendation of

Prof. Dr. Gaudenz Danuser, examiner
Prof. Dr. Jonathon Howard, co-examiner
Prof. Dr. Yves Barral, co-examiner

Table of contents

TABLE OF CONTENTS	3
SUMMARY	7
SOMMARIO	9
1 INTRODUCTION	13
1.1 FUNDAMENTS OF CELL MOTILITY	14
1.1.1 <i>Cell locomotion</i>	14
1.1.2 <i>Actin</i>	15
1.1.3 <i>Protrusion is driven by actin-polymerization</i>	16
1.1.4 <i>The role of signaling on the spatial control of actin assembly</i>	18
1.1.5 <i>Stabilization of the actin meshwork</i>	20
1.1.6 <i>Cell body translocation</i>	20
1.2 FLUORESCENT SPECKLE MICROSCOPY	22
1.2.1 <i>FSM origins and fields of application</i>	22
1.2.2 <i>Quantitative FSM</i>	25
1.3 OUTLINE OF THE THESIS	25
2 COMPUTATIONAL ANALYSIS OF F-ACTIN TURNOVER IN CORTICAL ACIN MESHWORKS USING FLUORESCENT SPECKLE MICROSCOPY	27
2.1 INTRODUCTION.....	28
2.2 MATERIALS AND METHODS	29
2.2.1 <i>Software development</i>	29
2.2.2 <i>Synthesis of FSM movies using Monte Carlo simulations of dynamic F-actin meshworks</i>	29
2.2.3 <i>Cell Manipulations</i>	31
2.2.4 <i>Time-lapse Spinning Disk Confocal FSM</i>	32
2.2.5 <i>Characterization of image noise</i>	32
2.2.5.1 <i>Titration experiments</i>	32
2.2.5.2 <i>Calibration of a noise model</i>	33
2.3 ALGORITHM	33
2.3.1 <i>Noise reduction and local maximum selection</i>	33
2.3.2 <i>Statistical selection of speckles</i>	36
2.3.3 <i>Micro-movement tracking</i>	40
2.3.4 <i>Removal of time gaps in speckle trajectories</i>	41
2.3.5 <i>Classification of birth and death events</i>	42
2.3.6 <i>Kinetic analysis of birth and death events and accumulation of actin turnover maps</i>	45
2.4 RESULTS.....	48
2.4.1 <i>Verification of the algorithm on synthetic data</i>	48
2.4.2 <i>FSM analysis of cortical actin meshworks reveals cyclic polymer turnover</i>	49

2.4.3	<i>Latrunculin A perfusion induces a spreading of the cycle frequencies</i>	53
2.5	DISCUSSION	54
2.5.1	<i>FSM analysis relies on a statistical separation of significant events</i>	54
2.5.2	<i>The effect of bleaching on FSM analysis is minimal and can be eliminated completely by an appropriate correction scheme</i>	56
2.5.3	<i>The effect of focus changes</i>	59
2.5.4	<i>Local meshwork contractions are most likely to result in ghost speckles which are excluded from the analysis</i>	61
2.6	ACKNOWLEDGEMENTS	63
3	RECOVERY, VISUALIZATION, AND ANALYSIS OF ACTIN AND TUBULIN POLYMER FLOW IN LIVE CELLS: A FLUORESCENT SPECKLE MICROSCOPY STUDY	65
3.1	INTRODUCTION	66
3.1.1	<i>FSM of filamentous actin flow at the leading edge of migrating cells</i>	67
3.1.2	<i>FSM of poleward microtubule flux in mitotic spindles</i>	68
3.1.3	<i>Scope of the paper</i>	69
3.2	MATERIALS AND METHODS	70
3.2.1	<i>FSM of actin in migrating newt lung epithelial cells</i>	70
3.2.2	<i>FSM of mitotic spindle in <i>Xenopus</i> eggs extracts</i>	70
3.3	ALGORITHM	71
3.3.1	<i>Signal preconditioning</i>	71
3.3.2	<i>Particle generation</i>	71
3.3.3	<i>Particle selection</i>	71
3.3.4	<i>Generation of candidate matches</i>	72
3.3.5	<i>Selection of matches</i>	72
3.3.6	<i>Tracking with two-layer graphs</i>	74
3.3.7	<i>Tracking with three-layer graphs</i>	76
3.3.8	<i>Relaxing the condition of non-fusing and non-splitting speckles in a next version of the tracking scheme</i>	78
3.3.9	<i>Flow recovery by filtering and interpolation</i>	79
3.4	RESULTS AND DISCUSSION	80
3.4.1	<i>Performance analysis on simulated flow fields</i>	81
3.4.1.1	<i>Influence of positional fluctuations</i>	82
3.4.1.2	<i>Influence of particle appearance and disappearance</i>	82
3.4.1.3	<i>Influence of the magnitude of the displacement</i>	82
3.4.1.4	<i>Influence of anti-parallel flow</i>	83
3.4.1.5	<i>Influence of various effects applied simultaneously</i>	83
3.4.1.6	<i>Comparative evaluation</i>	83
3.4.2	<i>F-actin flow recovery in a migrating newt lung epithelial cell</i>	85
3.4.2.1	<i>Recovery of complete F-actin flow maps at the front edge of a migrating cell</i>	85
3.4.2.2	<i>F-actin flow is organized in three distinct zones</i>	87
3.4.2.3	<i>F-actin flow is dynamically modulated</i>	87

3.4.2.4	Comparison with previous kymograph analyses	88
3.4.3	<i>Recovery of microtubule flux in a mitotic spindle</i>	89
3.4.3.1	Single speckle tracking reveals bi-polar flux	90
3.4.3.2	The velocity of microtubule flux is constant along the mitotic axis	91
3.4.3.3	Histograms of the speckle number density along the mitotic axis reveal the microtubule organization and the spatial extension of the spindle poles	91
3.4.3.4	Flux in non-kinetochore microtubules is higher than in kinetochore microtubules	93
3.4.4	<i>Qualitative validation of tracking quality by speckle signal subtraction</i>	95
3.5	CONCLUSION	95
3.5.1	<i>The development of a novel tracking system was necessary to cope with the specific challenges of FSM.</i>	96
3.5.2	<i>The chosen particle tracking approach outperforms alternative, pattern-based tracking methods.</i>	96
3.5.3	<i>Single speckle tracking can reveal local polymer events and delivers extensive data for statistical analysis of cytoskeletal events.</i>	98
3.5.4	<i>The new speckle tracker overcomes the limitations of previous kymograph analyses.</i>	98
3.6	ACKNOWLEDGEMENTS	99
4	COMPUTATIONAL FLUORESCENT SPECKLE MICROSCOPY II: HIGH-RESOLUTION CO-MAPPING OF F-ACTIN FLOW AND TURNOVER IN MIGRATING CELLS	101
4.1	INTRODUCTION	102
4.1.1	<i>Organization and scope of the paper</i>	104
4.2	MATERIALS AND METHODS	105
4.2.1	<i>Cell system</i>	105
4.2.2	<i>Time-lapse spinning disk confocal FSM</i>	105
4.2.3	<i>Image analysis</i>	105
4.3	ALGORITHM	106
4.3.1	<i>Hierarchical speckle extraction</i>	106
4.3.1.1	Speckle fusions during low-pass filtering and local maximum detection	106
4.3.1.2	Hierarchical extraction of higher-order speckles	110
4.3.2	<i>Hierarchical tracking</i>	115
4.3.3	<i>Adaptive flow filtering and tracking</i>	119
4.4	RESULTS AND DISCUSSION	120
4.4.1	<i>Cell model for the analysis of the algorithmic performance</i>	120
4.4.2	<i>Hierarchical speckle extraction results in a decrease of the mean intensity and of the standard deviation of the speckle signal.</i>	121
4.4.3	<i>The role of higher-order speckles in the extraction of complete trajectories</i>	122
4.4.4	<i>Hierarchical speckle extraction increases the number of kinetic scores by 20% in spatially stationary F-actin meshworks</i>	123
4.4.5	<i>Hierarchical speckle extraction in combination with hierarchical tracking increases the number of kinetic scores by 26% in F-actin meshworks undergoing flow, and prolongs the lifetimes by 13%.</i>	125
4.4.6	<i>The role of higher-order speckles in mapping F-actin turnover</i>	126
4.4.7	<i>The role of higher-order speckles in mapping F-actin flow</i>	127

4.4.8	<i>What does the lifetime of a speckle mean?</i>	128
4.4.9	<i>The flow organization is replicated by four zones of different turnover</i>	134
4.4.10	<i>Lamellum turnover reveals peak frequencies in the power spectrum similar to those of turnover of cortical F-actin of contact-inhibited cells</i>	136
4.5	CONCLUSION	137
4.6	ACKNOWLEDGMENTS	139
5	QUANTITATIVE FLUORESCENT SPECKLE MICROSCOPY ANALYSIS OF THE DYNAMIC COUPLING OF LAMELLIPODIAL AND LAMELLAR F-ACTIN MESHWORKS	140
5.1	INTRODUCTION	141
5.2	RESULTS AND DISCUSSION	143
5.2.1	<i>Material coupling</i>	143
5.2.2	<i>Mechanical coupling</i>	146
5.2.3	<i>Perturbation experiments</i>	147
5.2.3.1	Jasplakinolide	148
5.2.3.2	Blebbistatin	148
5.3	CONCLUSION	150
6	CONCLUSION	152
6.1	SUMMARY	153
6.1.1	<i>Summary of Chapter 2</i>	154
6.1.2	<i>Summary of Chapter 3</i>	154
6.1.3	<i>Summary of Chapter 4</i>	155
6.1.4	<i>Summary of Chapter 5</i>	155
6.2	OUTLOOK	156
	REFERENCES	160
	SUPPLEMENTARY DATA	172
	ACKNOWLEDGMENTS	174
	CURRICULUM VITAE	176
	PUBLICATIONS	178

Summary

This thesis presents the development of a software package for the high-resolution analysis of F-actin (*filamentous actin*) meshwork kinetics and kinematics imaged by Fluorescent Speckle Microscopy (FSM).

FSM has emerged as the tool of choice for the analysis of the movement, assembly and disassembly dynamics of macromolecular structures *in vivo* and *in vitro*. It delivers simultaneous kinetic information in large areas of the cell, offering the capability to detect non-steady state molecular dynamics, and the ability to measure variation in dynamics of molecular systems at high spatial and temporal resolution. The full exploitation of the huge quantitative potential of this technique, however, has highly been limited by the lack of specialized software for analysis of the positional and photometric fluctuations of hundreds of thousand speckles in an FSM time-lapse series, and for translating this data into biologically relevant information.

Because of the weak and inherently stochastic nature of speckles, any measurement derived from FSM data must rely on a statistical processing, based on mathematical models, of large numbers of speckles, and this calls for fully automated, robust computational tools. This motivated us into the modeling of the speckle signal and the development of a complex algorithm to extract, track, and analyze huge numbers of speckles in FSM time-lapse series, which fluctuate in intensity, move, appear and disappear, subject to the underlying molecular processes.

In the four core chapters of this thesis, our algorithm will be presented in great detail along with the many exciting biological results and observations we have obtained from the analysis of the F-actin meshwork of both contact-inhibited and motile newt lung epithelial cells. With our software we have been able to reveal the kinetic and kinematic organization of the cortical, lamellipodial and lamellar F-actin in newt cells with unprecedented spatial and temporal resolution.

Sommaro

Questa tesi riporta lo sviluppo di un pacchetto software per l'analisi ad alta risoluzione della cinetica e cinematica della rete di actinaF (*actina fibrosa*) visualizzata mediante la tecnica detta "Fluorescent Speckle Microscopy" (FSM), letteralmente la *microscopia delle macchie fluorescenti*.

La FSM si è imposta quale tecnica preferita per l'analisi della dinamica del movimento, dell'assemblaggio e del disassemblaggio delle strutture macromolecolari *in vivo* ed *in vitro*. Essa fornisce informazioni cinetiche simultanee su ampie aree della cellula, ed offre la capacità di rilevare dinamiche molecolari lontane dallo stato di equilibrio e di misurare variazioni nella dinamica dei sistemi molecolari ad alta risoluzione, tanto spaziale quanto temporale. La carenza di software specializzato per l'analisi delle fluttuazioni nella posizione ed intensità delle centinaia di migliaia di *speckles* che caratterizzano le sequenze di immagini FSM, e per la traduzione di questi dati in informazione biologica rilevante, ha finora impedito lo sfruttamento dell'immenso potenziale quantitativo di questa tecnica.

A causa della natura stessa degli *speckles*, entità fievoli ed intrinsecamente stocastiche, qualunque misurazione ottenuta da dati FSM deve basarsi su elaborazioni statistiche, imperniate su modelli matematici, di grandi quantità di *speckles*. Ciò richiede l'impiego (e quindi, nel nostro caso, lo sviluppo) di strumenti computazionali potenti, robusti ed completamente automatizzati. Per questo motivo abbiamo modellato il segnale FSM e sviluppato un complesso algoritmo per l'estrazione, il tracking e l'analisi di grandi quantità di *speckles* che fluttuano in intensità, si muovono, appaiono e scompaiono, soggetti all'azione di processi molecolari che modificano le strutture macromolecolari sottostanti.

Nei quattro capitoli centrali di questa tesi presenteremo il nostro algoritmo dettagliatamente, così come mostreremo gli eccitanti risultati biologici e le osservazioni che abbiamo ottenuto dall'analisi della rete dell'actinaF in cellule epiteliali motili e non motili del tessuto polmonare delle salamandre. Grazie al nostro software siamo stati in grado di decifrare l'organizzazione cinetica e cinematica della rete corticale, lamellipodiale e lamellare di actinaF in questo tipo di cellule con una risoluzione spaziale e temporale mai ottenuta in precedenza.

*To Gaby,
my family,
and the pets.*

1

Introduction

1.1 Fundamentals of cell motility

1.1.1 Cell locomotion

Eucaryotic cells have the ability to organize directed movements to migrate, feed, divide, or drive internal transport of materials, converting the free energy derived from ATP hydrolysis into directed movement. One type of directional, ATP-consuming movement is the amoeboid crawling motion, mediated by the polarized assembly of a polymer (Pantaloni *et al.*, 2001). Most animal cells possess the capacity to move over or through a substrate, and cell locomotion plays a key role in both normal physiology and disease. Certain cell types are specialized for locomotion, e.g. neutrophils and free living amoebae. In many tissue cells, the capacity of locomotion is usually repressed, but can be activated by wounding or oncogenic transformation (Mitchison and Cramer, 1996). The crawling motion of animal cells involves three basic steps: formation of a lamellipodial protrusion at the front of the cell, adhesion of the lamellipodium to the substratum, and translocation forward of the cell body (Fig. 1-1). injected into fibroblasts showed that lamellipodia were the primary sites of actin incorporation (Glacy, 1983), marking them as the major “filament factory” of the cell.

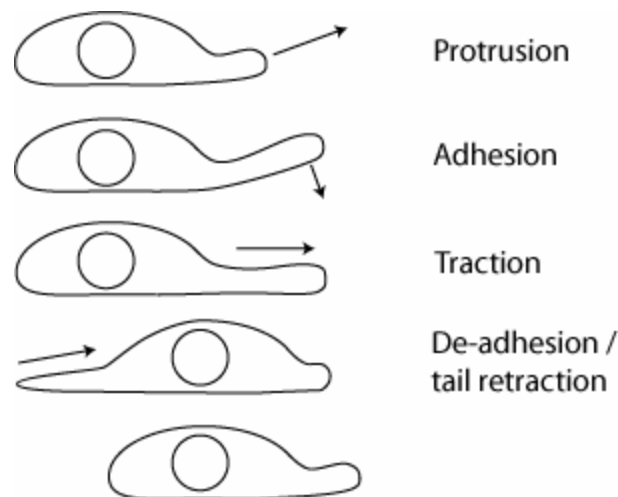


Figure 1-1

Steps of cell locomotion. Adapted from Mitchison and Cramer (1996). Detailed morphology varies between cell types, but the same basic types of motility can be distinguished.

The mechanism of amoeboid (or crawling) cell motility has been the subject of scientific scrutiny since the advent of optical microscopy. Abercrombie (1980) identified the lamellipodium, the thin layer of cytoplasm that protrudes at the front of migrating cells as the primary ‘organelle’ of motility

It is now widely accepted that the basic engine for gliding or crawling locomotion is the actin cytoskeleton (Mitchison and Cramer, 1996). In general, though, actin-based motility describes a variety of cellular processes through which living cells change shape in response to environmental signals, or extend protrusions like lamellipodia and filopodia, or wrap around a particle in a phagocytic cup (Bray and White, 1998).

1.1.2 Actin

For this subchapter, please see Albert *et al.* (2002).

Actin is the most abundant protein in many eucaryotic cells, often constituting 5% or more of the total cell protein. In vertebrate skeletal muscle cells the fraction rises to about 20%. Some lower eukaryotes, such as yeasts, have only one actin gene, encoding a single protein. All higher eukaryotes, in contrast, have several isoforms encoded by a family of actin genes: α actins are found in various types of muscles, whereas β and γ actins are the principal constituents of nonmuscle cells. Although there are subtle differences in properties in the different forms of actin, the amino acid sequences have been highly conserved in evolution, and all assemble into filaments that are essentially identical in most tests performed *in vitro*.

Each actin molecule (called *G-actin*) is a single polypeptide 375 amino acids long that has a molecule of ATP tightly associated with it. In the cell, this 43-kD globular protein is found polymerized into two-stranded helical filaments, which are known as F-actin. Actin filaments rarely occur in isolation in the cell, but rather in cross-linked aggregates and bundles, which are much stronger than the individual filaments. Indeed, single actin filaments appear in electron micrographs as thin threads about 8 nm wide, and are flexible structures.

An actin filament is a polar structure, with two structurally different ends – a relatively inert slow-growing *minus* (or *pointed*) *end* and a faster-growing *plus* (or *barbed*) *end*. The polymerization rate at the plus end of actin filaments is up to 10 times the rate at the minus end. The *critical concentration* for actin polymerization – that is, the free G-actin concentration at which the proportion of actin in polymers stops increasing – is around 0.2 μM (about 8 $\mu\text{g/ml}$). This concentration is very much lower than the concentration of unpolymerized actin in a cell, and the cell has evolved special mechanisms to prevent most of its monomeric actin from assembling into filaments (see below).

As G-actin molecules polymerizes into the polymer, they hydrolyze the terminal phosphate of their tightly bound ATP molecules, leaving the resulting ADP trapped in the polymer. This hydrolysis is not required to form the filament; instead, it serves to weaken the bonds in the polymer and thereby promote depolymerization. It is important to notice that the replacement of ADP by ATP in free G-actin monomers is relatively slow (with a half-time in the order of minutes), meaning that there is a relatively long delay before they can be reused in filament assembly. In principle, this property of actin allows the cell to maintain a high cytosolic concentration of unpolymerized actin molecules in the form of ADP actin.

Actin filaments show an interesting dynamic behavior known as *treadmilling*, which occurs when actin monomers are added continually to the plus end of the filament and are lost continually from the minus end, with no net change in filament length. This nonequilibrium behavior requires an input of energy, which is provided by the ATP hydrolysis which accompanies polymerization. Treadmilling plays a crucial role in the function of actin in motility (Alberts *et al.*, 2002).

1.1.3 Protrusion is driven by actin-polymerization

In the 1980s, it was recognized that the polarized array of actin filaments turns over rapidly in the lamellipodium subjected to treadmilling (Wang, 1985): filament barbed ends facing the cell membrane at the leading edge were growing, while pointed end were depolymerizing at the rear. Lamellipodia are not easily isolated for biochemical analysis, and *in vitro* studies and biochemical characterizations of the lamellipodium were difficult. The bacterial pathogens *Listeria monocytogenes* and *Shigella flexneri*, which exhibit actin-based movement in the host cytoplasm, have been instrumental in identifying essential factors in motility and developing biophysical assays for movement analysis (Beckerle, 1998; Cameron *et al.*, 2000). Studies performed on the “comet tail” of *Listeria* in infected cells brought the first clear evidence that actin assembly was the driving force for protrusion, and revealed the potential of *Listeria* (and *Shigella*) as models of the leading edge of the lamellipodium. The *in vitro* monitoring of *Listeria* movement in cell extracts converted a complex cell biology problem into a biochemically tractable problem, and opened the way to the full reconstruction of actin-based movement from a minimum set of purified components (Theriot *et al.*, 1994). Indeed, actin-based motility of the bacteria or of functionalized microspheres can be reconstituted *in vitro* from only five pure proteins (Pantaloni *et al.*, 2001; Wiesner *et al.*, 2003). Spatially controlled polymerization of actin is therefore at the origin of cell motility and is responsible for the formation of cellular protrusions like lamellipodia. Movement

results from the regulated site-directed treadmilling of actin filaments, consistent with observations of actin dynamics in living motile cells and with the biochemical properties of the components of the synthetic motility medium.

Still, there are major discrepancies between the well-characterized in vitro behavior of purified actin and the apparent behavior of actin filaments inside of intact, living cells (Theriot, 1997). Two of them have been particularly puzzling. First, the concentration of unpolymerized actin present in most vertebrate nonmuscle cells is ~100-fold higher than the concentration of monomeric actin that can exist at steady state in vitro. In a fibroblast, for instance, approximately 50% of the actin is in filaments and 50% is in monomer. The monomer concentration is typically 50-200 μM in a variety of cell types. This is surprisingly high, given the low critical concentration of pure actin (less than 1 μM). Second, the apparent rate of turnover of actin filaments in dynamic structures inside living cells is up to 100 times faster than can be accounted for by the in vitro turnover kinetics. These discrepancies can be explained by the presence of special proteins that bind to the actin molecule and inhibits its addition to the ends of actin filaments (Alberts *et al.*, 2002).

The *ADF/cofilin* family, which includes cofilin, destrin, depactin, actophorin, and actin depolymerizing factor (ADF), is largely responsible for the rapid turnover of actin filaments. ADF/cofilin family members are ubiquitous actin-binding protein essential in morphogenetic and motile processes. Most of them are regulated by phosphorylation in a stimulus-responsive fashion (Moon and Drubin, 1995). ADF accelerates pointed-end depolymerization, which is the rate-limiting step in treadmilling (Pantaloni *et al.*, 2001). As a result, a higher-steady state concentration of monomeric ATP-actin is established in F-actin solutions, which supports faster barbed-end growth, balancing faster pointed-end depolymerization. In enhancing treadmilling, ADF increases the rate of actin-based motility (for a review, see Carlier *et al.*, 1999).

Profilin is involved in motile processes mediated by actin polymerization (Pantaloni *et al.*, 2001; Alberts *et al.*, 2002). Profilin specifically binds ATP-monomeric actin in a complex that has the unique property of associating exclusively with barbed ends. Profilin catalyzes the ADP/ATP nucleotide exchange reaction, which is an important promoter of actin dynamics (Pollard and Cooper, 1984). The action of profilin, therefore, converts the large pool of ADF–ADP–G-actin, which undergoes association-dissociation reactions at the pointed ends, into the ATP-bound profilin-actin complex, which polymerizes at barbed ends only. The processivity of treadmilling therefore is enhanced by profilin.

β -thymosins make a complex with G-actin that does not participate in assembly at either end (Safer and Nachmias, 1994). Hence, they do not modify filament dynamics or the rate of movement (Boquet et al., 2000). These proteins are sometimes thought to buffer the free ATP-G-actin concentration. Instead, the amount of sequestered actin is determined by the value of the concentration of ATP-G-actin imposed by filament dynamics (Fechheimer and Zigmond, 1993). The changes in free ATP-G-actin elicited by regulators like ADF lead to changes in sequestered actin that are more than one order of magnitude greater. Motile cells contain a large pool of sequestered actin (Alberts *et al.*, 2002).

The capping of barbed filament ends to prevent addition or loss of actin subunits is mediated by the *heterodimeric capping protein* (Hug *et al.*, 1995; Sun *et al.*, 1995). By blocking a large fraction of the barbed ends, capping proteins funnel the flux of pointed-end depolymerization to feed the growth of a few non-capped filaments, which individually grows faster than if the other filaments were not capped (Alberts *et al.*, 2002).

Gelsolin, *villin*, *fragmin*, *adseverin*, and *scinderin* comprise a family of structurally related proteins that are able to sever actin filaments (Alberts *et al.*, 2002). These proteins bind to actin filaments, bend and cleave them in a Ca^{2+} -dependent manner, and afterwards cap the barbed filament ends. The fragmented filaments may serve as new nuclei to allow rapid repolymerization in response to further signals.

In conclusion, ADF/cofilin and capping protein cooperate in promoting fast actin-based motility. In the treadmill cycle, capping proteins are recycled after depolymerization of capped filaments and eventually cap the growing barbed ends. Maintenance of a steady number of transiently growing barbed ends requires the constant generation of barbed ends. The cellular factor that generates new filaments in a site-directed, signaling controlled fashion, is the Arp2/3 complex (Pantaloni *et al.*, 2001).

1.1.4 The role of signaling on the spatial control of actin assembly

The Arp2/3 complex has emerged as an important player in the spatially controlled initiation of actin polymerization for actin-based pathogen motility and in lamellipodium protrusion (Pantaloni *et al.*, 2001). The Arp2/3 complex is a conserved ubiquitous complex of seven polypeptides, comprising actin-related proteins Arp2 and Arp3. It stimulates actin polymerization at the surface of the bacterium when it is activated by the *Listeria* protein ActA (Welch *et al.*, 1997; 1998). While ActA of *Listeria* can activate Arp2/3 directly, *Shigella* recruits the Wiscott-Aldrich syndrome protein (WASP) family member N-WASP to activate Arp2/3 (Frischknecht and Way, 2001). For vertebrate cells, another family member,

Scar/WAVE, has been implicated in activating Arp2/3 in lamellipodium formation (Machesky *et al.*, 1998; Miki *et al.*, 1998). This is supported by the localization of Scar/WAVE at the lamellipodium tips (Hahne *et al.*, 2001; Nakagawa *et al.*, 2001). Scar/WAVE might recruit a kinase implicated in cell motility, Abelson tyrosine kinase, c-Abl, to lamellipodia (Westphal *et al.*, 2000). c-Abl interacts with Abi proteins (Abl-interacting proteins), which localize exclusively to the tip of lamellipodia (Stradal *et al.*, 2001). Another protein that accumulates at the surface of *Listeria* and at the tips of lamellipodia and filopodia is profilin, which is known to enhance the treadmilling of actin filaments *in vitro* (see above).

The assembly of actin-based membrane projections is regulated by small GTPases of the Rho family (Hall, 1998; Ridley, 2001). They are synthesized as cytosolic proteins but can be targeted to membranes by a series of posttranslational modifications (Michaelson *et al.*, 2001). Two members of this family, Rac1 and Cdc42, signal the formation of lamellipodia and filopodia, respectively (Nobes and Hall, 1995). The activation of Rac and Cdc42 can be mediated by stimulation of both growth factor (Hall, 1998) and integrin (Price *et al.*, 1998) receptors and requires GEFs (GDP-GTP exchange factors), many of which have been described (Van Aelst and D'Souza-Schorey, 1997; Scita *et al.*, 2000). General membrane localization cannot explain the focal induction of lamellipodia or filopodia at the cell periphery. Indeed, activated Rac has been shown to accumulate in membrane ruffles upon growth factor stimulation (Kraynov *et al.*, 2000). Upon ligand binding, growth factor-receptors can activate phosphoinositide 3-kinases, a product of which, phosphatidylinositol (3,4,5)-trisphosphate, in turn activates GEFs such as Vav and Sos (Scita *et al.*, 2000). GEFs appear to be present at the site of actin assembly (Kranewitter *et al.*, 2001).

Potential pathways for the transduction of signals from active Rac and Cdc42 to actin polymerization into lamellipodia and filopodia have been uncovered. Of the many effector proteins that interact specifically with GTP-Cdc42, only the hematopoietic Wiscott-Aldrich syndrome protein (WASP) and its ubiquitous family member N-WASP provide a direct link to actin assembly through activation of the nucleating activity of the Arp2/3 complex (Pantaloni *et al.*, 2001). While N-WASP and Cdc42 display direct interaction, Scar/WAVE and Rac are linked by the insulin receptor substrate Irs53 (Miki *et al.*, 2000).

Another signaling pathway implicated in lamellipodium formation involves the p21-activated kinase (PAK) family. These serine/threonine kinases were identified as direct downstream effectors of Rac and Cdc42 (Daniels and Bokoch, 1999; Bagrodia and Cerione, 1999).

1.1.5 Stabilization of the actin meshwork

Actin polymerization at the lamellipodium tip must be tightly coupled to the establishment of molecular linkages that constrain the generated actin filaments within a membrane sheet, through filament-filament and filament-membrane interactions. Emphasis has recently been placed on the possible role of the Arp2/3 complex in initiating and structuring actin networks. *In vitro* experiments have shown that Arp2/3 can promote the branching of actin filaments (but conflicting models have been proposed for how this occurs: see Pantaloni *et al.*, 2000; Blanchoin *et al.*, 2000), and evidence for the *in vivo* relevance of filament branching by Arp2/3 has been extracted from appealing images of lamellipodium meshworks prepared for electron microscopy imaging (Svitkina *et al.*, 1999). Accordingly, a dendritic-branching model of actin-based protrusion has been widely accepted (Svitkina *et al.*, 1999; Borisy and Svitkina, 2000). Candidates for actin network stabilization are cortactin (Weaver *et al.*, 2001; Zettl and Way, 2001; Kaksonen *et al.*, 2000) and Abp1 (Goode *et al.*, 2001, Kessels *et al.*, 2000), which have been shown to bind and activate Arp2/3, and the classical actin crosslinking proteins filamin (Cunningham *et al.*, 1992) and α -actinin (Langanger *et al.*, 1984). Evidence suggests that filamin can bind to transmembrane proteins and thus could serve as a linker between the membrane and the cytoskeleton to recruit signaling proteins (e.g. small GTPases) to the vicinity of sites of actin polymerization and remodeling (Van der Flier and Sonnenberg, 2001).

1.1.6 Cell body translocation

Actin filaments grow at their plus end providing the force for protrusion. Polymerized domains, however, do not move forward relative to the substratum. In contrast, major components of the cell body, such as the nucleus and other organelles actually move forward. Consequently, translocation of the cell body requires elements in addition to protrusion.

In general, cell motility is based on actin and myosin and is reasonable to consider that actin-dependent motor proteins may generate forces contributing to the translocation of the cell body relative to the lamellipodium. If such forces exist, translocation of the cell body may occur even in the absence of lamellipodial protrusion. This was actually demonstrated for fish epidermal keratocytes, where the cell body continued to move forward after protrusion was blocked with cytochalasin (Anderson *et al.*, 1996).

The same forces that drive the cell body forward relative to the lamellipodium and to the substratum, are expected to produce a retrograde flow of lamellipodial components relative to the substratum, if the cell body, for any reason, could not move forward. This in

principle explains the phenomenon of F-actin retrograde flow (Abercrombie *et al.*, 1972; Small, 1981; Wang, 1985; Forscher and Smith, 1988; Danuser and Oldenbourg 2000, Waterman-Storer *et al.*, 2002). The myosin involved in cell translocation appears to be myosin II (Cheney *et al.*, 1993; Goodson, 1994). There are two fundamentally distinct models for how myosin II may generate traction force (Mitchison and Cramer, 1996). The *transport model* suggests that cell movement results from polar organization of actin filaments which function like railroad track, with their barbed ends oriented in the direction of translocation. Myosin II would then travel along these tracks, providing the force to for the translocation of the cell body, to which it is mechanically connected. The contractile model holds that myosin II interacts with actin filaments to produce contraction in the cell. In this model, directional translocation is explained not by the polarity of actin itself but by a non-uniform distribution of contractile force and/or strength of cell adhesion to the substratum. Unlike the transport model, the extent of translocation of individual myosin molecules could be small compared to the size of the cell, but being multiplied by the number of contractile elements, it could result in a sufficient magnitude for cell body movement.

Verkhovsky *et al.*, (1999a) studied the actin-myosin II machinery in cell a translocation and retrograde flow in two model systems: mammalian fibroblasts and fish epidermal keratocytes. They observed aggregation of myosin II filaments into clusters and proposed a network contraction model, where myosin clusters embedded in the actin network are the tension generation units. The cell body is attached to the actin-myosin network at the transition with the lamellum/lamellipodium (the *convergence zone*), either directly or through other cytoskeletal structures (e.g. intermediate filaments). Consequently, compression of the actin-myosin network in the forward direction pulls along the cell body.

Retrograde flow is a necessary consequence of the contractile force between the lamellum/lamellipodium and the cell body. In locomoting keratocytes, the lamellipodium is attached to the substratum more strongly than is the cell body, thus contraction of the network in the convergence zone moves the cell body forward relative to the stationary lamellipodium and there is therefore no retrograde flow of cytoskeletal components. In fibroblasts, contraction of network could also participate in retrograde flow. Both in locomoting and stationary cells, retrograde flow delivers newly assembled contractile elements from the cell periphery to their site of action. Contraction of these elements, in turn, drives the flow which brings new contractile elements to fuel contraction. Thus, contraction becomes a self-supporting process and flow provides the logical link between the assembly and function of the contractile machinery.

1.2 Fluorescent speckle microscopy

1.2.1 FSM origins and fields of application

Fluorescent speckle microscopy (Waterman-Storer *et al.*, 1998) is derived from fluorescent analog cytochemistry, in which a fluorescently labeled protein is introduced into cells and incorporates into macromolecular structures, rendering them fluorescent and amenable to analysis by video or time-lapse microscopy (Wang *et al.*, 1982). When a high percentage (>10%) of subunits in a cell bear fluorescent tags, their incorporation into the polymer is relatively even, with the result that the polymeric structures appear to be uniformly labeled. This approach is limited in its ability to report protein dynamics because of high background fluorescence from unincorporated and out-of-focus incorporated fluorescent subunits and the difficulty in detecting movement or turnover of subunits because of the uniform labeling of fluorescent structures in microscope images. These problems have been partially alleviated by technically cumbersome laser photo-bleaching and photo-activation of fluorescence to mark structures in limited cell areas and measure the movement and subunit turnover in the mark at steady state (Mitchison, 1989; Theriot and Mitchison, 1991; Wadsworth and Salmon, 1986; Wang, 1985; Wolf, 1989).

FSM provides similar information to photomarking techniques. However, it can deliver simultaneous kinetic information from large areas of the cell, offers the capability to detect non-steady state molecular dynamics, and can measure variation in molecular dynamics at high spatial resolution. In addition, FSM significantly reduces out-of-focus fluorescence and improves the visibility of fluorescently labeled structures and their dynamics in thick specimens (Waterman-Storer and Salmon, 1999).

In FSM, the random incorporation of low percentages of tagged molecules (<1%) produces a discontinuous pattern, which can then be used to determine whether the polymer is stationary or translocating. Such a discontinuous labeling of filamentous structures had previously been noted *in vitro*, in studies in which actin filaments were doped with small amounts of labeled subunits (Sase *et al.*, 1995), but it was not until (Waterman-Storer and Salmon, 1997) noted unevenly-labeled microtubules (MTs) in the lamella of migrating epithelial cells (Fig. 1-2 (a)) and realized their value as fiduciary marks that FSM began to be used *in vivo*.

To understand the origin of speckles, Waterman and Storer (1998) developed a stochastic growth model for the origin of the fluorescent speckle pattern in light micrographs of MTs. Microtubules assemble from tubulin dimers into 25 nm wide polymers containing

1625 dimers per micron of microtubule (Desai and Mitchison, 1997; Fig. 1.2 (b)). The image of a microtubule assembled from a mixture of fluorescent and non-fluorescent dimers is a convolution of the fluorophore distribution along the microtubule with the point-spread function (PSF) of the microscope. The size of the PSF for standard fluorophores is determined by the numerical aperture of the objective lens (NA), minimally a radius of 240–270 nm using the highest NA lenses available. Within this diffraction-limited 250 nm image region are ~450 tubulin dimers, some fraction (f) of which will be fluorescent, giving a mean number of fluorescent dimers ($450 \cdot f$) per PSF. In FSM images, the speckle pattern along the microtubule is produced by variations in the number of fluorescent dimers per PSF (Waterman-Storer and Salmon, 1998). The contrast of the speckle pattern increases with lowering f . As seen in Fig. 1-2 (c), microtubules assembled from a low fraction of fluorescent tubulin ($f = 1.25\%$) appear speckled in high-resolution images, while microtubules assembled from higher fractions ($f = 20\%$) of labeled tubulin appear continuously labeled (Waterman-Storer and Salmon, 1998).

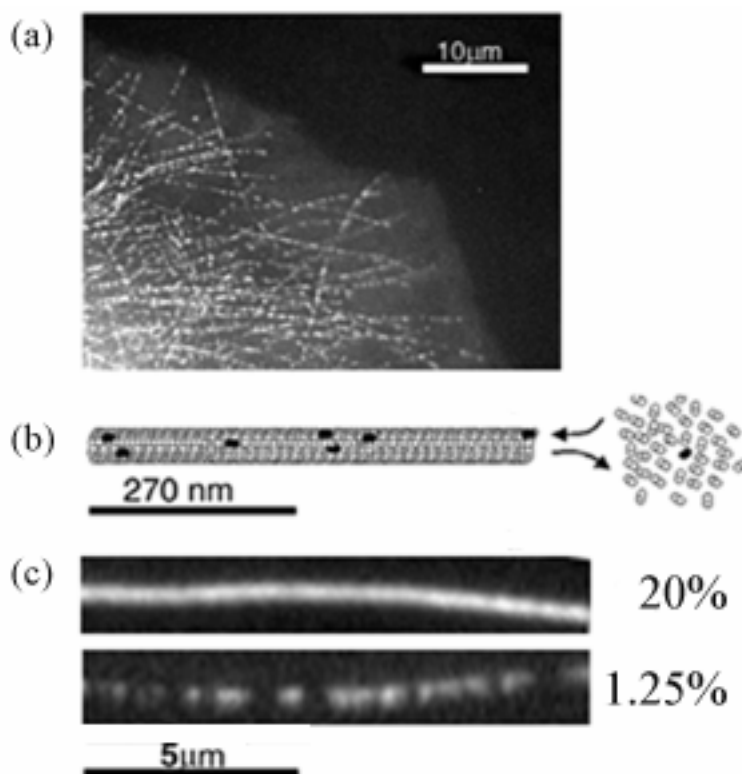


Figure 1-2

How microtubules get fluorescent speckles in vivo and in vitro. Adapted from Waterman-Storer and Danuser, 2002. (a) Microtubule FSM image of the lamella of a migrating newt lung epithelial cell. (b) Microtubule co-assembly from a pool of very few fluorescently labeled (black) tubulin dimers and many unlabeled (white) dimers. The limit of resolution for X-rhodamine fluorescence is shown to scale. (c) Microtubules assembled in vitro from purified tubulins; the percentage labeled tubulin is shown. Microtubules assembled from 1.25% labeled tubulin appear speckled, while those assembled from 20% labeled tubulin do not.

In theory, optimal contrast is obtained when speckles represent the diffraction-limited image of a single fluorophore (Watanabe and Mitchison, 2002; Waterman-Storer and Salmon, 1999). In practice, however, lower bounds for the fraction f are determined by two factors: the imaging parameters, including noise level, sensitivity of the camera, stability of the microscope, and dynamics of the observed process, which all may reduce the ability to detect single fluorophores. And secondly, fractions that are too low result in a very low density of speckles, and thus a reduction in the spatial and temporal sampling rate of events.

FSM initially used conventional wide-field epifluorescence light microscopy and digital imaging with a cooled charge-coupled-device (CCD) (Waterman-Storer and Salmon, 1997). Since then, FSM has been applied to interesting questions about cytoskeletal function during cell motility, neuronal path-finding and mitosis, and has given insight into cytoskeletal dynamics *in vitro*. For instance, when injected with low level of fluorescently labeled actin, actin-rich structures such as the lamellipodium of migrating cells appear speckled in high-resolution fluorescence images (Waterman-Storer *et al.*, 1998, 2000a; Verkhovsky *et al.*, 1999b; Watanabe and Mitchison, 2002). In contrast to what had been observed for the formation of speckles in the MT lattice, actin speckles form in a different way. For actin, the lamellipodium is filled with a cross-linked and dense 3-dimensional meshwork of actin filaments, and each filament is made up of a paired helix of 360 actin monomers per micron (Pollard *et al.*, 2000; Small, 1981; Svitkina *et al.*, 1997). Here, a fluorescent speckle may arise from fluorescently labeled actin monomers within multiple actin filaments of the meshwork falling into the same PSF volume; however, none of the filaments are detected individually. Thus, the entire meshwork appears as a relatively even distribution of fluorescent speckles in images. The ability to observe speckles without resolving individual filaments has made FSM useful for studies of actin movement.

Perhaps one of the more powerful applications of FSM has been in the study of MT flux in mitotic spindles, where it is difficult, if not impossible, to see individual MTs by fluorescence microscopy. By observing mitotic spindles that had been labeled with a low percentage of fluorescent tubulin, Waterman-Storer *et al.* (1998) were able to detect poleward speckle movement throughout the spindle. Although mitotic flux had previously been described using photomarking (Mitchison, 1989), FSM is much simpler and will most likely be instrumental in further studies aimed at understanding the mechanism of flux and its role in chromosome movement.

1.2.2 Quantitative FSM

Although many discoveries have already been made by FSM visualization of dynamic processes (cf. references in the next paragraph), the full potential of FSM will only be accessible through specialized computational tools for automatic extraction of all speckles and the statistical analysis of their translocations and intensity fluctuations. A typical speckle movie of, e.g. an actin meshwork at the protruding edge of a migrating cell, contains more than 500'000 speckles which move, appear and disappear. Furthermore, speckles are inherently stochastic image features with very low signal-to-noise ratio. To date, no commercial software is capable of tracking this vast number of speckles in time-lapse FSM series.

Thus far, hand tracking of only a few speckles has been employed, which is incredibly laborious, prone to error, and leaves the majority of information unexploited (Schafer *et al.*, 2002; Salmon *et al.*, 2002; Gupton *et al.*, 2002; Watanabe and Mitchison, 2002). Alternatively, kymographs provide rough estimates of speckle velocities (Waterman-Storer *et al.*, 1998, 1999, 2000; Salmon *et al.*, 2002; Gupton *et al.*, 2002; Kapoor and Mitchison, 2001; Brust-Mascher and Scholey, 2002). In kymographs of FSM image series, a three to seven pixel wide line whose axis is parallel to the direction of speckle movement is extracted from each image of the series and pasted side-by-side in a time-montage. As speckles move along the line they appear as oblique streaks on the kymograph, the slope of which corresponds to the velocity of speckle movement (Waterman-Storer, 2002). However, this analysis is limited to speckles moving along the same trajectory, it averages speed variations over time, and again delivers only sparse data.

1.3 Outline of the thesis

The main goal of this Ph. D. project consisted in the development of a fully automated, robust and possibly user-friendly software package for the extraction, tracking, and statistical processing of the huge numbers of speckles in FSM time-lapse series. This software should overcome the limitations of hand-tracking and kymograph analysis for the quantitative analysis of FSM data. We introduce the term *Computational Fluorescence Speckle Microscopy* (cFSM) to name this enhanced microscopy technique.

As a model system, the F-actin meshwork of newt lung epithelial cells was chosen, although other systems (like the mitotic spindle of *Xenopus* eggs) have been (partially) analyzed in the course of the project. The software in his first versions has been applied for

the quantitative mapping of the actin cytoskeleton turnover kinetics and kinematics with unprecedented spatial and temporal resolution in both contact-inhibited and motile cells.

After this introduction, the main section of the thesis is structured in four main chapters (chapters 2 through 5), presented in the format of scientific papers.

Chapter 2 presents the first version of our software for the fully automated analysis of FSM data sets. The cortical F-actin meshwork of contact-inhibited cells was analyzed and relative kinetic rates for the polymer turnover were obtained. This chapter has been published on the *Biophysical Journal* (see Ponti *et al.*, 2003 in the References).

Chapter 3 presents a particle tracker based on graph theory which proved to be exceptionally valid in the recovery of anti-parallel flow in extremely complex systems such as the mitotic spindle. This chapter has been published on the *Biophysical Journal* (see Vallotton *et al.*, 2003a in the References).

Chapter 4 introduces major enhancements to the algorithm. A new speckle extraction scheme and a hierarchical tracker allowed for the first time a full kinetic analysis to be performed on motile cells. This chapter has been submitted to the *Biophysical Journal*.

Chapter 5 analyzes in more detail the leading edge of motile cells and reveals that the lamellipodium and lamellum are kinetically and kinematically independent structures. This chapter will be completed and submitted to *Science*.

Finally, Chapter 6 summarizes the achievements and discusses some of the next steps which will be needed to further develop cFSM into *the tool* for quantitative cytoskeleton biology.

Remark for the reader: in this thesis the terms actin *meshworks* and actin *networks* have been used throughout the text. They should be considered absolutely equivalent.

2

Computational Analysis of F-Actin Turnover in Cortical Actin Meshworks Using Fluorescent Speckle Microscopy

2.1 Introduction

Fluorescent Speckle Microscopy (FSM) is a recently developed method to analyze the movement, assembly, and disassembly dynamics of macromolecular structures *in vivo* and *in vitro* (Waterman-Storer and Danuser 2002). Originally, it has been applied to the analysis of *in-vivo* microtubule movements in mitotic spindles and actin retrograde flow in migrating cells (Waterman-Storer *et al.*, 1998), and has now become the tool of choice for investigating many aspects of cytoskeleton dynamics. Speckled images of such polymer structures are obtained by micro-injecting low amounts of labeled monomers into cells. Random incorporation of few labeled and many endogenous unlabeled monomers into cellular structures yields a fluorophore distribution with high spatial density variation, which is, by light microscopic imaging, convolved with a diffraction-limited point spread function. We define a speckle as a peak in the image signal, significantly brighter than its surroundings. Most of the speckle data hitherto published refer to multi-fluorophore speckles formed by 3-7 fluorophores clustered within a diffraction-limited region, and only recently Watanabe and Mitchison (2002) were able to acquire single-fluorophore speckles in actin structures in fibroblasts.

Speckles act as local reporters throughout the polymer lattice. In time-lapse FSM, speckle appearance and disappearance are linked to polymerization and depolymerization whereas speckle movement is associated with polymer translocations. Therefore, FSM allows simultaneous and local measurements of polymer turnover and movement in large areas of the cell, with a time-resolution equal to the frame rate of the movie. This offers a novel tool for studying non-steady state molecular processes in live cells.

In this paper we apply FSM to the study of cortical F-actin meshwork dynamics in contact-inhibited newt lung epithelial cells. Contact-inhibited cells form tight adherens junctions with neighboring cells (Harris, 1999). In contrast to migrating cells, where F-actin meshworks, and thus actin fluorescent speckles, undergo a coordinated motion known as “retrograde flow” (Abercrombie *et al.*, 1972; Small, 1981; Wang, 1985; Forscher and Smith, 1988; Danuser and Oldenbourg 2000, Waterman-Storer *et al.*, 2002), in contacted cells cortical F-actin meshworks remains spatially stationary. However, FSM movies still show a strong photometric activity, indicating that F-actin is undergoing steady turnover (Waterman-Storer *et al.*, 2000a). We investigated how to extract quantitative information of this turnover in order to shed new light on the mechanisms of actin dynamics. Our long-term goal is to

develop a quantitative live-cell assay to study the effect of biochemical reagents, molecular and genetic factors involved in the regulation of actin dynamic processes.

Speckles are a weak and inherently stochastic image feature with a low signal-to-noise ratio (SNR). For this reason, any measurement derived from FSM data must rely on a statistical processing of large numbers of speckles. Typically, FSM movies contain >500,000 speckles which fluctuate in intensity, move and disappear, while new speckles appear. Speckle fluctuations are induced by stochastic molecular processes and their interpretation requires mathematical models of the relation between changes in speckle signal and the alteration of the polymer. Hence the demand for computational tools, where each speckle is automatically tracked in position and intensity and statistically processed according to the models.

In the core of this paper we propose a first version of an algorithm working along these lines and we demonstrate its performance on synthetic and experimental data. The Materials & Methods introduce the experimental protocols and a simulation package that enabled us to establish a forward model of speckle formation dependent on several biochemical and imaging parameters. Artifacts in the imaging and analysis steps are discussed in the concluding section along with a summary of the key features of our computational model.

2.2 Materials and methods

2.2.1 Software development

All programs for speckle analysis and graphical representation have been written in house using MATLAB version 6.0 (Mathworks, Inc. Nattick, MA). The computation is performed on high-end PCs running either Windows or Linux operating systems.

2.2.2 Synthesis of FSM movies using Monte Carlo simulations of dynamic F-actin meshworks

For code debugging and to investigate the relationship between speckle lifetime and polymer turnover in a complex macro-molecular structure we implemented a Monte Carlo simulation of how fluorescently labeled and unlabeled monomers dynamically associate and dissociate from an F-actin meshwork. The physical model is depicted in Fig. 2-1 (a). In such a meshwork, the 3D distribution of fluorophore is determined by a contribution of three random

processes: i) distribution of free barbed and pointed ends of actin filaments; ii) rates of association and dissociation of actin monomer at the two filament ends (Pollard, 1986); iii) binomial sequence of labeled and unlabeled monomers turned over at all free ends. Image data was synthesized by convolution of the simulated fluorophore distribution with a 3D model point spread function of the microscope plus by random addition of Poisson-distributed shot noise, and normal distributed camera dark and readout noise. The program simulates the distribution of barbed and pointed ends based on a user-specified function defining the spatial variation in area concentrations of the two kinds of ends. This allowed us to simulate F-actin meshworks with spatially modulated probabilities of assembly and disassembly. Once the barbed and pointed end distributions and the concentration of monomer are set, the meshwork locally assembles and disassembles. If necessary, a steady state, i.e. monomers associate to and dissociate from the meshwork at on average equal rates, can be simulated by periodic redistribution of the free ends. In this implementation, the model was useful to validate our software for kinetic analysis (see Results) but it cannot reveal any relationship between the observable speckle intensity fluctuations and regulatory factors of F-actin turnover.

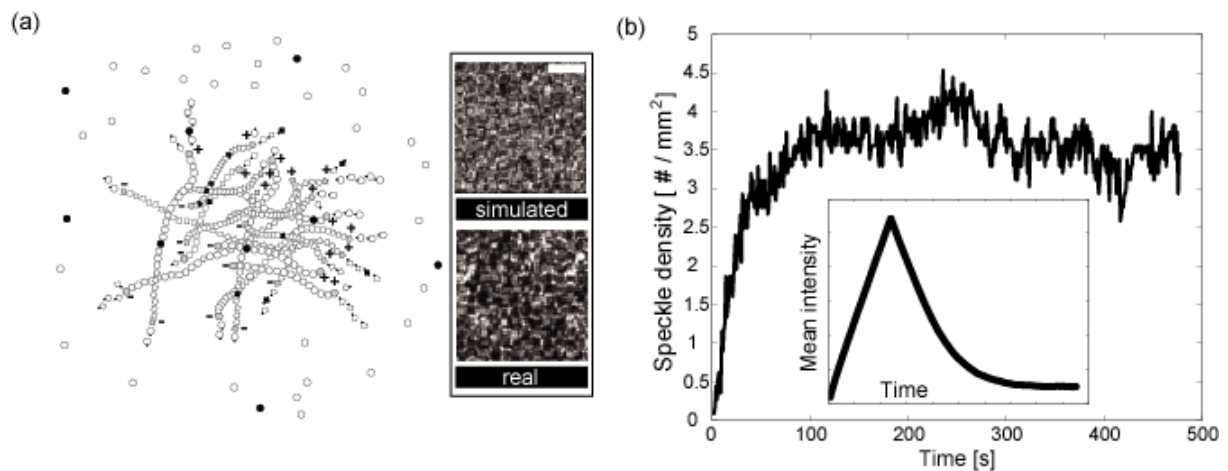


Figure 2-1

Dynamic simulations of a polymerizing and depolymerizing F-actin meshwork. (a) Physical model for the generation of an actin meshwork. The inset shows a comparison between simulated and real FSM image data. Scale bar, 1 μm . (b) Mean speckle number density from five simulations of a meshwork that assembles for 120 s and disassembles for 360 s at equal rates (inset, mean fluorescence intensity development). Meshwork disassembly is associated with a decrease in the mean intensity. Once the steady-state speckle number density is reached (after 100 s), the mean speckle density is independent of whether the meshwork is polymerizing or depolymerizing, but only dependent on the PSF volume. With $NA=1.4$ optics, the number density is 3.5–4 speckles per μm^2 .

In particular, the simulation does not include chemical reaction equations other than the stochastic rate equations of monomer association and dissociation. A more complex modeling of these rates as functions of a network of interdependent chemical equilibriums affected by numerous effectors upstream of F-actin turnover is a challenging future task. It is now addressable in combination with our new quantitative FSM experiments which can test the roles of specific effectors under drug perturbation.

Despite the many oversimplifications, the model was sufficiently accurate to produce speckled images (Fig. 2-1 (a)) and to teach us a critical lesson about FSM of a polymeric meshwork: the speckle number density is almost independent of whether the meshwork assembles or disassembles; but depends only on the PSF volume. With $NA=1.4$ optics, the number density is 3.5 – 4 speckles per μm^2 (Fig. 2-1 (b)). The graph in Fig. 2-1 (b) displays the mean speckle number density from five simulations of a meshwork that assembles for 120s and disassembles for 360s at equal rates (inset: mean fluorescence intensity development). The steady-state speckle number density is reached after 100s. The fact that the speckle density remains constant despite further addition of labeled monomer suggests that monomer association can cause an equal number of speckle appearances (births) as disappearances (deaths). The same holds for dissociation. This finding caused us to develop the classification scheme of speckle birth and death which is now the core of the algorithm for kinetic analysis (see Algorithm). Data such as presented in Fig. 2-1 was used to prove the concepts of the algorithm and to verify their performance (see Results).

2.2.3 Cell Manipulations

Primary cultures of newt lung epithelial cells were established on 22x22 mm #1.5 coverslips from *Taricha granulosa* lung tissue and maintained in Rose Chambers at $\sim 20^\circ\text{C}$ in $\frac{1}{2}$ strength L-15 media containing 5% FBS, antibiotics and antimycotics as previously described (Waterman-Storer and Salmon, 1997; Reider and Hard, 1990). We microinjected 0.5 mg/ml X-rhodamine labeled actin (prepared as described in Waterman-Storer, 2002) into newt lung epithelial cells that were contacted on all sides by neighboring cells and situated in the center of the epithelial sheet that extends from the explant of lung tissue during the wound healing response in culture. For FSM imaging, coverslips of injected cells were mounted on slides on two strips of double-stick tape in culture media containing 30 U/ml of Oxyrase (to inhibit photobleaching, Oxyrase, Inc., Mansfield, OH) and sealed with valap (1:1:1 mixture of Vaseline, lanolin, and paraffin). For some experiments, injected cells were fixed in 4% paraformaldehyde in PBS (140 mM NaCl, 15 mM Na-phosphate, 2.5 mM KCl, 1.6 mM K-

phosphate, pH 7.2) for 5 minutes, rinsed in PBS, and mounted on slide/tape chambers in cell culture media with or without Oxyrase. For latrunculin-A perfusion experiments, coverslips of cells were mounted in a custom-built perfusion chamber that was sealed to ambient air in media containing Oxyrase, and gravity-perfused with media containing 750 nM latrunculin A and Oxyrase.

2.2.4 Time-lapse Spinning Disk Confocal FSM

Time-lapse FSM was performed using a spinning disk confocal microscope system on an inverted microscope (TE300 Quantum, Nikon, Melville, NY) using a 100x 1.4NA Plan-Apochromatic DIC objective lens. Light from a 50 mW Krypton-Argon ion laser (OmniChrome/Melles Griot, Irvine, California) was delivered by a single-mode fiber optic (Point Source) to the UltraView spinning disk confocal scan-head (PerkinElmer, Inc., Wellesley, MA). Excitation wavelength was selected by a filterwheel apparatus (Lamda10-2 Sutter Instruments, Novato, CA) containing excitation filter for 568 nm (Chroma, Brattleboro, VT) and an opaque disk for use as an excitation shutter. Images with an average exposure time of 1.5-2 seconds were collected at 5 sec intervals on an Orca 2 camera (Hamamatsu, Inc., Bridgewater, NJ) containing a 1280 x 1024 array of 6.7 x 6.7 μm pixels in progressive scan interline transfer configuration operated in the slow-scan (1.25 mHz) 14 bit-depth mode, where the noise is typically 3-5 electrons rms. Focus was controlled by a stepper motor (Ludl Electronic Products Ltd., Hawthorne, NY). Microscope functions were controlled by MetaMorph (Downingtown, PA) software on a PC computer.

2.2.5 Characterization of image noise

2.2.5.1 Titration experiments

Solutions of varying concentrations of x-rhodamine labeled actin (0, 8, 15 and 22 μM) were prepared in G-buffer (2 mM Tris, 0.2 mM CaCl_2 , 0.2 mM Mg ATP, 0.5 mM β -mercaptoethanol, pH 7.0). 0.8 μl of solution was squashed between a slide and a 22 x 22 mm coverslip, and the coverslip sealed to the slide with valap. This reproducibly gives a layer of solution that is $\sim 4 \mu\text{m}$ thick. Images of the solution just adjacent to the coverslip surface were then acquired with the spinning disk confocal system for each concentration with exposure times in an interval ranging from 500 ms to 3000 ms in 100 ms steps.

2.2.5.2 Calibration of a noise model

For the estimation of noise parameters at different exposure times, a calibration of the camera was performed. For four concentrations of X-rhodamine-actin solutions (0 μM defining the dark field, 8, 15 and 22 μM) 11 images were acquired per exposure time setting (see Titration experiments). From the dark field image series, the parameters I_0 and α_{DN} in Eq. (2.2) (see Algorithm – Statistical selection of speckles) were estimated. The mean of all pixel intensities over 11 images defined the value for I_0 . To estimate α_{DN} , the intensities $I(x,y)$ of the 11 dark field images were first analyzed in a position-dependent fashion, providing variances $\sigma_{DN}^2(x,y)$. The average of this variance field provided a measure for the dark and readout noise α_{DN} .

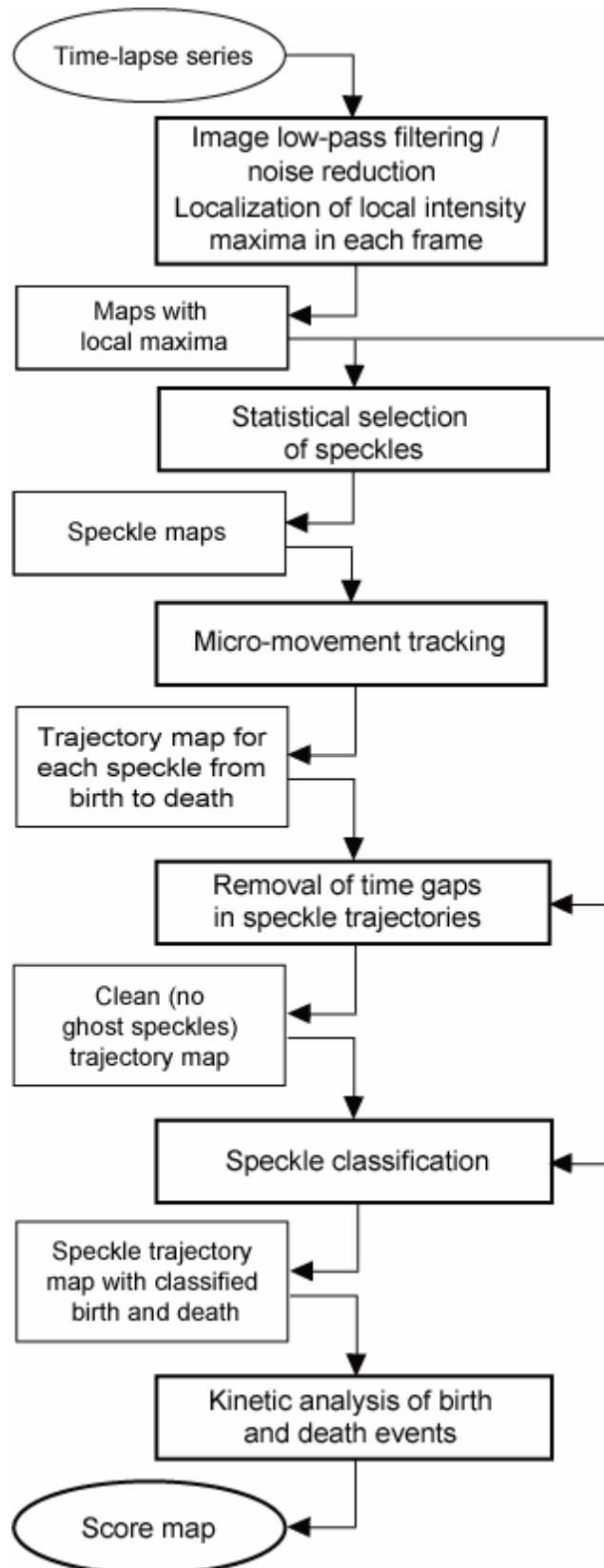
Variances σ_i^2 were calculated for all other concentrations $i = 8, 15, 22 \mu\text{M}$ in the same way and the mean intensity I_i was used to define the intensity dependence of noise according to $\sigma_i^2 - \alpha_{DN} = \beta(I_i - I_0)$ (see Eq. (2.2)). The parameter β was estimated by linear regression of the data pairs (σ_i^2, I_i) .

2.3 Algorithm

We describe an algorithm for the extraction of kinetic parameters of F-actin turnover from time-lapse FSM in otherwise stationary meshworks, as they occur in contact-inhibited cells. A typical FSM movie consists of 100-200 frames at sampling rates between 1 and 5 seconds per frame. A graphical outline of the algorithm is given in Fig. 2-2.

2.3.1 Noise reduction and local maximum selection

The F-actin cytoskeleton acquires its speckle pattern due to random incorporation of actin monomers into actin filaments at a very low labeling ratio ($< 0.5\%$). The labeling ratio f is defined as the fraction of labeled monomers in the entire cytoplasmic monomer pool. This results in a high spatial variation of the fluorophore density, which, after imaging with high magnification diffraction limited optics, appears as a band-limited signal with a random texture of intensity maxima and minima. We define a speckle as a local intensity maximum in the fluorescence signal, associated with a locally high density of fluorophores.

**Figure 2-2**

A computational scheme for kinetic analysis of FSM data (see text for details).

In multi-fluorophore FSM a speckle corresponds to a clustering of 3 to 7 fluorophores in an area defined by the lateral extension of the microscope point spread function (PSF) (Waterman-Storer and Salmon, 1999). A speckle can thus be regarded as a local probe in the actin meshwork, in which fluctuations in the signal intensity indicates polymer turnover with high temporal and spatial localization. The maximal spatial resolution achievable is defined by the mean distance between two distinguishable speckles; the temporal resolution is defined by the frame rate of the movie.

In the raw FSM image data, many of the observed local maxima are, however, not due to locally clustered fluorophores, but due to noise. To separate noise from speckles, we rely on the fact that pixel intensities belonging to one speckle are spatially correlated over the radius of the PSF, while intensity variations due to noise are independent between pixels. Convolution of the signal with a low pass filter with a frequency cutoff ν_c equal to the bandpass of the optical transfer function (OTF) will guarantee preservation of the speckle signal while suppressing noise at spatial frequencies higher than ν_c . For numeric stability we apply a Gaussian kernel for low pass filtering

$$G(r, s) = \frac{1}{\sqrt{2\pi s^2}} \cdot e^{-\frac{1}{2} \frac{r^2}{s^2}}, \quad (2.1)$$

instead of a kernel with a sharp cutoff ν_c . The parameter $r^2 = x^2 + y^2$ in Eq. (2.1) denotes the distance of a pixel contributing to the convolution from the center of the Gaussian kernel, and the parameter s defines the filter drop off. We determined the latter in agreement with the PSF of our spinning disk confocal microscope. Under conditions identical to our FSM experiments, Maddox *et al.* (2003) measured a PSF full width at half maximum (FWHM) of 260 nm using sub-resolution fluorescent beads. Expressed in the image domain, this results in

a FWHM of 3.9 pixels. Therefore, we set the parameter s of the Gaussian kernel to 1.25 pixels to match the experimental FWHM and the FWHM of our noise filter.

After low-pass filtering we apply a local maximum detection in a 5x5 pixel mask:

$$L = \{L_i\}, \forall i \{I(\mathbf{x}_i) > I(\mathbf{x}_i + \mathbf{t}) \text{ with } \mathbf{t} = [t_1, t_2]; t_1, t_2 = -2 \dots 2\}.$$

The size of the mask is again motivated by the diameter of the PSF. Each local maximum is a speckle candidate. Typically, several thousands of them are extracted by this first algorithmic step.

2.3.2 Statistical selection of speckles

With the choice of a noise filter with the same FWHM as the PSF and thus an almost identical frequency cut-off as the OTF, noise components corresponding to spatial frequencies below the optical cut-off are still present and interfere with the proper speckle signal. Therefore, many of the local maxima are still due to noise and are not associated with an actual speckle. The set L has to be divided into two subsets $L = S \cup L_N$, where the set S contains local maxima representing speckles and L_N contains *weak local maxima* due to noise.

The set partitioning relies on a noise model permitting a test of each local maximum for its statistical significance. We assume that the image noise is a superposition of two independent components, dark noise and shot noise (Oshiro, 1998). The dark noise component can be modeled as an additive and normal distributed random variable with a variance σ_{DN}^2 . Shot noise is proportional to the signal intensity and needs to be calibrated once for every experimentally applied exposure time. It is Poisson distributed with the mean number of photons representing the mode of the distribution and a variance σ_{SN}^2 proportional to the number of photons (Papoulis, 1991). In total, we describe noise as the variance of the intensity I

$$\sigma^2 = \sigma_{DN}^2 + \sigma_{SN}^2,$$

with

$$\sigma_{SN} = \gamma(I - I_0)^{\frac{1}{2}}.$$

The parameter I_0 is the camera offset expressed in gray levels. The coefficient γ defines the proportionality factor between the square root of the offset-corrected image intensity and the variance of the image signal induced by shot noise. Consequently, the total variance can be written as a linear function of intensity:

$$\sigma^2(I) = \alpha_{DN} + \beta(I - I_0), \quad (2.2)$$

with $\alpha_{DN} = \sigma_{DN}^2$, and $\beta = \gamma^2$. The parameter β has been calibrated once for our imaging system (see Materials and Methods). It remains constant between experiments, unless there is a change in the applied camera gain or exposure time. In contrast, the camera offset and dark noise slightly vary between image stacks. Therefore, the values for α_{DN} and I_0 are recalculated for every time-lapse series by analyzing background regions without fluorescent signal. Expressed in the normalized intensity range $[0, 1]$ used for all image data processing, the value for β determined amounted to 2.00×10^{-4} , and the value for the dark noise σ_{DN} averaged over several movies was 2.73×10^{-4} with $\bar{I}_0 = 2.84 \times 10^{-2}$. Converted into the intensity range of our 14-bit CCD camera this corresponds to a camera offset of 472 gray levels with a dark noise of 5 gray levels. Speckle peak intensities reached 630 gray levels at maximum. Applying Eq. (2.2) to this signal yields a combined dark and intensity-dependent noise of 18 gray levels. This example also illustrates the maximum SNR found in our FSM data. Defining the SNR of a speckle as the ratio between peak intensity above background and the noise level propagated for this intensity difference, we obtained signals with $\text{SNR}_{\max} = 8.5$ at best.

Using the noise model, an intensity dependent confidence interval ΔI_C can be calculated for each local maximum in L . Maxima with a peak intensity (I_L) that is in a statistical sense more than ΔI_C above the adjacent background (I_{BG}) are accepted as speckles and thus added to the set S . Maxima not satisfying this criterion are assigned to the set L_N . Fig. 2-3 illustrates this notion of a speckle as a statistically significant image feature. Fig. 2-3 (a) displays the speckled fluorescence intensity image of F-actin in a living cell, of which Inset a1 shows a zoom-up window represented in a2 as a continuous function in \mathbb{R}^2 . Fig. 2-3 (b) shows an isolated speckle with peak intensity I_L above a relatively homogeneous background intensity I_{BG} .

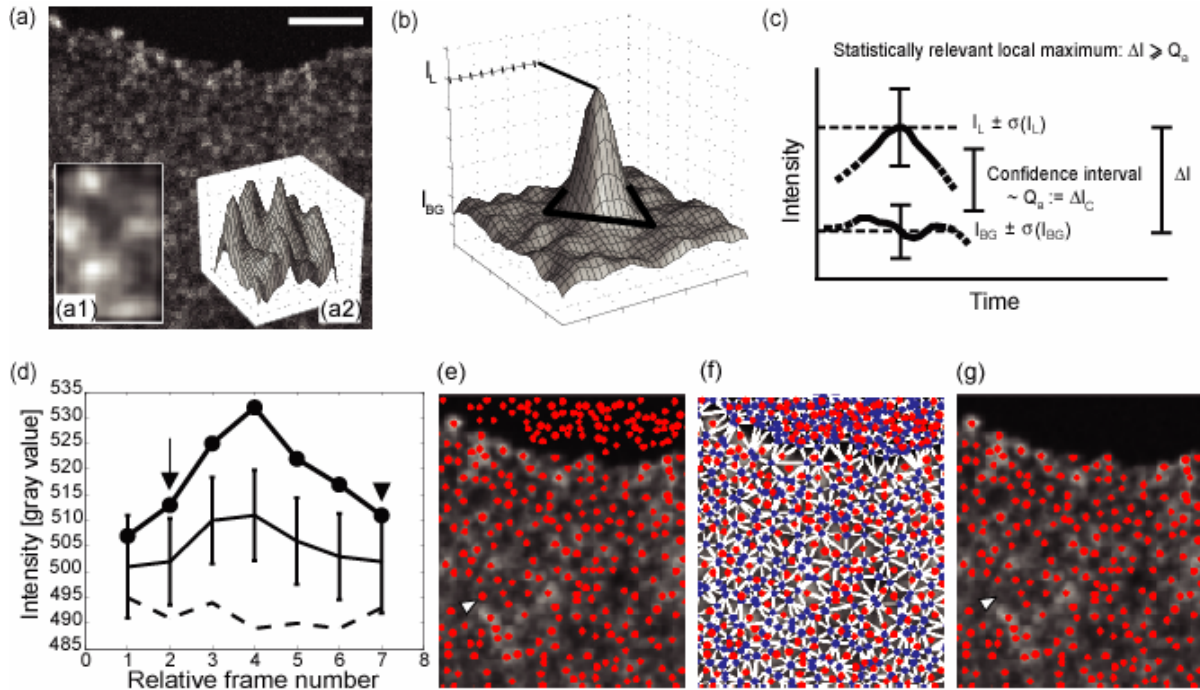


Figure 2-3

Separation of speckles, i.e., significant local maxima in the image from noise-related weak local maxima. (a) Images are low-pass filtered to remove high-frequency noise. Scale bar, $2.5 \mu\text{m}$. (Inset a1) Zoom-up of a sub-region after filtering; (Inset a2) The same sub-region displayed as an intensity function in \mathbb{R}^2 . (b) Definition of a speckle as an intensity peak above background. (c) Principles of statistical speckle selection (see text for additional explanations). (d) Example of a speckle lifetime history; time point of speckle birth (arrow) and time-point after speckle death (arrowhead). (e) – (g) Statistical selection of speckles illustrated on an image. (e) Result of local maximum (red dots) extraction. (f) Local minima (blue dots) extraction and assignment of background intensities to local maxima by Delaunay triangulation of local minima (see text). (g) Local maxima failing the Student's t test are not counted as speckles. The arrowheads in (e) and (g) indicate the position of one weak local maximum falling through the statistical selection.

Notice that the background intensity is not always as clearly defined as in this case but that generally it has to be extracted from intensity distributions with rather complicated topographies (see a2). A procedure for the calculation of the background is discussed later in this section. Given the peak and background intensities, the difference ΔI between the two has to exceed the critical interval ΔI_C to render a local maximum a speckle. This is depicted by Fig. 2-3 (c), where the two levels differ more than the required confidence interval. As it will be introduced in Eq. (2.4), the size of the interval is a function of the estimated noise in the two intensity values. Fig. 2-3 (d) already suggests a possible development of a speckle throughout its lifetime of, in this case, 5 frames. It starts out as a non-significant local maximum (frame 1) before it turns into a speckle (the arrow in frame 2 indicates the *speckle*

birth). To illustrate the statistical conditions, the critical interval ΔI_C is plotted at the midpoint between the peak and background intensities. As long as the speckle is alive (frames 2-6), the peak-to-background intensity difference is greater than the critical interval, whereas the speckle turns again into an insignificant local maximum at frame 7 (arrowhead). *Speckle death* occurs at the last time point where the peak intensity I_L is significantly higher than the background intensity I_{BG} (frame 6).

Obviously, the entire selection procedure depicted by Fig. 2-3 (a)-(d) relies on an estimate of the local background for each element in L . In analogy to the procedure for local maximum detection, local minima are sought in every image. Fig. 2-3 (e)-(g) displays the different steps of speckle selection. Panel 2-3 (e) shows a portion of the low-pass filtered image of speckled actin in a living cell overlaid with local maxima (red dots). In panel 2-3 (f) the local minima (blue dots) are displayed. Using Delaunay triangulation these points are connected to form a meshwork (white solid lines). By definition, Delaunay triangles have the property that the circumscribing circle of each triangle does not contain vertices from any other triangle in the meshwork. Therefore, every local maximum can be unambiguously assigned to a triangle of three local minima (Fig. 2-3 (f)), of which the mean intensity \bar{I} provides a measure I_{BG} for the background intensity. Using Eq. (2.2), uncertainties for both the local maximum intensity $\sigma(I_{LM})$, and the background intensity $\sigma(I_{BG})$ can be derived (cf. Fig. 2-3 (c)). In mathematical terms, the statistical test for speckle selection then amounts to performing a Student's t test with a user-defined confidence probability α :

$$\begin{aligned} H_0 &: |\Delta I| = 0; \text{ with } \Delta I = I_L - I_{BG}; \\ H_A &: |\Delta I| > 0; \\ T &= \frac{|\Delta I|}{\sigma_{\Delta I}} \propto t_{\infty}(0,1); \end{aligned} \quad (2.3)$$

with

$$\sigma_{\Delta I}^2 = \sigma^2(I_L) + \frac{1}{3}\sigma^2(I_{BG}) \quad (2.4)$$

H_0 is rejected if $T \geq Q_{\alpha}$ where Q_{α} is the Student's t quantile. Notice in Eq. (2.4) that the contribution of the background to the variance of the intensity difference is three-times smaller than the one of the local maximum. This is because the background value is an estimate based on three intensity values.

The result of the statistical test is displayed in Fig. 2-3 (g). The selection step removes a few weak local maxima from the background, although in the example shown most of the local maxima are retained as significant. This suggests that many noise-induced image features are already removed in the initial low-pass filtering. The arrowheads in Fig. 2-3 (e) and 2-3 (g) indicate the position of one weak local maximum not suppressed by low-pass filtering and failing to pass the statistical test. This almost ideal scenario, however, deteriorates with image artifacts that cause sudden fluctuations and fading of the speckle contrast associated, for example, with in- and out-of-focus movement of the sample. In such situations substantially more weak local maxima are eliminated.

2.3.3 Micro-movement tracking

After selection of speckles, their microscopic movements are tracked over time. A speckle at time point t is linked to a speckle at time point $t+1$, if the distance between the two positions is less than or equal to half the diameter of the Airy disk. This is motivated by the fact that the mean distance between two speckles in the same frame is generally higher. Exceptions to this rule occur with overlapping speckles, although most of these overlaps are eliminated by the low-pass filtering. The few remaining cases are currently neglected by our software. The position of each speckle varies over time even in spatially stationary actin meshworks as studied in this work. This is due to physical effects, such as Brownian motion and motor protein-induced meshwork contractions, as well as signal effects caused by the addition or removal of fluorescent label near an existing speckle. Also the presence of a noise-induced local maximum nearby a speckle will significantly shift the speckle position during low-pass filtering. In this context, it must be noticed that the signal contribution due to free actin monomers diffusing through the cytosol does not affect either the position or the intensity of a speckle. Given a diffusion rate of 47 pixels / s in our imaging system (Abraham *et al.*, 1999) the signal generated by a labeled but unbound monomer in one pixel is, over the exposure time of 0.5 to 3 s used in FSM, one to two orders of magnitude smaller than the one of a bound monomer. This was recently demonstrated by Watanabe and Mitchison (2002), where even the more critical case of single fluorophore speckles was examined.

If a speckle at time t cannot be linked to a speckle at time $t+1$ according to the above criterion, it is classified as a dying speckle. On the contrary, speckles in $t+1$ that are not linked to speckles in t are classified as new speckles. As a result, the micro-movement tracker provides speckle trajectories existing between frames t_b (time of birth) and t_d (time of death). Sometimes, newly born speckles cannot be linked to any other speckle in the following frame.

In this case, t_b equals t_d . They are referred to as *ghost speckles*. The existence of ghost speckles is expected from a statistical point of view, because speckles are indeed weak features with a low signal-to-noise ratio. However, they also occur with failures in the tracking or with the fusion and dissolution of multiple speckles. Both situations are not yet optimally addressed by our software and we suppose that a certain percentage of ghost speckles are not associated with short-living features but with sub-optimal analysis (see also Discussion).

After the identification of trajectories, the software stores for each speckle peak and background intensities, speckle position and the positions of the three local minima at every time point t ($t_b \leq t \leq t_d$). Furthermore, the same information is stored for the last time point t_b-1 before birth and for the first time point t_d+1 after death. The importance of this additional information will be discussed below.

The speckle trajectories may be interrupted sometimes because of peak and background intensity fluctuations that yield failures of the test in Eq. (2.3). Consequently, speckle lifetimes are underestimated and many artifactual birth and death events will be accumulated. This problem must be addressed before kinetic analysis of birth and death events.

2.3.4 Removal of time gaps in speckle trajectories

To circumvent the problem of false speckle birth and death detection, all birth and death events are analyzed individually. If a speckle that disappears at time $t-1$ is spatially close (not farther than the Airy disk radius) to a speckle that appears at time $t+1$, meaning that at time t there is no significant local maximum that links the two fragments, the gap in t can be closed if and only if there exists a weak local maximum in $L_N(t)$ with a position in the same neighborhood. If this is the case, the maximum in $L_N(t)$ is moved to the set $S(t)$. The gap is closed, and two apparent events (one death and one birth) are removed from the event list. Fig. 2-4 illustrates the intensity development of a speckle with five closed gaps (arrows). The dashed line indicates the critical intensity difference. Small fluctuations in the peak and background intensities cause an initial fragmentation of one speckle into several sub-speckles, which are fused by the gap closer.

The importance of suppressing false birth and death events will become evident as we describe the algorithm further. For the remainder of the article, we will refer to the complete

speckle trajectory, including the development of peak and background intensities, simply as a speckle.

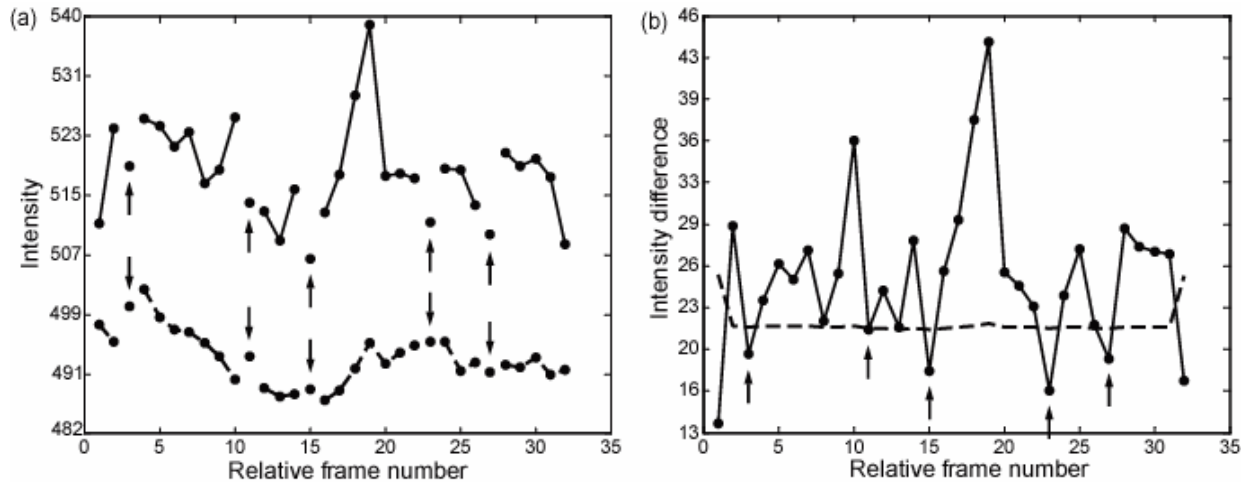


Figure 2-4

Gap closer. (a) The linking of six short-living speckles (full lines) separated in time by one frame and in space by less than the Airy disk diameter removes false birth and death events and reconstructs one long-living speckle (b). The linking of two speckles is only allowed if the gap frame contains a weak local maximum within distance of the Airy disk radius to both the false death position of the first speckle and the false birth position of the second speckle (arrows in panel a). Further details on the linking conditions are given in the text. Panel b displays the intensity differences $\Delta I = I_L - I_{BG}$ between peak and background, superimposed by the critical intensity difference ΔI_C calculated with the noise model (dashed line).

2.3.5 Classification of birth and death events

Waterman and Salmon (1998) demonstrated that for single microtubules, speckle appearance and disappearance indicate assembly and disassembly of the polymer. Using our framework for FSM simulations (see Materials and Methods) we learned that this is not true for actin meshworks, where fluorophores forming one speckle can belong to several criss-crossed filaments. A new speckle appears wherever the fluorophore distribution increases in number relative to the immediately adjacent surroundings. This can occur in two ways (Fig. 2-5): 1) new fluorophores are incorporated into the meshwork, resulting in a locally higher fluorophore density and giving rise to a new speckle; 2) in an area with a low variation in fluorophore density and therefore no discernible speckles, the dissociation of fluorophores can result in a change of distribution such that the concentration of fluorophores becomes higher

in one place compared to its surroundings. This may give rise to a new speckle as well. In the same manner speckles can disappear: either by dissociation of fluorophores at the site of the speckle, or by association of fluorophores in the neighborhood, resulting in a homogenization of the fluorophore distribution. Therefore, the algorithm has to distinguish between four situations (Fig. 2-5): (a) speckle birth due to polymerization; (b) speckle birth due to depolymerization; (c) speckle death due to depolymerization; (d) speckle death due to polymerization. The graphs display the speckle and background intensity development from one time point before appearance until one time point after disappearance. The relevant event (birth or death) is marked with an arrow. As in Fig. 2-3 (e), the confidence intervals for ΔI are plotted in the midpoints between the peak and background intensities.

Whether birth or death are associated with local assembly or disassembly of the actin meshwork can be decided based on the speckle intensity change in small time windows around the events. For all speckles with a lifetime of at least two time points, we consider the last time point (t_{b-1}) before speckle appearance, the time point of appearance (t_b) and one time point after appearance (t_{b+1}) (Fig. 2-5 (a) and (b)). Speckle and background intensities for the time point before appearance are extracted from the corresponding set of weak local maxima $L_N(t_b - 1)$. If an element of $L_N(t_b - 1)$ exists in the immediate spatial neighborhood of a speckle appearing at time t_b , then its intensity as well as the intensity of its background are added to the speckle history as the pre-birth event. If no such local maximum is found, the coordinates of the speckle and of the three local minima in t_b are used to obtain an estimate of the same values in t_{b-1} . In the same way we consider the time point before (t_{d-1}), at (t_d), and after speckle disappearance (t_{d+1}) to classify the speckle deaths (Fig. 2-5 (c) and (d)). Fig. 2-5 (d) refers to a case of speckle death due to polymerization. The intensity development of this speckle demonstrates at the same time a pathological situation, sometimes occurring with the above explained extrapolation of intensities of pre-birth and post-death events. The birth of this speckle is characterized by a pre-birth difference between peak and background intensity larger than the confidence interval ΔI_c (arrowheads). Such a situation can only occur when no weak local maximum is available for extrapolation of the intensities in t_{b-1} . The values for peak and background intensities are therefore extracted from the image using the coordinates of the speckle in t_b as explained before. In some cases, the intensity development between two consecutive time points can change abruptly, so that local intensity values get decorrelated over time. Any kinetic analysis in this time-point is meaningless.

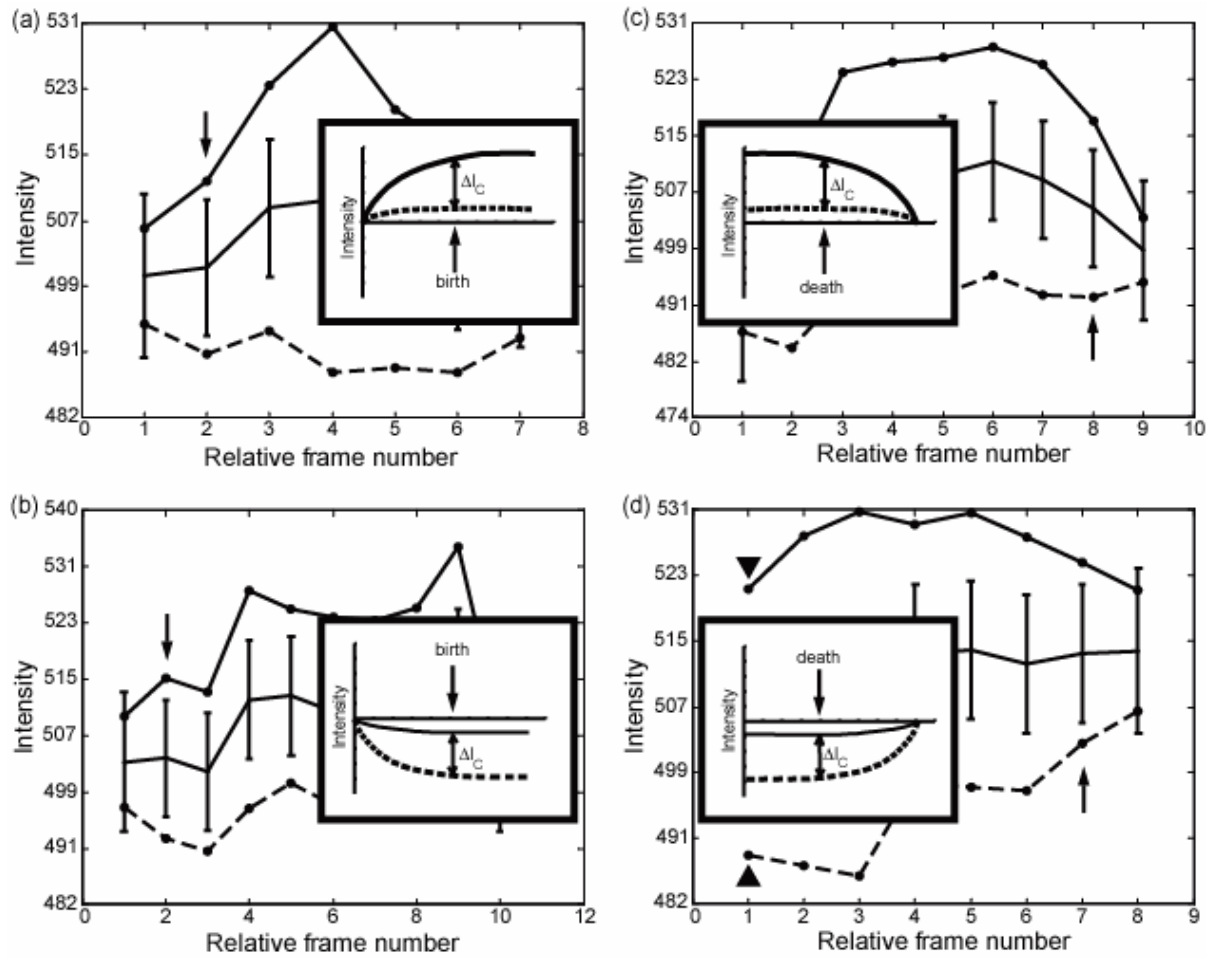


Figure 2-5

Classification of births due to polymerization (a) and births due to depolymerization (b), respectively; deaths due to depolymerization (c); and deaths due to polymerization (d). See text for further explanation of the scheme.

For the classification of a birth or death event, the speckle intensities as well as the background intensities at the time points around the actual event are fitted with linear regression. This yields an estimate of the rate of intensity change, represented by the slopes $a_{speckle}$ and $a_{background}$. We also calculate the standard deviation of the slopes using error propagation of the residuals of the intensity values to the regression line. Noisy data, poorly represented by the linear model, will therefore generate large values for σ_a ; intensity values in perfect match with the linear trend will result in small values for σ_a . We test the ratio $\frac{|a|}{\sigma_a}$ in a Student's t test and exclude statistically insignificant slope measurements if $\frac{|a|}{\sigma_a} < Q_\alpha$.

Then, we compare the ratios between speckle slope and background slope. Table 2-1

summarizes the conditions for each of the four event classes. The events which do not satisfy the criteria in Table 2-1 are excluded from the analysis.

It should be noticed that the strategy of analyzing only short intervals renders the algorithm relatively robust against the longer term effects of bleaching and intensity changes associated with focus drift or sample movement in axial direction.

2.3.6 Kinetic analysis of birth and death events and accumulation of actin turnover maps

Using the classification of speckle birth and death events the final step of the algorithm is to extract a measure for the polymer kinetics reported by the speckle activity. This analysis is motivated by the fact that the changes in fluorescence intensity, which either lead to the formation or dissolution of a speckle, reflect, on average, the rate difference between local monomer association and dissociation. Nominally, the conversion factor between the rate difference and the observable intensity fluctuation is governed by the labeling ratio f . Of course, the same argument holds for any image point and not only for speckles. However, the appearance or disappearance of a speckle marks spots of particularly high kinetic action, which can be quantified significantly above noise, while the continuous analysis of a more homogeneous fluorescence signal over time is prevented by imaging artifacts such as noise and bleaching (see Discussion).

During classification, each significant event is assigned with the intensity slope $|a|$ resulting in the highest ratio $\frac{|a|}{\sigma_a}$. We refer to this slope as the *score* s of the event. Scores are counted positive for polymerization events and negative for depolymerization events (see last column of Table 2-1). Notice that the score values are highly stochastic: given a rate difference r , i.e. the net number of monomers added or removed in the diffraction-limited area of a speckle, the variation of the score is proportional to $\sigma_s^2 \propto r \cdot f(1-f)$. In addition, the score measures are perturbed by noise according to Eq. (2.2). However, given a space-time window in which the rate difference r remains constant, statistical elimination of the score variation and noise perturbation is achievable by averaging the scores of several events. In this case, the expectation value is $\mu = r \cdot f$ for which the mean value of the scores \bar{s} represents an unbiased estimator. In practice, these assumptions will not be completely satisfied: 1) the scores are susceptible to in- and out-of-focus movements of the entire sample, as well as of individual speckles; and 2) they are susceptible to bleaching. Artifacts due to

single speckle axial motion are also largely eliminated by averaging (see Discussion for a more detailed analysis of artifacts).

In summary, the kinetic analysis has to make a trade-off between robustness of the estimate and reduction in temporal and spatial resolution. The larger the space-time window, the less is the influence of the various perturbation factors, at the cost of lower density information. The second point to notice is that the scores can currently not deliver absolute rate values, but only relative values. To achieve absolute values one needs: 1) to have experimental control over the fraction f ; 2) to calibrate the conversion factor between fluorophore density and image signal intensity. Both requirements are practically difficult to fulfill with sufficient accuracy. Therefore, we confined the algorithm to kinetic mapping on a *relative* scale.

In the following we explain the method for space-time averaging and simultaneous interpolation of the scores. Given the sets of events $E(t) = \{e_1^t, \dots, e_{n_t}^t\}$, $E(t-1) = \{e_1^{t-1}, \dots, e_{n_{t-1}}^{t-1}\}$, $E(t+1) = \{e_1^{t+1}, \dots, e_{n_{t+1}}^{t+1}\}$ at the time points t , $t-1$ and $t+1$, with the associated sets of event positions $P(t) = \{\mathbf{p}_1^t, \dots, \mathbf{p}_{n_t}^t\}$, $P(t-1) = \{\mathbf{p}_1^{t-1}, \dots, \mathbf{p}_{n_{t-1}}^{t-1}\}$, $P(t+1) = \{\mathbf{p}_1^{t+1}, \dots, \mathbf{p}_{n_{t+1}}^{t+1}\}$ and scores $S(t) = \{s_1^t, \dots, s_{n_t}^t\}$, $S(t-1) = \{s_1^{t-1}, \dots, s_{n_{t-1}}^{t-1}\}$, $S(t+1) = \{s_1^{t+1}, \dots, s_{n_{t+1}}^{t+1}\}$ we define for the time point t a *score matrix* $\mathbf{S}(\mathbf{x}, t)$ of the same dimensions as the original image:

$$\mathbf{S}(\mathbf{x}_i, t) = \sum_{k=-1,0,1} \begin{cases} \omega^{|k|} \cdot s_i^{t+k}, & \mathbf{x}_i \in P(t+k) \\ 0, & \mathbf{x}_i \notin P(t+k) \end{cases}. \quad (2.5)$$

The parameter $k = -1, 0, 1$ defines the time offset around the central time point t . The weight function between the central time point and the previous and subsequent time points is set to $\omega = 1/e$. In other words, Eq. (2.5) corresponds to an accumulation of all event scores in a time stack, followed by Gaussian filtering, i.e. discrete convolution, along the time axis subject to negligence of filter values smaller than $1/e$. The additional low-pass filtering and hence reduction of resolution in the time domain is minimal. Already the score values at time t are extracted based on line regression of data from one time point before and after t . By applying Eq. (2.5) we therefore add only a small indirect coupling of the kinetic measures in t with those in $t-2$ and $t+2$.

Finally, spatial averaging is achieved for every time point by convolving

$$\mathbf{K}(\mathbf{x}, t) = \mathbf{S}(\mathbf{x}, t) * \mathbf{G}(r, d_0) \quad (2.6)$$

with a Gaussian kernel according to Eq. (2.1). The parameter d_0 is chosen adaptively as the mean distance between adjacent non-zero score values in any of the stack layers $\mathbf{S}(\mathbf{x}, t)$, $\forall t$. This means that the convolution kernel acts as a smooth transient between weighted averaging and interpolation. In areas with a high score density, i.e. several values fall inside the circle with radius d_0 , the convolution takes the role of averaging resulting in more robust kinetic estimates, whereas in areas with only a few scores the kinetic estimates are mainly obtained from interpolation between the nearest score values. If the distances to the nearest score value become larger than $3 \cdot d_0$ the kinetic estimate tends to zero, in correspondence with the infrequent occurrence of speckle birth and death events in such areas. $\mathbf{K}(\mathbf{x}, t)$ provides a continuous and smooth representation of the kinetic activity, and can be employed for further biological analyses (see Results). For display purposes the values in $\mathbf{K}(\mathbf{x}, t)$ are binned into 31 score classes and are stored in a display stack $\mathbf{D}(\mathbf{x}, t)$. The class boundaries were derived from several actin FSM movies, imaged under various experimental parameters. We extracted the range of practically relevant scores and divided it into 31 classes, symmetrically distributed around zero. Graphically, they are presented in color with colors ranging from green to dark blue for depolymerization, and from yellow to bright red for polymerization (see e.g. colorbar in Fig. 2-7 (c)).

Event	Class	Conditions	Ordered kinetics	Score s
Birth	Birth due to (speckle) polymerization	$a_{\text{speckle}} > 0$ $\frac{ a_{\text{speckle}} }{\sigma_{a_{\text{speckle}}}} > \frac{ a_{\text{background}} }{\sigma_{a_{\text{background}}}}$ $\frac{ a_{\text{speckle}} }{\sigma_{a_{\text{speckle}}}} > Q_\alpha$	Polymerization	$s = a_{\text{speckle}} > 0$
	Birth due to (background) depolymerization	$a_{\text{background}} < 0$ $\frac{ a_{\text{speckle}} }{\sigma_{a_{\text{speckle}}}} < \frac{ a_{\text{background}} }{\sigma_{a_{\text{background}}}}$ $\frac{ a_{\text{background}} }{\sigma_{a_{\text{background}}}} > Q_\alpha$	Depolymerization	$s = a_{\text{background}} < 0$
Death	Death due to (speckle) depolymerization	$a_{\text{speckle}} < 0$ $\frac{ a_{\text{speckle}} }{\sigma_{a_{\text{speckle}}}} > \frac{ a_{\text{background}} }{\sigma_{a_{\text{background}}}}$ $\frac{ a_{\text{speckle}} }{\sigma_{a_{\text{speckle}}}} > Q_\alpha$	Depolymerization	$s = a_{\text{speckle}} < 0$
	Death due to (background) polymerization	$a_{\text{background}} > 0$ $\frac{ a_{\text{speckle}} }{\sigma_{a_{\text{speckle}}}} < \frac{ a_{\text{background}} }{\sigma_{a_{\text{background}}}}$ $\frac{ a_{\text{background}} }{\sigma_{a_{\text{background}}}} > Q_\alpha$	Polymerization	$s = a_{\text{background}} > 0$

Table 2-1

2.4 Results

2.4.1 Verification of the algorithm on synthetic data

To prove consistency and stability of the algorithm, it was first tested on synthetic data. Our FSM simulation package allowed us to generate synthetic movies where speckle intensity fluctuations were related to the kinetic activity of a Monte Carlo model of an actin meshwork (see Materials and Methods). The software also integrates imaging parameters, including models for image dark and shot noise, which we could freely turn on and off.

Fig. 2-6 shows the result of such a test. All our synthetic data was analyzed at a 95% confidence level. A homogeneous intensity field of $10 \times 10 \mu\text{m}^2$ was divided into four sub-regions of which each was assigned to a different net assembly rate. The net assembly rate is defined by

$$r = [e^+]_A \cdot (k_{on}^+ \cdot M - k_{off}^+) + [e^-]_A \cdot (k_{on}^- \cdot M - k_{off}^-) \quad (2.7)$$

where $[e^+]_A$ and $[e^-]_A$ denote the area concentrations of the plus (barbed) and minus (pointed) actin filament ends, $k_{on}^{+/-}$ and $k_{off}^{+/-}$ are their respective association and dissociation rate constants and M is the concentration of free actin monomers. The initial intensity was set in the range we usually get from experimental data, assuming uniform spatial distribution of label. The artificial meshwork was then allowed to polymerize and depolymerize according to the local net assembly rate.

Fig. 2-6 (a) shows the reference net assembly rates on a relative scale, where negative values denote disassembly. The output scores calculated by the algorithm are presented in Fig. 2-6 (b) on the same relative scale. The reference assembly rates and the output kinetic scores are in good agreement. This confirms the following three properties of the algorithm: i) in the chosen 95% confidence level, speckles are properly distinguished from intensity variations due to noise (see Algorithm – Statistical selection of speckles); ii) the classification of speckle birth and death events correctly distinguishes between assembly and disassembly (see Algorithm – Classification of birth and death events); iii) despite their inherently stochastic nature, the slopes of the intensity profiles around birth and death reflect, on average, the local kinetic property of the meshwork on a linear, relative scale (see Algorithm – Kinetic analysis).

The scores at the boundaries between the four sub-regions are not sharply defined as the input data. This is due to low-pass filtering in the time and space domain, necessary to

average the scores of several events. The graph suggests that the spatial resolution of our analysis is in the range of 1 – 2 μm given input data using a pixel size of 67 nm expressed in object domain and a 100X / 1.4 NA optics.

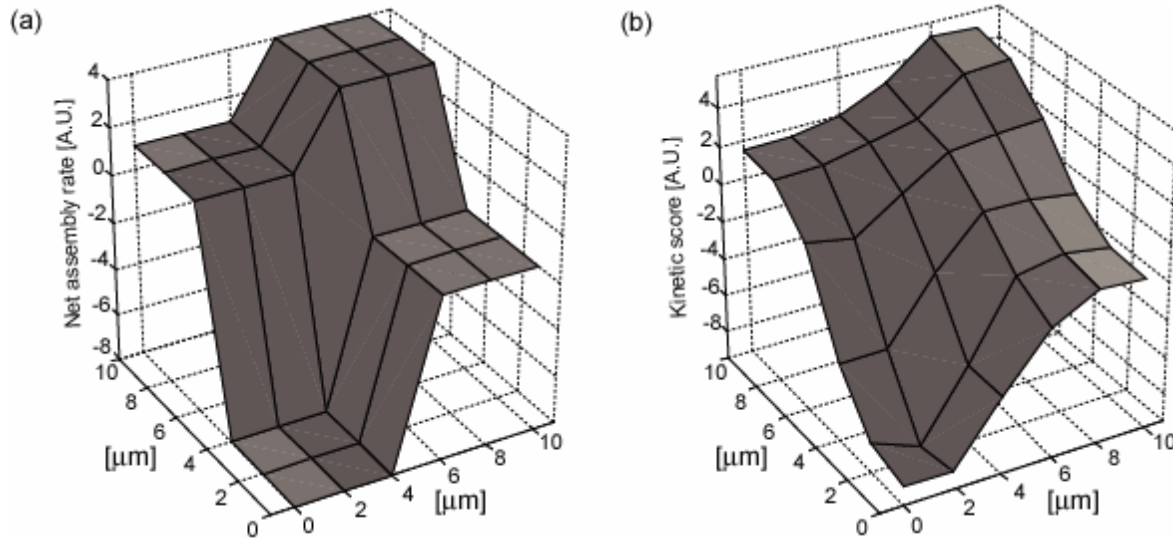


Fig. 2-6

Speckle analysis on synthetic data. Synthetic FSM movies were created based on a model of meshwork assembly and disassembly and well-defined labeling ratios and optical parameters. (a) Net assembly rates (negative values denote disassembly) applied to generate synthetic $10 \times 10 \mu\text{m}^2$ FSM image stacks. (b) The normalized kinetic scores accurately match the input net assembly rates, except for smoothing due to averaging effects in the analysis.

2.4.2 FSM analysis of cortical actin meshworks reveals cyclic polymer turnover

After initial validation, the software was applied to data from live cell experiments. We imaged and analyzed the cortical regions of contact-inhibited newt lung epithelial cells using a spinning-disk confocal microscope system equipped with a cooled CCD detector (see Materials and Methods). X-rhodamine labeled actin was micro-injected into contact inhibited cells in the interior of a monolayer sheet of epithelial cells and $600 \times 600 \text{ pixel}^2$ images were acquired at 5 s intervals. Oxyrase was added to reduce photobleaching effects (Waterman-Storer *et al.*, 1993; Mikhailov and Gundersen, 1995). Fig. 2-7 shows the turnover in the cortical actin at the ventral cell surface, as revealed by our software. The overall distribution of fluorescent actin in the edge region of a cell is shown in Fig. 2-7 (a). Note that the cell is in contact with an adjacent cell (top black region) that had not been labeled with fluorescent actin.

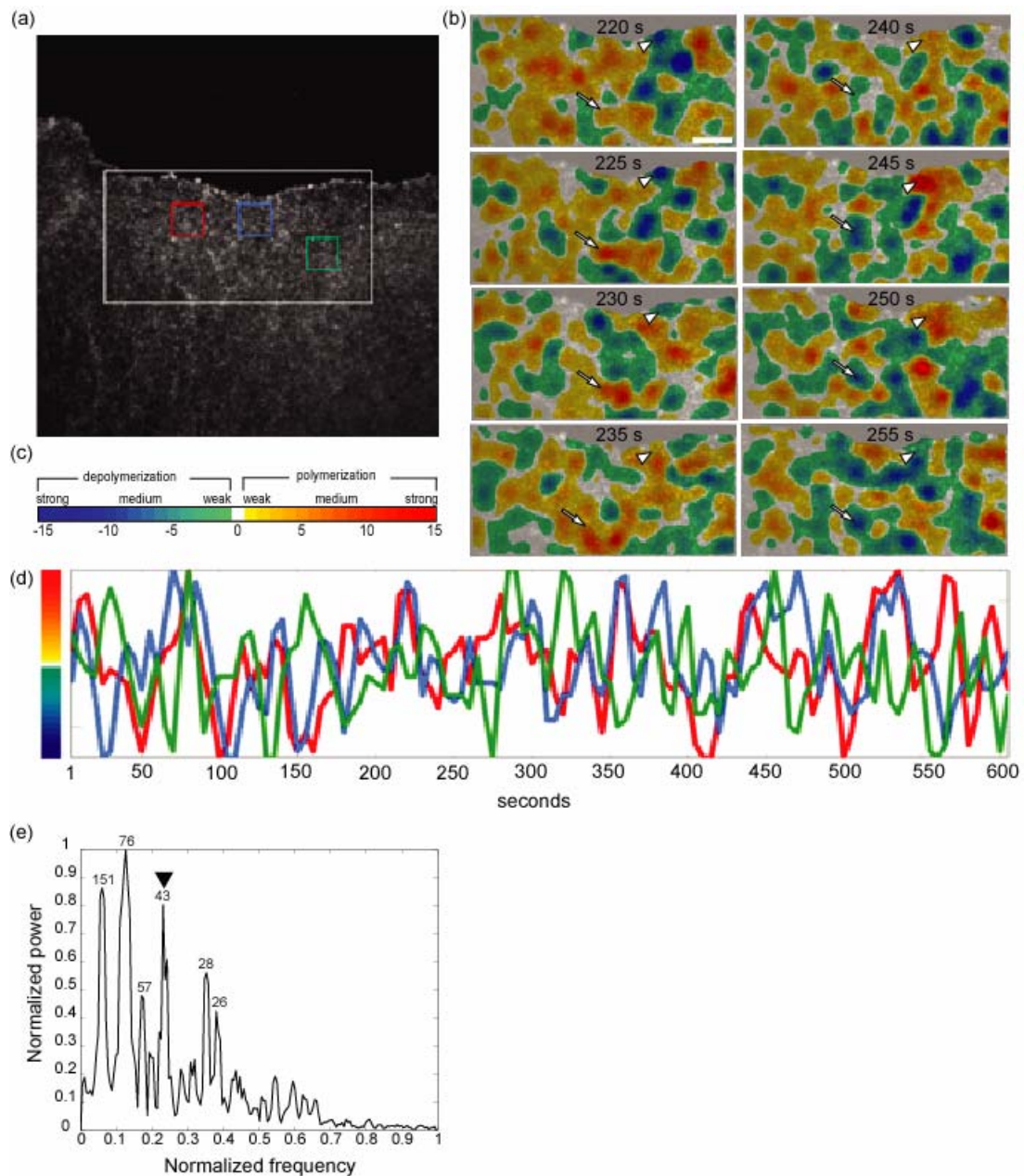


Figure 2-7

FSM analysis of F-actin turnover in the lamellipodium of a newt lung epithelial cell. (a) Overview of the cell area imaged by FSM. The kinetic analysis displayed in (b) refers to the region delimited by the white frame. (b) Eight panels showing kinetic maps over a period of 35 seconds, starting at time point 220s. Two positions are selected to indicate the periodic cycling of the actin meshwork. The arrowhead points to a region cycling from depolymerization to polymerization back to depolymerization. The arrow points to a region where the cycle is 180° phase-shifted. Scale bar, $2.5 \mu\text{m}$. (c) The color map used for displaying 31 score classes in the kinetic maps. (d) The mean kinetic score per unit time and area ($2.5 \times 2.5 \mu\text{m}^2$) over 600 s for three selected regions (see colored boxes in a) reveals a space-independent cycling rate of $\sim 40 \text{ s}^{-1}$. (e) Overall power spectrum of the cycles in (d). The spectrum has three predominant peaks, corresponding to cycling periods of 151 s, 76 s and 43 s. They are approximately in an octave ratio to one another. A second pair found in the data are the 26 s and 28 s periods in octave to the 57 s cycle.

The region overlaid by a white box indicates the area analyzed in Fig. 2-7 (b), which presents 8 consecutive time frames at 5 s intervals of a kinetic map generated by our algorithm. The color coding is illustrated by the scale bar in Fig. 2-7 (c). Strong polymerization corresponds to dark red, strong depolymerization to dark blue.

Although there is an overall equilibrium of polymerization and depolymerization, our analysis reveals alternating polymerization and depolymerization waves in spatially discrete cellular regions. These oscillatory kinetics are illustrated at the positions indicated with an arrow and an arrowhead, respectively. Both positions show a cyclic behavior between states of prevalent polymerization turning into states of depolymerization with subsequent recovery of polymerization. For a position close to the junction with the adjacent uninjected cell (Figure 2-7 (b), arrowhead), the meshwork starts in a state of moderate depolymerization which gets stronger at time point 225 s, weakens again at 230 s and turns into weak polymerization at 235 s. Polymerization peaks 10 seconds later before it weakens again and finally returns in a state of depolymerization (255 s). The position pointed out with the arrow exhibits a similar cycle but starts with weak polymerization.

We conclude that the cortex is divided in small sub-areas of the size of a few μm^2 which polymerize and depolymerize in phase-shifted cycles of similar periodicity. Qualitatively, a similar cyclic behavior can be observed in time-lapse phase-contrast microscopy of contact-inhibited cells in the form of spatial waves in the intensity signal (data not shown). However, the underlying physiological effect was hitherto unclear.

In Fig. 2-7 (d), we further analyze the cycling in three $2.5 \times 2.5 \mu\text{m}^2$ regions indicated in Fig. 2-7 (a) with a red, a blue, and a green box. Independent of the cellular position, the meshwork cycles with a period in the range 35-45 s. Fig. 2-7 (e) underlines this observation with a power spectrum of actin kinetic cycling. The spectrum has three predominant peaks, corresponding to cycling periods of 151 s, 76 s and 43 s. Notice that the first two cycles are almost octave matches to the cycle with the 43 s period. Therefore, they are relatively difficult to observe in the direct spaces revealed by the map in Fig. 2-7 (b) and the graph in 2-7 (d). In addition, the spectral analysis of Fig. 2-7 (e) reveals a second octave pair of frequencies in the turnover cycling (26 s and 28 s which match approximately with the 57s cycle). Interestingly, such cycling has also been observed in the context of lamellipodial protrusion in fibroblasts (Ballestrem *et al.*, 2000). Kymograph analyses of a free leading edge exhibited a transient ruffling at a cycling period of 40 – 50 s, hence in almost perfect agreement with our result. We may conclude that under similar physiological conditions the steady state of an actin meshwork is characterized by an oscillatory turnover, which results in cells with a free

leading edge in lamellipodial protrusion and retraction, whereas in contact-inhibited cells this behavior causes assembly and disassembly of the cortical actin cytoskeleton without cell morphological consequences.

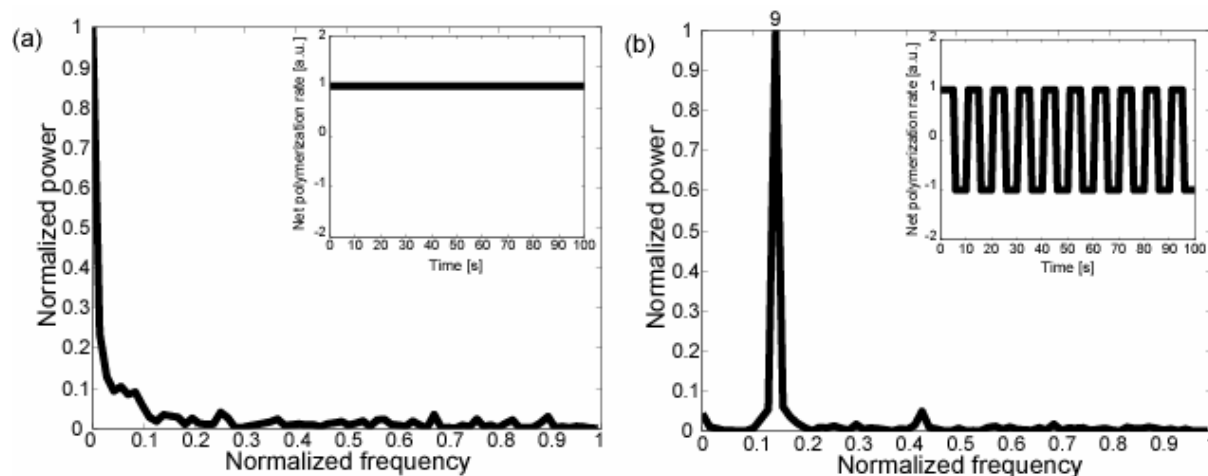


Figure 2-8

Power spectra of synthetic data. (a) Analysis of a meshwork with constant net polymerization (inset). The spectrum is concentrated in the zero (DC) frequencies. (b) Analysis of a meshwork with alternating phases of net assembly and disassembly with a period of 9 s. Here, the spectrum concentrates in a peak at the corresponding frequency.

To verify that the discovered cycling phenomenon is indeed a physiological effect and not an artifact of the analysis, we used our simulation framework to generate steady-state conditions, i.e. for any time interval in the simulation the number of monomers added and removed from a spatial unit was equal. The analysis of such data reported zero activity, as expected (results not shown). In addition, we simulated data where the meshwork was subjected to constant net polymerization, and to kinetics with phases of net polymerization and depolymerization alternating in periods of 9 s (Fig. 2-8). The insets of Fig. 2-8 (a) and Fig. 2-8 (b) show the evolution of the simulated net polymerization rate throughout the two test experiments. Fig. 2-8 (a) shows the power spectrum in the case of constant polymerization. As expected, the spectrum concentrates at the zero frequency (DC). In contrast, the power spectrum of Fig. 2-8 (b) contains a strong peak at a frequency $1/9 \text{ s}^{-1}$, in precise match with the predefined cycling rate between assembly and disassembly of the second simulation. The small fluctuations besides the dominating peaks in both spectra underline again that speckles are a stochastic signal generating various side frequencies, even when the signal represents the outcome of a perfectly deterministic turnover. To conclude, these tests confirm that our algorithm is indeed capable of reporting kinetic events which

occur in regular cycles, suggesting that the results in Fig. 2-7 (e) are very likely to reflect a hitherto unknown behavior of F-actin meshworks.

2.4.3 Latrunculin A perfusion induces a spreading of the cycle frequencies

To study if external perturbations of the actin meshwork activity could be tracked by our algorithm, injected cells were perfused with latrunculin A, a drug known to disrupt the actin cytoskeleton in several mammalian non-muscle cells (Spector *et al.*, 1983). The suggested model of latrunculin A binding to G-actin monomers to form a stoichiometric 1:1 complex (Yarmola *et al.*, 2000) has recently been modified by Pring *et al.* (2002) who suggest the existence of a yet unknown species which participates in the formation of a ternary complex with latrunculin A and G-actin. This puts the effects of latrunculin A into a more complicated context which can eventually be resolved by FSM assaying. Here, we focus on our first observations.

We used a low dose (750 nM) of the drug to prevent catastrophic depolymerization of actin and major morphological changes, which both would have biased our FSM analysis. We expected that a low dose would suffice to shift the cyclic steady state towards actin filament disassembly, or at least to perturb the meshwork cycling. Contact-inhibited cells were first imaged under control conditions (Fig. 2-9 (a) – Before latrunculin-A perfusion) and our analysis software revealed similar behavior as in Fig. 2-7 (e), with discrete regions showing cycling between polymerization and depolymerization of ~166 s (Fig. 2-9 (b)). Notice that each of the frames in Fig. 2-9 shows the score integrated over a 50 s period, i.e. cycle rates faster than 100 s are deliberately obscured. Detailed spectral analysis for this experiment reveals similar peak frequencies as in Fig. 2-7 (e), supporting our speculation about a universal rule for steady state actin turnover under comparable physiological conditions.

In the first panel (50 s) after perfusion of latrunculin A, the tendency for polymerization from the last panel before treatment of the cell continues. Only the second panel after perfusion shows a strong homogenous depolymerization, which is succeeded by continuously stronger re-polymerization already one or two panels (50 – 100 s) later. This means that the system undergoes a relatively rapid recovery. Unfortunately, it was impossible to analyze the cells for more than 200 s because latrunculin A induces cell rounding. Nevertheless, the high sensitivity of our algorithm allowed us to uncover an unexpected effect of latrunculin A treatment. Fig. 2-9 (c) displays the power spectrum of cyclic actin turnover after perfusion. The drug shifts the cycling towards more and higher frequencies.

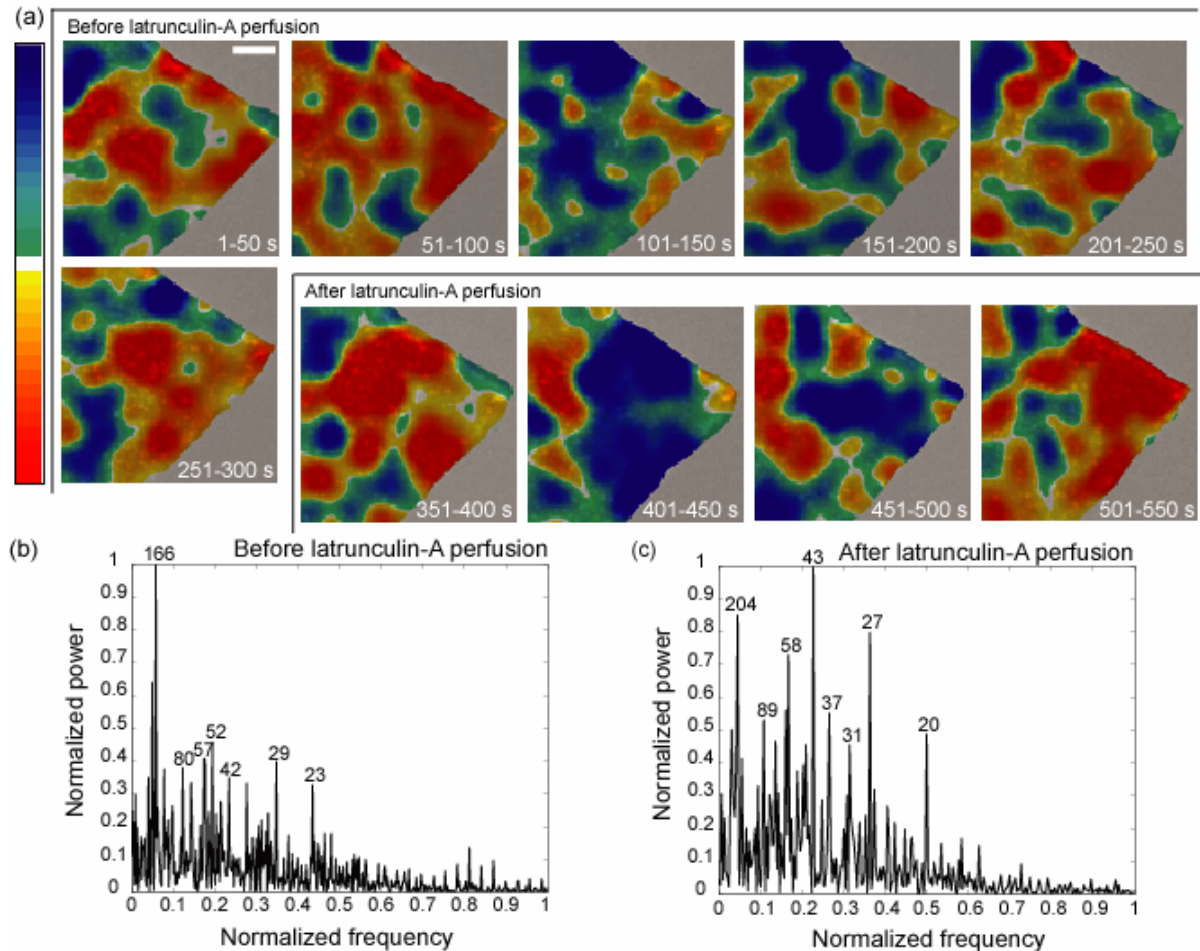


Figure 2-9

F-actin turnover after latrunculin-A perfusion. Cells were first imaged during 300 s under control conditions and then perfused with 750 nM of latrunculin A. (a) Frames showing the scores integrated over a period of 50 s. Scale bar, 2.5 μ m. Comparison of the power spectra before (b) and after (c) latrunculin-A perfusion.

Notice that the DC values of both spectra 2-9 (b) and 2-9 (c) are almost zero, indicating that there is no average tendency for either meshwork assembly or disassembly. In other words, the application of low doses of latrunculin A does not simply cause net depolymerization but the meshwork reacts with a rapid and sustained re-polymerization in many and fast cycles. This can be interpreted as a perturbation leading to higher disorder of the system.

2.5 Discussion

2.5.1 FSM analysis relies on a statistical separation of significant events

In this paper we introduce an algorithm for automated analysis of the assembly and disassembly kinetics of actin meshworks from fluorescent speckle microscopy movies of

living cells. As discussed in the outline of the Algorithm, speckles represent an inherently stochastic and very dynamic signal perturbed by likewise stochastic noise. The core of information extraction from speckle data, therefore, relies on the statistical separation of two stochastic signal components, followed by time- and space-averaging of the component associated with the speckle signal. This reveals statistical trends describing the kinetics of monomer association and dissociation to and from a polymer structure.

The separation of the speckle signal from noise requires modeling the characteristics of both signal components. For the speckle signal we know that it represents a diffraction-limited image of local peaks in fluorophore concentration, which is accounted for by the initial low pass-filtering. The further separation is based on a model of image noise. Three parameters have to be set which are the proportionality factor β for shot noise dependence in image intensity, the dark noise variance α_{DN} and the mean intensity of the dark field (see Eq. (2.2)). The first parameter β has been calibrated once for all relevant exposure times and thus is stored in a software look-up table. The second and third parameters vary between experiments. They must be calibrated for every image series, for which the software operator has to select a small window devoid of speckles. The only parameter that requires manual input is the confidence level α on which all the statistical tests are performed. However, the setting of this parameter is also unproblematic. The statistical selection processes turn out to be very robust for confidence probabilities between 80% and 99% (also see Fig. 2-12 below). Based on these parameters the algorithm performs three essential steps (see Fig. 2-2): i) statistical selection of speckles; ii) statistical classification of speckle birth and death events to ascertain meshwork polymerization and depolymerization; iii) statistical analysis of the intensity development in these events. Time changes in the intensity are, on average, related to the kinetics of monomer association and dissociation.

In a recent paper, Watanabe and Mitchison (2002) used single-fluorophore FSM to quantify F-actin flow and meshwork activity in lamellipodia of fibroblasts. They tracked a few, selected speckles by hand and performed statistical analysis on the lifetime and movement of the speckles. In analogy to the present work, single-fluorophore speckle appearances and disappearances served as local reporters of meshwork turnover. Single-fluorophore FSM has the advantage that every labeled monomer added to the meshwork results in a new speckle, and dissociation of a labeled monomer removes a speckle. Consequently, in this kind of data the speckle lifetime is a direct measure of the kinetic activity. However, single-fluorophore FSM also has disadvantages: i) besides the

experimental challenges of stably imaging single fluorophores, the labeling ratio has to be kept extremely low with the result that the speckle distributions are low density and thus provide limited spatial sampling; ii) the SNR is weak, which requires long exposure times and thus limits the temporal resolution; iii) the speckle appearances and disappearances deliver only binary information, comparable to an on/off switch. To convert this binary data into smooth kinetic rate measures requires substantial averaging in space and time over several speckles, which lowers the resolution of the method further. It is an open question whether single fluorophore speckles could characterize the dynamic equilibrium of a spatially stationary meshwork as reported by Fig. 2-7, where polymerization and depolymerization co-exist in very close proximity, and whether it has sufficient temporal resolution to extract the short-term fluctuations of the equilibrium.

In our multi-fluorophore approach, speckles are the result of local clustering of several monomers perhaps in different filaments within the volume of the PSF. Speckle births and deaths result from a significant change in the local number density of labeled monomers. As discussed in the section Algorithm – Kinetic analysis, the score of an event corresponds to the slope of either the peak or background intensity development, and therefore is a direct measure of the temporal change of the number of labeled monomer at the position of the speckle. Our score delivers more continuous information than the binary answer of a single-fluorophore speckle, and allows us to distinguish with one measurement between a slow and a fast process. Averaging is still necessary for elimination of the inherent variation of the score values, but we believe that much fewer speckles are necessary to obtain a robust kinetic rate estimate.

2.5.2 The effect of bleaching on FSM analysis is minimal and can be eliminated completely by an appropriate correction scheme

To test the robustness of the algorithm against imaging artifacts, we examined the effect of intensity changes due to photobleaching. We performed two experiments on cells that were fixed one hour after microinjection with labeled actin. During this time, the labeled actin was allowed to incorporate into filaments until the equilibrium between free monomers and filaments was established. In fixed cells no actin meshwork activity is supposed to occur. The two protocols differed in the strength of illumination and the use of anti-fading agents. As with all our experimental data the confidence level α was set to 95% for both experiments.

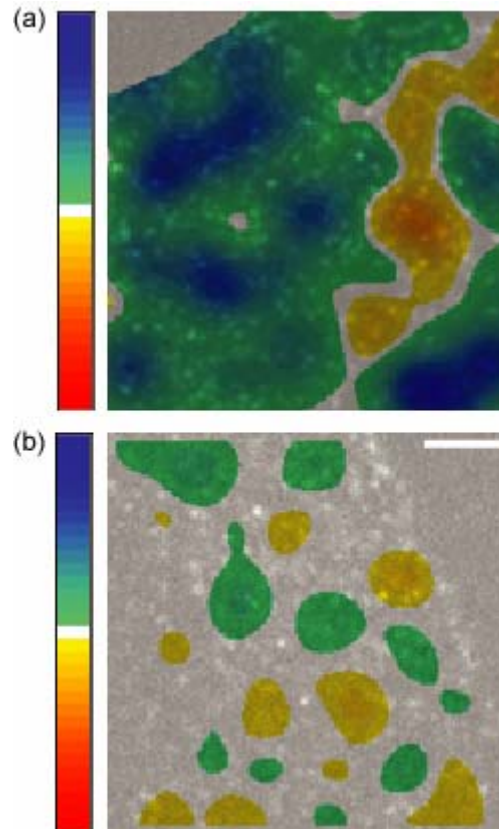


Figure 2-10

Effects of intensity changes due to photobleaching tested on fixed newt lung epithelial cells with a speckled actin cytoskeleton. (a) An exposure time of 10 s per image induced strong bleaching represented by green to dark-blue areas. (b) An exposure time of 5 s and the addition of Oxyrase as an antifading agent reduced the bleaching dramatically. Scale bar, 2.5 μm .

Both actin disassembly and photobleaching lead to a decrease of labeled monomer and thus we expect the software to have its report biased towards depolymerization. In the first experiment, the fixed cells were imaged under strong illumination conditions. The exposure time was set to 10 s and no anti-fading agents were applied. Strong bleaching was the result and we expected the software to return kinetic maps indicating mostly depolymerization. This is largely confirmed by Fig. 2-10 (a). Most parts of the cortical meshwork show strong depolymerization, with the exception of one region where the reported trend is the opposite. A thorough analysis of the raw FSM movie revealed that in this area new speckles occurred with an increasing absolute peak intensity (data not shown). At the moment the origin of this imaging artifact is unclear.

The panel Fig. 2-10 (b) shows the analysis of an experiment with more moderate exposure times and where Oxyrase was added to reduce bleaching. The exposure time was set to 5 seconds, which is still higher than the 2 to 3.5 seconds of our live cell imaging protocol.

Again, depolymerization as well as some artifactual polymerization events are reported by the software. Notice, however, the large reduction of the scores as compared with the first experiment. This indicates that the majority of the map in Fig. 2-10 (a) is indeed associated with fluorophore bleaching. The scores cover only the lowest kinetic classes, which means that under regular exposure time and under the application of anti-fading agents, the effect of bleaching on FSM analysis is minimal. analysis of live cell experiments, we analyzed the distribution of positive and negative scores from the weak bleaching experiment in comparison to the score of the data set shown in Fig. 2-7.

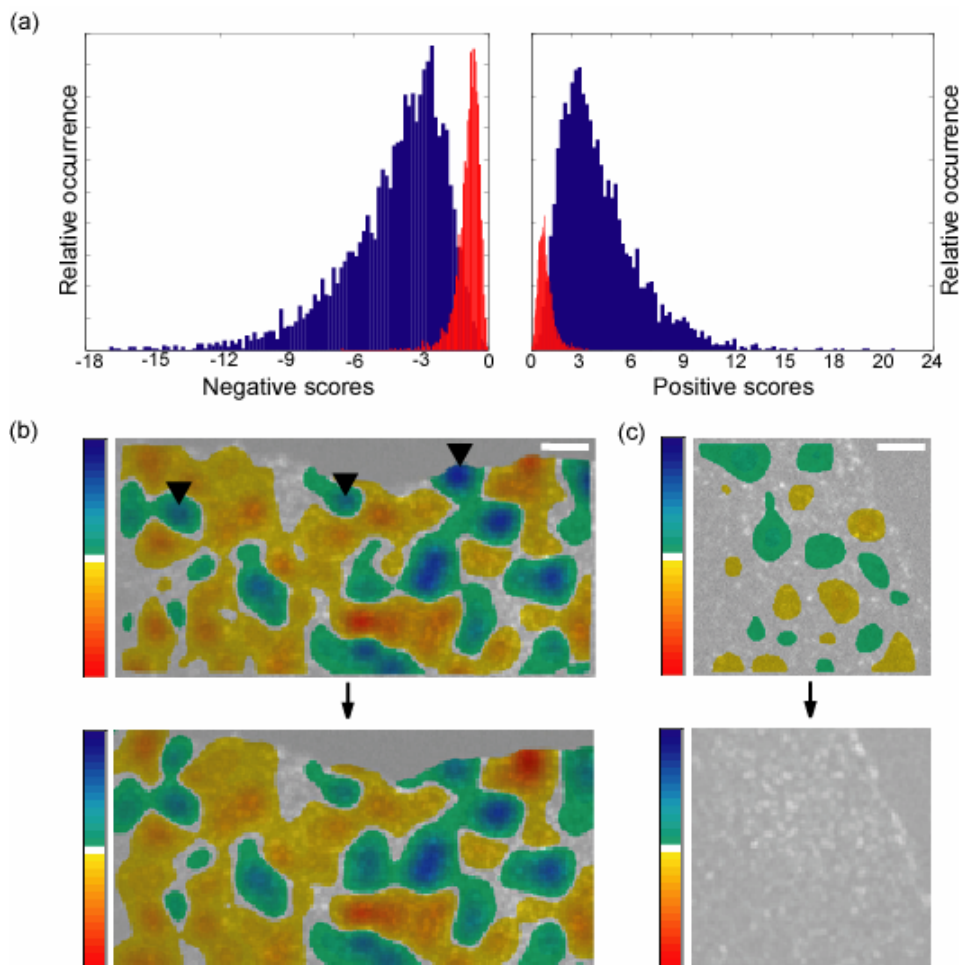


Figure 2-11

(a) Characterization of bleach-induced scores (red) relative to scores measured in live cell experiments (blue). The score distributions are clearly distinct, so that score biases due to bleaching can be compensated (see text for a description of the bleaching correction). (b) Bleaching correction applied to an uncorrected panel of Fig. 7 and (c) to Fig. 10 b. The maps show that the correction indeed eliminates the marginal bias induced by bleaching; however, it does not change the quality of kinetic maps from live cell experiments. The arrowheads in b indicate some depolymerization scores that are slightly diminished by the bleaching correction. Scale bars, 2.5 μm .

Nevertheless, bleaching is a systematic effect and hence could be eliminated from the analysis by an appropriate correction scheme. To test the extent to which bleaching affects the Fig. 2-11 (a) shows the relative occurrences of bleach-induced scores (red histogram) overlaid to the scores measured in a live cell experiment (blue histogram). The two histograms clearly differ, which means that scores due to bleaching can be eliminated. Thus, we supplemented the algorithm with an entirely data-driven bleaching compensation module: from the modes of the two red histograms the module automatically derives thresholds that discriminate weak scores due to bleaching from scores related to F-actin meshwork turnover. After removal of weak scores the kinetic map is recalculated according to the filtering and interpolating scheme discussed in the section Algorithm – Kinetic Analysis. Fig. 2-11 (b) and (c) display the effect of such correction. In agreement with the conclusions above, changes in the map due to the bleaching correction are very minimal and almost only visible for areas with strong depolymerization that get slightly diminished (arrowheads in Fig. 2-11 (b)). The reason for this minimal effect originates in the strategy of analyzing the speckle intensity development only over short time intervals around birth and death events. It implies that the intensity changes exploited are systematically several-fold larger than intensity changes associated with bleaching over such time spans. To demonstrate the self-consistency of the correction scheme, we display in Fig. 2-11 (c) a bleach-corrected version of the map in Fig. 2-10 (b). Indeed, the scheme removes all scores from the map, indicating that our analysis correctly reports no meshwork activity for a fixed cell.

2.5.3 The effect of focus changes

In addition to intensity variations due to bleaching, focal shifts may mistakenly lead to false birth and death events. We can think of two types of focal changes. On the one hand, *single speckle axial motions* occur, which affect the intensity development of one speckle independent of any other speckle. They are a stochastic process on average leading to the same amount of birth and death events. Therefore, their contribution to the score cancels out by averaging. On the other hand, a *coordinated axial shift of many speckles* may occur. Origins of such motion are z-stage drifts and vertical movements of entire cell parts, as for example induced by contraction. The first problem could be reduced by means of sophisticated closed-loop stage controllers (Lanni, 1993), which were, however, not used for data acquisition in this paper. Unfortunately, the second problem is out of our experimental control.

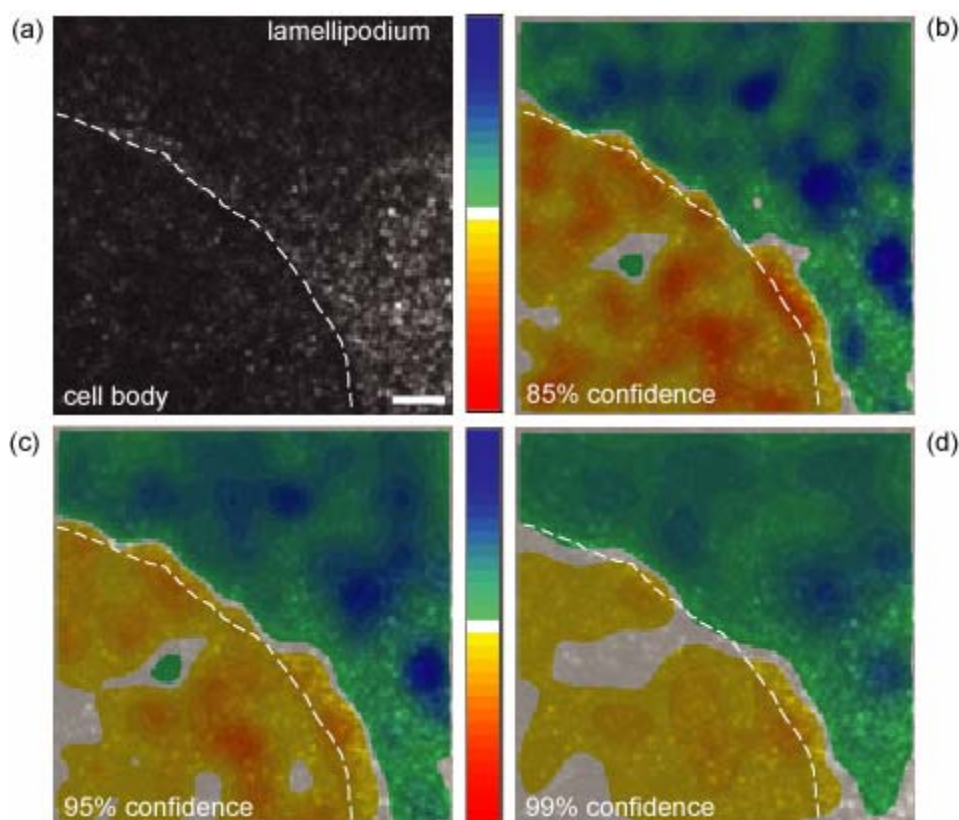


Figure 2-12

Characterization of kinetic scores induced by focal shifts. Fixed cells with a speckled actin cytoskeleton were imaged in a series, at 3-s exposure time and with Oxyrase added, where the focus was changed in steps of 100 nm between frames. (a) Overview of the cell indicating the transition between the thick cell body and the much thinner (~200 nm) lamellipodium. Panels b–d show the kinetic maps calculated at the confidence levels $\alpha = 85$, 95, and 99%. Scale bar, 2.5 μm .

To quantify the sensitivity of the algorithm to coordinated z-motion, images of fixed newt lung epithelial cells were acquired at 100 nm z-intervals using a stepper motor focus controller. These cells were not contact inhibited, as revealed by the presence of a large lamellipodium. In accordance with the parameters of live cell experiment the exposure time was set to 3 s and Oxyrase was added to reduce photobleaching.

Fig. 2-12 (a) gives an overview, where the transition from the very thin lamellipodium to the thicker cell body is highlighted. The thickness of lamellipodial actin sheets has been quantified in the range of 200 nm by Abraham *et al.* (1999). Hence, we anticipate that 100 nm stage shifts have a significant effect on the scores in the lamellipodium, whereas the much thicker cell body should be more insensitive towards such shifts. Depending on the position of the focus plane relative to the heights of cell body and lamellipodium, a result like the one in Fig. 2-12 (b) – (d) can be expected. The movement causes positive scores for the cell body

(Fig. 2-12 (b) – (d)), where new speckles enter the focus plane, and negative scores for the lamellipodium, where a 100 nm step induces almost complete disappearance of all speckles. However, the drift effects are significantly lower for the cell body area, where a certain “random symmetry” in the vertical speckle distribution leads to an averaging effect. This becomes particularly obvious with alterations of the confidence probability. Fig. 2-12 (b) – (d) illustrates the dependence of the scores on the choice of α . The higher the confidence, the lower is the risk of including artifactual events into the score analysis. At 99% confidence, scores for the cell body are almost exclusively in the two lowest score classes (faint yellow), while at 85% a considerable amount of false events is collected. Nevertheless, the series also indicates that the general trends of the maps are unaffected by the setting of the confidence probability and thus that the algorithm is very robust in reporting the main characteristics of polymer turnover.

We conclude from this data that uncontrolled focus drifts have a dramatic effect on the extraction of kinetic measurements. However, the drift rates applied to the data shown in Fig. 2-12 are far beyond what is encountered in live cell experiments. Such drifts have never been observed in real experiments, where an operator visually supervised the image acquisition and small focus corrections were applied manually approximately every 20 – 30 frames. There is a second reason why we believe that our live cell experiments are only minimally perturbed by focus drifts. As evident from Fig. 2-12, focus drifts cause coherent score drifts over large areas of the field of view. In none of our cell experiments have we observed such spatially homogeneous score maps, but the maps were always highly structured as in the data shown in Fig. 2-7. Finally, the data examined in Fig. 2-10 (b) contains, in a strict sense, a super-position of bleaching and focus drift effects, as these bleaching series were acquired in the same manner as any other data set, i.e. with manual compensation of focus drifts. With Fig. 2-11 we demonstrate that these biases can be appropriately eliminated.

2.5.4 Local meshwork contractions are most likely to result in ghost speckles which are excluded from the analysis

There is a third potential source of error in our analysis originating in motor-induced local meshwork contraction. While positional fluctuations of speckles induced by such contraction are properly accounted for (see Algorithm – Micro-movement tracker), contraction and subsequent release of the meshwork can also cause the formation of new speckles and the dissolution, fusion and splitting of existing speckles. In all of these situations our software is likely to detect the birth or death of a speckle which is not associated to

meshwork turnover. As with the axial motion of single speckles in and out of focus, these are stochastic events with zero mean score that average out by appropriate spatial and temporal filtering. The kinetic map in Fig. 2-7 suggests a cyclic turnover of actin with a cycling period of 30 s and more. Therefore, a time window of up to 15 s could be used to eliminate artifactual birth and death events from the analysis without obscuring the kinetic behavior of polymerization and depolymerization. As indicated by Eq. (2.5), our temporal averaging was more conservative. We limited the averaging to three time-points in 5 s frame rate data, which corresponds to a time window of 10 s.

Our data provides clear evidence that contraction-related speckle appearances and disappearances even take place in rates much faster than with a period of 10 s. Besides the data presented in the Figures of this paper, which was consistently acquired at 5 s intervals between frames, we have also analyzed movies with frame rates of 1 s, 3 s, and 10 s. On the one hand we examined the number of ghost speckles as a fraction of the total number of extracted speckles. For all movies and independent of the frame rate it was in the range 40% to 50%. We can exclude that these large numbers of ghost speckles are due to noise. All our images are carefully low-pass filtered and speckles are subsequently selected on a confidence level between 80% and 99%, allowing a maximum of 20% insignificant local maxima that are falsely detected as speckles. Consequently, ghost speckles do represent a significant signal with a lifetime shorter than the currently achievable acquisition rate of 1 s. On the other hand, we compared the power spectra of polymer turnover between the movies and found no additional peak when increasing the frame rate, suggesting that indeed all major polymerization-related cycles are retrieved by our computational analysis of 5 s data. We conclude that ghost speckles are not related to meshwork turnover and hence are likely the product of fast local meshwork contraction. There is further support for this argument by the fact that ghost speckles have, on average, an intensity 1.5 to 2.0 times lower than the intensities of speckles living over more than one time-point. Even with only 1 s frame rate the exposure time necessary for FSM image acquisition amounts to almost 1 s. Fast local meshwork movements induced by contraction would cause a smear of the signal that is in agreement with the observed intensity reduction. Since ghost speckles are not included in the score analysis it seems very likely that our system is largely unaffected by the meshwork contraction. Nevertheless, an extended series of experiments with ATP depleted cells and controls with inhibitors of myosin activity and polymerization is planned for the future in order to provide a conclusive proof of this argument.

In summary, we have developed a completely automatic and robust software which maps the kinetics of spatially stationary F-actin meshworks in living cells injected with fluorescent actin and imaged by FSM, by analyzing every speckle as a local reporter of meshwork turnover. Applications of this novel quantitative FSM are manifold. They range from fundamental studies of polymer dynamics *in situ*, the analysis of mechanisms mediating cell migration and morphogenesis, to very sensitive high-content screening of drugs and regulators affecting the cytoskeleton dynamics. In near future, we will combine this program with a module for tracking large scale speckle movements, which will enable us to map cytoskeleton kinetics and translocation dynamics at the same time.

2.6 Acknowledgements

Supported by Swiss National Science Foundation 21-59452.99 to G.D., the National Institutes of Health (GM 61804-01 to C.M.W.-S., and a collaborative Young Investigators Award from the Human Frontiers Science Programme to C.M.W.-S., G.D., and Inke N athke (University of Dundee).

3

Recovery, Visualization, and Analysis of Actin and Tubulin Polymer Flow in Live Cells: a Fluorescent Speckle Microscopy Study

3.1 Introduction

Extended polymeric structures such as the actin and microtubule cytoskeletons are pervasive in eukaryotic cells. They are in particular responsible for the generation of cell polarity, movement, and morphogenesis, for organizing cell division and cellular organelle transport, as well as for ensuring cell mechanical integrity (Alberts *et al.*, 2002). In addition, defects in cytoskeletal function have been implicated in many diseases, for example in vascular diseases (Wesselman and De Mey, 2002), neuronal degeneration (Brandt, 2001; Garcia and Cleveland, 2001), and cancer (Condeelis *et al.*, 2001; Thiery and Chopin, 1999).

When very low amounts of a fluorescent derivate of the monomer forming actin filaments and microtubules (G-actin and tubulin, respectively) are introduced into a living cell, the cytoskeletal polymer assembled from the mixture of endogenous and fluorescent monomers acquires a speckled appearance in high resolution, high magnification fluorescence microscopy digital images (Waterman-Storer and Danuser, 2002). The speckles correspond to diffraction-limited regions where, statistically, more labeled monomers have polymerized into the underlying structure than in the immediate neighborhood. In time-lapse Fluorescent Speckle Microscopy (FSM) the movement and appearance/disappearance of speckles act as local reporters for the translocation (i.e. flow), and assembly/disassembly (i.e turnover) of polymer. Since the discovery of this effect (Waterman-Storer *et al.*, 1998), FSM has been applied in various contexts, including: in vitro analysis of microtubule treadmilling (Grego *et al.*, 2001); in vivo studies of mitotic spindles in cells and cell extracts (Maddox *et al.*, 2000; Waterman-Storer *et al.*, 1998); the analysis of microtubule transport along axonal shafts (Chang *et al.*, 1999); investigations of the actin cytoskeleton dynamics in stationary and migrating cells (Watanabe and Mitchison, 2002; Waterman-Storer *et al.*, 2000a); the dynamic relationship of the actin and tubulin cytoskeletons (Gupton *et al.*, 2002; Salmon *et al.*, 2002; Schaefer *et al.*, 2002; Waterman-Storer *et al.*, 2000b); and the study of microtubule-associated proteins (Bulinski *et al.*, 2001; Kapoor and Mitchison, 2001; Perez *et al.*, 1999).

There are at present no techniques besides FSM having a similar potential to deliver dynamic information on cytoskeletal flow and turnover activities over extended areas of the cell. FSM however is still in its infancy. A particular challenge consists in the complexity and sheer volume of the data. In time-lapse FSM image series, thousands of weak contrast speckles exhibit movement. Also, new speckles may pop up unexpectedly or speckles can disappear at any time. Speckle appearance and disappearance can potentially be exploited to analyze local polymer turnover, but they interfere heavily with our ability to recover flow

information. The relationship existing between the true, continuous flow of the viscoelastic cytoskeletal media and a set of time-lapse speckle images, perturbed by the various effects enumerated above, is far from trivial. Hence, we use the term “flow recovery” throughout this contribution.

3.1.1 FSM of filamentous actin flow at the leading edge of migrating cells

Migrating cells in culture are polarized, with a broad flat lamellum that terminates in a ruffling lamellipodia facing the direction of migration (the leading edge). A meshwork of actin polymerizes at the leading edge and flows retrogradely towards the cell body (Wang, 1985). The nucleation and growth of actin filaments (F-actin) into a cross-linked and branched meshwork is thought to drive forward protrusion of the cell membrane (Mogilner and Oster, 1996), while retrograde flow, if coupled to substrate adhesion, is thought to generate lamellipodial traction.

Recently, we proposed a computational framework for the analysis of F-actin turnover in non-migrating, contact-inhibited cells (Chapter 2), where the leading edge F-actin assembly and retrograde flow are shut down. Nevertheless, FSM movies of such cells still showed a photometric activity of fluorescent speckles in the non-moving cortical actin, indicating that F-actin is undergoing steady turnover (Waterman-Storer *et al.*, 2000a). The algorithm relied on the statistical evaluation of speckle intensity fluctuations coupled with speckle appearance and disappearance.

In the present contribution, we address how speckle movements can be exploited to map the retrograde F-actin flow in a migrating cell. The task is complicated by the high variability of the speckle signal, which is typically near the noise level of the imaging system, and by the presence of speckle sources and sinks, associated with either regions of polymerization and depolymerization, or contractile centers formed by myosin motor proteins. Such singularities are clearly visible in the results produced by our new tracker. We are also able to confirm findings concerning the organization of F-actin flow in migrating newt lung epithelial cells, which were up to now only inferences from sparse kymograph analyses on small data sets. Finally, we show that significant, coherent changes in the flow pattern can occur on a time scale of seconds; a result which is not surprising considering the ability of motile cells to respond remarkably rapidly to changes in their environment.

3.1.2 FSM of poleward microtubule flux in mitotic spindles

Another exciting application of FSM is the study of microtubule dynamics in the mitotic spindle. This is a complex machine composed of two polar arrays of microtubules, motor proteins, and other molecules (Karsenti and Vernos, 2001; Wittmann *et al.*, 2001b). During mitosis, the spindle assembles around the duplicated chromosomes and distributes them equally to the daughter cells. Each of the two spindle poles initiates the growth of microtubules that overlap to form the central spindle. Growth occurs at microtubule plus ends oriented distal from the poles. Some overlapping microtubules form bundles of inter-polar spindle fibers (cf. also Fig. 3-6 (a)). A second class of bundles link chromosomes to the spindle poles. The plus ends of these microtubules attach to the centromeric DNA via a specialized organelle, known as the kinetochore (Bloom, 1993). At metaphase, chromosomes become aligned at the spindle equator with kinetochore bundles symmetrically extending from sister chromatids towards the corresponding pole. The mitotic checkpoint senses the bipolar attachment for all pairs of sister chromatids and regulates the onset of anaphase, when sisters separate and are moved by their kinetochore microtubule bundles to opposite poles.

A major dynamic aspect of microtubule assembly in the spindle is a steady poleward flux of microtubules toward their poles that occurs at the same rate as minus end depolymerization (Mitchison, 1989; Mitchison and Salmon, 1992; Sawin and Mitchison, 1991). At metaphase, the net rate of polymerization at plus ends equals the flux rate and the spindle achieves a constant steady-state length. Flux may be produced by microtubule treadmilling mechanisms (Margolis and Wilson, 1991) or driven by one or more of the many microtubule motors associated with the spindle (Desai *et al.*, 1998; Kapoor and Mitchison, 2001; Mitchison, 1989). Flux appears important for aligning chromosomes at the spindle equator during metaphase and for generating the tension required to inactivate the spindle checkpoint (Kapoor and Compton, 2002). In anaphase, polymerization at kinetochores mostly ceases and flux can make a major contribution to the movement of chromosomes to their poles (Desai *et al.*, 1998; Maddox *et al.*, 2000).

Although microtubule flux is now easily visible with time-lapse FSM (Waterman-Storer *et al.*, 1998), most of the information captured by such movies has remained unexploited because of a lack of appropriate data processing tools. Indeed, analyzing the kinetics of poleward microtubule flux in mitosis is particularly challenging because of the complex and densely interleaved, anti-parallel motion of fluorescent speckles associated with the two opposing and overlapping bipolar arrays. Hence, flow recovery has to be achieved at

the level of single speckles. Each speckle is treated as a local reporter of microtubule flux, independent of any other speckle in the neighborhood. Ambiguities during tracking are the rule rather than the exception and a framework able to resolve these conflicts for thousands of speckles simultaneously has to be used. As with FSM of actin, a speckle tracker has to cope with disappearances and the formation of new speckles. These demands exceed the capability of any existing single particle tracking method, justifying the developments presented in this contribution.

3.1.3 Scope of the paper

In this paper we present the first results obtained with our novel single particle tracking algorithm. The software proceeds in four steps: i) particle generation, i.e. the selection of significant speckles; ii) generation of candidate matches, i.e. a set of possible speckle displacement vectors between successive frames; iii) scoring of candidate matches based on rules defining the variability of speckles in position and intensity. Probable matches get high scores, improbable ones get low scores; iv) selection of the candidate subset with maximum global score and no topological ambiguity, i.e. none of the speckles is allowed to participate in two trajectories. In the current state, the program delivers the displacements of thousands of speckles between consecutive frames while coping with the unexpected appearance and disappearance of speckles. The algorithm can also deal with anti-parallel motion of proximate speckles. This allows us not only to quantify the interleaved flux fields of bipolar spindles, but also to resolve shear flow in contraction areas of actin meshworks.

An obvious next use of the speckle tracker will be to combine displacement data with appearance and disappearance data to calculate trajectories for every speckle and to perform speckle lifetime analysis for moving polymers in the manner we have shown for spatially stationary F-actin assemblies (Chapter 2). This development is currently underway. Here we focus on the recovery of flow fields from the tracking data. Detected displacement matches are averaged in space and time to map the overall polymer transport, reducing the effect of various random displacements superimposed at the single speckle level.

To demonstrate the power of the data from the tracker for future applications of quantitative FSM, we include various statistical analyses of speckle flow towards opposite poles within the spindle. In particular, the classification of speckles with respect to their direction of movement within the spindle reveals the spatial distribution of the two overlapping microtubule sub-arrays. This is a piece of information hitherto inaccessible and prototypical of what can now be systematically examined with single speckle tracking. We

also obtained measurements indicating that flux is slower for kinetochore microtubules than for non-kinetochore microtubules. We interpret this heterogeneity as the result of tension at kinetochores. Such findings augur a new era in the exploitation of FSM data for quantitative cytoskeleton biology.

3.2 Materials and methods

3.2.1 FSM of actin in migrating newt lung epithelial cells

Primary cultures of epithelial cells were established on 22x22 mm #1.5 coverslips from *Taricha granulosa* lung tissue and maintained in Rose Chambers as previously described (Reider and Hard, 1990). X-rhodamine-labeled chicken skeletal muscle actin was prepared as described (Waterman-Storer, 2002). Migrating cells at the edge of the epithelial sheet that extends from the lung explant were microinjected with 1 mg/ml X-rhodamine G-actin in G-buffer (2 mM Tris, 0.2 mM CaCl₂, 0.2 mM MgATP, 0.5 mM β -mercaptoethanol, pH=8). Following microinjection, cells were allowed to recover for 1-2 hours in the dark before being mounted on slides with double stick tape in culture media containing 0.3-0.6 U/ml Oxyrase (Oxyrase, Inc., Mansfield Ohio) to inhibit photobleaching during imaging. Digital images were obtained at 10 s intervals with a 12 bit Hamamatsu C-4880 camera containing a Texas Instruments TC-215 charge coupled device (CCD, with 12 μm^2 pixels) cooled to -40°C on the multimode microscope described in (Salmon *et al.*, 1998) using a 60x 1.4 NA objective, a 1.25x body tube magnifier, and a 1.5x optovar and epifluorescence filters for x-rhodamine. Excitation illumination was blocked between camera exposures with an electronic shutter.

3.2.2 FSM of mitotic spindle in *Xenopus* eggs extracts

Metaphase spindles with replicated mitotic chromosomes were assembled in meiotic *Xenopus* egg extracts as described (Desai *et al.*, 1998; Murray *et al.*, 1996; Waterman-Storer *et al.*, 1998). For FSM of microtubules, a low level of X-rhodamine labeled tubulin was introduced into the *Xenopus* egg extracts before spindle assembly and FSM was performed as described (Waterman-Storer *et al.*, 1998) by wide field microscopy using a Nikon (Melville, NY) E600 upright microscope equipped with a 60x, 1.4 N.A. Plan Apoformat bright field objective lens with no intermediate magnification and a multiple bandpass dichromatic filter which allowed sequential acquisition of blue (DAPI stained chromosomes) and red (X-rhodamine-labeled tubulin in microtubules) fluorescent images in register on the detector of a

Hamamatsu Orca 1 cooled charge coupled device camera. Metamorph software (Universal Imaging Corp., West Chester, PA.) was used to control illumination through a dual filter wheel (excitation wavelength and intensity), and shutter, specimen focus via a stepping motor (Nikon), and image acquisition. Pairs of fluorescence images were collected at 10-s intervals with exposure times of 500 ms.

3.3 Algorithm

3.3.1 Signal preconditioning

Because the resolution of optical microscopes is limited to roughly 250 nm due to diffraction, signals displaying significant variations over distances shorter than this limit must originate from noise of e.g. electronic origin. This noise can be removed without compromising the speckle signal by low-pass filtering every image with a Gaussian convolution kernel of a full width at half maximum equal to 250 nm, expressed in pixel dimensions (Chapter 2). Note that speckles represent the diffraction-limited image of a random distribution of fluorophores. Thus, the pattern does not contain significant spatial frequencies beyond the optical cut-off, i.e. our low-pass filter strictly suppresses noisy features only. Omitting this preconditioning, the number of local intensity maxima in the image, later identified as potential speckles, would be much higher. Moreover the apparent movement of the noisy features removed would bear no connection with the physical flow.

3.3.2 Particle generation

In particle tracking methods, the complexity inherent to an image is condensed into a set of discrete features with associated properties. Here, these properties are the speckle coordinates and their intensities. We generated these particles from the images by applying a local maximum detector, such that a particular pixel is detected as a maximum whenever its intensity is higher than every pixel around it. Each particle was stored in an array, containing the coordinates and the corresponding intensities.

3.3.3 Particle selection

Particles produced up to this point are still likely to be the result of noise. In the preconditioning step, we have only suppressed noise components corresponding to spatial frequencies higher than the diffraction limit. The components with spatial frequencies below this limit are still present and interfere with the speckle signal. Thus, a further selection is

performed. We apply a statistical selection scheme to only keep those speckles (here, particle and speckle are equivalent terms), whose peak intensities are significantly higher than the local background intensity. Details on how we estimate the local background of each speckle and how we test the significance of peak intensities against noise are described in Chapter 2, (2003).

3.3.4 Generation of candidate matches

Over time, speckles move continuously along with the intracellular cytoskeletal flow. Because time-lapse images deliver only discrete snapshots of this flow, speckles in one frame have to be re-identified in the consecutive frame. Because speckles can appear, disappear, fuse and split, this correspondence search is far from trivial, even at high image sampling rates.

The speckle flow has a finite maximum speed over the duration of an FSM movie. Together with the sampling rate, this defines the maximum displacement d that a speckle can undergo from one frame to the next. It is fairly easy to visually estimate an upper limit for this distance. Omitting the use of this *a priori* information, the number of potential matches to consider would be overwhelmingly large. Hence, for each speckle we store every neighboring speckle within the distance d in an array M , such that each row of this array consists of the two position vectors $[\mathbf{r}_k, \mathbf{r}_{k+1}]$, with $\mathbf{r}_k = [r_{k,x}, r_{k,y}]$. Here, \mathbf{r}_k denotes the position of a source speckle in frame k , and \mathbf{r}_{k+1} denotes the position of a potential target speckle in the frame indexed by $k+1$.

3.3.5 Selection of matches

The essence of particle tracking methods is that particles are indivisible and that they retain their individuality even when they come very close. In that sense, the notion of a particle does not capture every aspect of a speckle because nothing prevents two speckles from fusing in an FSM sequence. This happens particularly in regions of flow convergence, where speckles are squeezed into a volume below the optical resolution of the microscope, compelled to do so, for example, by cytoskeleton contraction.

However, by analyzing some sample data manually, it appeared that fusion or splitting of speckles were rather rare events in the polymer assemblies we studied. Moreover, ignoring fusion and division allowed us to use a standard method from operational research to recover the speckle correspondences between frames. Specifically, the correspondence search selects a sub-array of M such that:

- A source speckle at time k is matched with at most one target speckle at time $k+1$.
- A target speckle at time $k+1$ is matched with at most one source speckle at time k .
- The matches are selected according to heuristic rules, describing the a priori likelihood of potential actions of speckles between consecutive frames.

Condition c) determines the quality of particle-to-particle correspondence, and thus imposes local constraints on the selection of matches. Items a) and b) formulate conditions for the global topology of all matches. Whereas many particle tracking systems employ some sort of similarity measure to define the correspondence, they resolve topological conflicts at best with an *ad hoc* scheme. Topological conflicts occur, for example, when two speckles in frame k would have their best match with the same speckle in $k+1$, violating rule a) above. In this case, the algorithm has to decide which of the two is permitted to link to the over-booked target speckle, and how the losing speckle re-participates in the competition for another speckle.

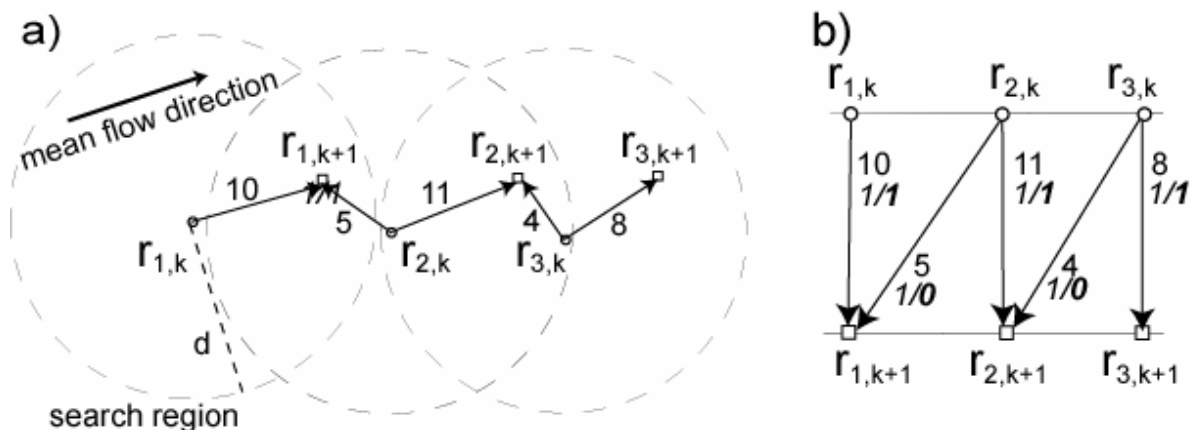


Figure 3-1

Applying graph concepts to tracking problems. (a) Speckles at time point k (small circles), move to new positions (squares) at time point $k+1$. (b) Translation of candidate matches into edges of a graph which defines all possible topologies for linking the speckles. In terms of graph theory, speckles represent vertices arranged in two layers. Only those matches are considered which fall into the search area of the corresponding speckle (dashed circles in A). Costs equal to the distance separating speckles are attached to the graph edges (numbers in regular font). Capacities of edges are all equal to one (first number in italic font). Not more than one unit of flow can leave from any of the source vertices, or flow into a target vertex. Pushing a maximum amount of flow through the graph at minimal cost yields the matches selected by the tracker. In the case shown, the correct solution is chosen (edges with an effective flow 1, see second number in bold-italic font), at a cost of 29. A nearest neighbor matching scheme would result in a cost of 9, but would violate the condition of maximum flow.

Another example of a topological conflict is illustrated in Fig. 3-1 (a). Three speckles, indexed by $\mathbf{r}_{1,k}$, $\mathbf{r}_{2,k}$ and $\mathbf{r}_{3,k}$, translate to their new positions, indexed by $\mathbf{r}_{1,k+1}$, $\mathbf{r}_{2,k+1}$, and $\mathbf{r}_{3,k+1}$. Frequently, particle tracking methods use a nearest neighbor criterion to describe the quality of a match. In the example given, $\mathbf{r}_{2,k}$ would therefore be linked to $\mathbf{r}_{1,k+1}$, and $\mathbf{r}_{3,k}$ to $\mathbf{r}_{2,k+1}$, whereas $\mathbf{r}_{1,k}$ and $\mathbf{r}_{3,k+1}$ would have no correspondents in frame $k+1$ and k , respectively. This would represent a false speckle disappearance and appearance, and more critical for flow recovery, would yield the wrong selection of matches.

In the following, we propose a solution to this challenging tracking problem, using the terminology and methods of graph theory (Sedgewick, 2002). Speckles are identified with graph vertices and candidate matches with graph edges. Different time-points correspond to separate graph layers and the matching topology is defined by a sub-graph in which the edges connect corresponding speckles. We explain the computation of the “best” sub-graph first for the simple example in Fig. 3-1 (a), which can be translated into a two-layer graph. Then, we indicate the weaknesses of the two-layer approach, mainly in presence of anti-parallel speckle movements, and outline the extension of the method to a three-layer graph.

3.3.6 Tracking with two-layer graphs

The relation between speckles (circles for frame k , squares for frame $k+1$) and candidate matches (arrows), and their representation as graph vertices and graph edges, respectively, are illustrated in Fig. 3-1 (a) and 3-1 (b). The speckles $\mathbf{r}_{2,k}$ and $\mathbf{r}_{3,k}$ have two candidate matches within their search areas (defined by the dashed circles with radius d). Thus, in the corresponding graph (Fig. 3-1 (b)) two edges start from each of these positions. For $\mathbf{r}_{1,k}$ only one vertex in frame $k+1$ falls into the search area and accordingly, only one edge leaves the corresponding vertex in layer k . Notice that the limitation of candidate matches to a certain search area reduces the graph complexity and thus, the computation time. This is critical when running the procedure on thousands of speckles. As long as the areas enclose the maximum expected displacement of a speckle, this restriction has no effect on the final solution. Each graph edge is attributed an integer capacity which represents the maximum flow that can be transferred across a single edge (the use of the term *flow* in graph theory is unrelated to the cytoskeletal flow we aim at recovering with the tracking). In our graphs, each edge has a capacity 1 (cf. first italic number assigned to each edge of the graph in Fig. 3-1 (b)). Graph edges are also attributed a cost, reflecting the likelihood of the candidate match. In the example of Fig. 3-1 we simply assign the vector length of the match, rounded to an integer

value, as a cost to the edge (cf. regular numbers assigned to each edge of the graph in Fig. 3-1 (b)).

According to graph theory, optimal matches with no topological conflicts are obtained by maximizing the flow crossing the graph, while minimizing the overall cost. The latter is calculated as the sum of the cost of all edges multiplied by the flow crossing them. Algorithms to achieve this are available either commercially or in the public domain (Goldberg, 1997; Sedgewick, 2002). In Fig. 3-1 (a), the requirement of maximum flow forces the solution to the correct topology. The overall cost of the solution amounts to $10+11+8=29$. Although there are many other sub-graphs with lower cost, including the nearest neighbor match, associated with a cost of $5+4=9$, none of them sustains the maximum flow of 3. The requirement of minimal cost *and* maximum flow yields an optimal solution to the assignment problem.

For any particle tracker, the appearance and disappearance of particles represent major sources of perturbation for the reliable recovery of particle motion. This is how this problem is addressed in the presented scheme: the optimal sub-graph is selected in a two-step procedure. First, a so-called *network flow algorithm* is run, followed by a so-called *mincost algorithm*. The outcome of the network flow algorithm is a configuration of edges, each one assigned an effective flow value (cf. bold-italic number in Fig. 3-1 (b)). In our case the effective flow values are either 0 or 1. In terms of graph theory this means that edges are either empty (0) or full (1). Full edges now define the topology of a sub-graph that maximizes the flow across the entire graph. They connect a source speckle in frame k with a target speckle in frame $k+1$, whereas empty edges represent candidate matches discarded by the network flow algorithm because of a violation of the topological constraints. Importantly, not more than one unit of flow can leave from any of the vertices in layer k , or flow into a target vertex in layer $k+1$.

The search for maximum flow is ambiguous. The larger the graph the more sub-graphs exist which can sustain the maximum flow. Which of those is associated with the best matches is determined by the mincost algorithm. It uses the output graph of the network flow algorithm as an initial solution and seeks other sub-graphs with the same flow but lower overall cost. The final sub-graph returned by the mincost algorithm again labels the selected speckle matches with an effective flow 1, the others with an effective cost 0. Notice that the sub-graph may or may not be equal to the initial one obtained by the maxflow algorithm. In the example of Fig. 3-1 (b), there is obviously no reassignment of edge flows, as there is only one solution supporting the maximum flow of 3.

Given the output of the combined maxflow and mincost algorithms, speckle appearances and disappearances are readily found. Disappearing speckles correspond to vertices in layer k for which no edge leaves with an effective flow 1. Speckle appearances correspond to vertices in layer $k+1$ for which no edge arrives with an effective flow 1. These considerations will become central in the future when we make a detailed speckle lifetime analysis, but they are not critical here. For the scope of this paper it is sufficient that the matches used for flow recovery are minimally perturbed by speckle appearances and disappearances.

3.3.7 Tracking with three-layer graphs

In the case of speckles moving in anti-parallel flows, the recovery of correct matches is particularly difficult. Fig. 3-2 (a) displays the result of a two-layer graph algorithm run on data comprising two interleaved, rotating flow fields with opposite directions of rotation. The match selection frequently fails in areas with proximate anti-parallel trajectories. To enhance the tracking performance we modified our graph to be able to exploit the information contained in three frames simultaneously. This allowed us to exploit the notion of trajectory smoothness. Such heuristics have proven very powerful for solving the motion correspondence problem in other contexts (Veenman *et al.*, 2001). Following (Sethi and Jain, 1987) we express the cost of a candidate match as

$$c = \gamma_1 \left[1 - \frac{(\mathbf{r}_k - \mathbf{r}_{k-1}) \cdot (\mathbf{r}_{k+1} - \mathbf{r}_k)}{\|\mathbf{r}_k - \mathbf{r}_{k-1}\| \times \|\mathbf{r}_{k+1} - \mathbf{r}_k\|} \right] + \gamma_2 \left[1 - 2 \frac{\sqrt{\|\mathbf{r}_k - \mathbf{r}_{k-1}\| \times \|\mathbf{r}_{k+1} - \mathbf{r}_k\|}}{\|\mathbf{r}_k - \mathbf{r}_{k-1}\| + \|\mathbf{r}_{k+1} - \mathbf{r}_k\|} \right]. \quad (3.1)$$

The first term is equal to zero for displacement vectors that are aligned, while the second term is zero for displacement vectors whose magnitude does not change over time. The sum of the two terms is therefore a measure of trajectory smoothness over three frames. The weights γ_1 and γ_2 tune the relative contribution of changes in direction versus changes in magnitude. While (Sethi and Jain, 1987) proposed $\gamma_1 = 0.1$ and $\gamma_2 = 0.9$, we found that for our application weight factors of 0.4 and 0.6 yielded better results.

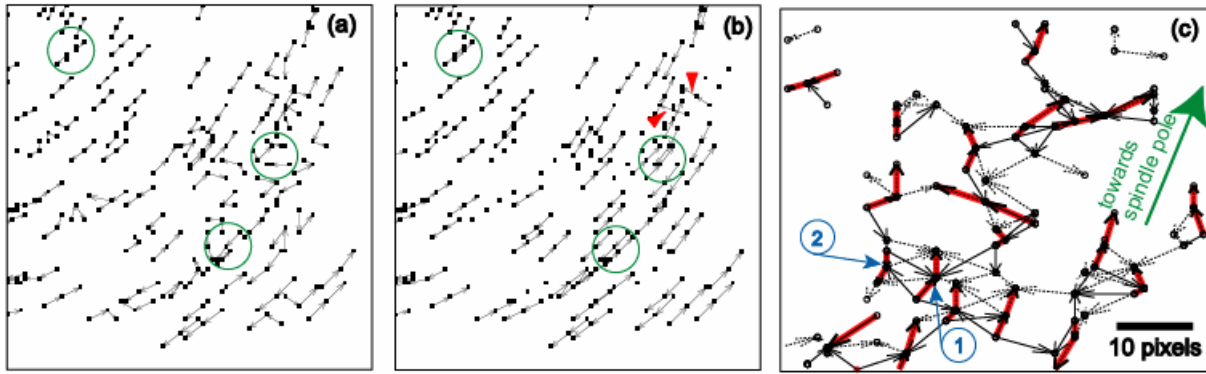


Figure 3-2

Tracking anti-parallel flow. (a) Difficulties encountered with tracking anti-parallel flow using a two-layer graph. (b) Improvement of the performance using a three-layer graph, which can account for the smoothness of speckle trajectories. See text for a discussion of the highlighted areas. (c) Illustration of the selection process in real data exhibiting anti-parallel flow (FSM data of bi-polar microtubule flux in a mitotic spindle; Fig. 3-6). Solid black vectors are candidate matches between frame k and frame $k+1$, dotted black vectors are those between frame $k+1$ and frame $k+2$. The algorithm associates solid vectors with dotted vectors to form trajectories linking speckle positions at time k , $k+1$ and $k+2$, such that the overall cost of the selected paths is minimal. According to the cost function in Eq. (3.1) the algorithm tends to select smooth trajectories with minimal speckle intensity variation. The red vectors indicate the matches selected by the algorithm. In agreement with the bipolar flux arrays, they outline a densely interleaved anti-parallel flow (see for example the trajectories indicated by labels 1 and 2, pointing towards the upper and lower spindle poles, respectively).

With the cost function of Eq. (3.1) we do not only introduce a third graph layer, but the costs of the edges between the layers k and $k+1$ are now coupled to those of the edges between the layers $k-1$ and k . This requires a non-standard re-structuring of the graph, which will be discussed in a more dedicated publication. Here we confine ourselves to demonstrating the improvement in tracking performance.

Fig. 3-2 (b) shows the same flow field as Fig. 3-2 (a) but now tracked with a three-layer graph. With the exception of two false matches (red arrowheads) the algorithm returns the correct solutions. We highlight three locations (green circles) where anti-parallel trajectories are particularly close. As evident in Fig. 3-2 (b), the algorithm cannot guarantee the selection of all matches. This will have to be improved for complete lifetime analysis but is irrelevant for the flow evaluation aimed at in this contribution. As explained in the sections on Flow recovery and Results, missing matches do not affect the reconstruction of flow fields.

Nevertheless, to maximize the number of matches and to make the selection as robust as possible, the cost function should incorporate as much prior knowledge of the speckle action between consecutive frames as available. A further information we have is that

speckles largely conserve their intensity. Therefore, we seek matches with minimal variation in speckle intensity. To achieve this, the term $0.2 * \left[\frac{\sigma_X(I)}{\bar{I}} \right]$ was added to the cost c in Eq. (3.1), where $\sigma_X(I)$ is the standard deviation of the intensities of the speckles at $\mathbf{r}_{k-1}, \mathbf{r}_k$, and \mathbf{r}_{k+1} , and \bar{I} is the mean intensity over all three frames:

$$c = 0.4 \left[1 - \frac{(\mathbf{r}_k - \mathbf{r}_{k-1}) \cdot (\mathbf{r}_{k+1} - \mathbf{r}_k)}{\|\mathbf{r}_k - \mathbf{r}_{k-1}\| \times \|\mathbf{r}_{k+1} - \mathbf{r}_k\|} \right] + 0.6 \left[1 - 2 \frac{\sqrt{\|\mathbf{r}_k - \mathbf{r}_{k-1}\| \times \|\mathbf{r}_{k+1} - \mathbf{r}_k\|}}{\|\mathbf{r}_k - \mathbf{r}_{k-1}\| + \|\mathbf{r}_{k+1} - \mathbf{r}_k\|} \right] + 0.2 \left[\frac{\sigma_X(I)}{\bar{I}} \right].$$

Fig. 3-2C shows an example of the graph selection process on real data. We present a zoom-up of a small region near one pole of the mitotic spindle, analyzed in more detail in the Results section (see frame of inset (b-I) in Fig. 3-6 (b)). Here, speckles mark an interspersed scaffold of microtubules, which flow in opposite directions. The panel displays candidate matches shorter than the radius ($d = 10$ pixels) of the circular search region centered at each of the speckles of frame k . Candidates between the frames $k-1$ and k are shown as solid black vectors; those between k and $k+1$ as dotted black vectors. According to the explanations above, the goal of the graph selection algorithm is to optimally pair solid vectors with dotted vectors. The possible combinations of vectors are bewildering, even for the very small example shown. The red vectors indicate the selected matches. As the region under scrutiny is near the upper spindle pole, the majority of matches points in the direction of the pole, located above and to the right of the zoom-in window (see green arrow). Most of the remaining matches point in the opposite direction indicating that these speckles belong to long microtubules reaching into this area from the opposite pole. We will revisit this phenomenon in the Results section with more emphasis on the biological significance. For now, we remark that e.g. the two anti-parallel vector pairs, highlighted by the blue labels 1 and 2, are only 6 pixels apart, which is in the range of the actual speckle displacements. A global resolution of topological conflicts, as it is achieved with the proposed selection of matches using graphs, is essential to cope with such a densely interleaved anti-parallel flow.

3.3.8 Relaxing the condition of non-fusing and non-splitting speckles in a next version of the tracking scheme

Despite our finding that fusion and splitting are relatively rare, we aim at overcoming this limitation of the current scheme (see above) with a future version. Fusion and splitting of

speckles can be addressed in two ways: i) by relaxing conditions a) and b), which demands a restructuring of the graph such that multiple edges with an effective flow equal 1 can leave a vertex in layer k , and vertices in layer $k+1$ can receive several edges with an effective flow equal 1. For graphs with thousands of vertices per layer this procedure will be ambiguous and computationally not affordable; ii) by resolving signal overlaps during particle generation. This bears the advantage that the graph structure is unaffected and all the core modules of the current software package are applicable without modifications. Near co-location of two or more significant speckles can e.g. be resolved by mixture model fitting (Thomann *et al.*, 2002). As a result, several speckle positions and intensities are obtained for what is currently detected as only one local maximum. This procedure will also be computationally expensive, but in contrast to the restructuring of the graph, it can be implemented in a framework for parallel computing.

3.3.9 Flow recovery by filtering and interpolation

As mentioned in the Introduction, the first utilization of the extracted matches consists in the reconstruction of speckle flow. Because speckle intensities and positions are stochastic variables subjected, among other effects, to the influence of thermal fluctuations (Chapter 2), their displacements are only in a statistical sense related to the underlying average cytoskeletal flow. Flow recovery is therefore achieved by spatial filtering of the map of matches delivered by the graph algorithm, using convolution. At the same time, we obtain interpolated flow on a regular grid, which mainly serves the purpose of flow visualization. In addition to spatial filtering, steady-state flow components are retrieved by filtering the maps of matches in time.

The amount of filtering is determined by the spatial and temporal correlation lengths of the filter. In our case, we chose an isotropic Gaussian convolution kernel in space, multiplied with another Gaussian in the time domain, describing the correlation of flow between any two frames of the movie. In the current version of the software the correlation lengths are set globally, i.e. the same lengths are applied throughout the entire field of view for all frames. They are tuned by the operator based on an educated guess. Obviously, the parameter choice depends on the focus of the study, and thus on some prior knowledge of the flow structure. For example, if an average, global measure of cytoskeletal motion is to be obtained, the spatial and temporal correlation lengths ought to be set relatively large, e.g. in the range of the persistence length of the studied polymer assembly ($\sim 2 - 7 \mu\text{m}$ for actin meshworks) (Tseng and Wirtz, 2001). On the other hand, if flow needs to be studied around a

pole in the vector field, e.g. associated with an area of meshwork contraction or depolymerization, the correlation length has to be lowered to pick up the details. This is of course done at the risk of including more random components, which are unrelated to the meshwork flow into the pole.

In future versions of the software we will relax the need for operator input. Prior knowledge of the flow structure can for example be extracted from the flow field itself. Borrowing ideas from edge preserving filtering in computer vision, a filtering framework will be implemented where the correlation lengths are iteratively adjusted to the local convergence or divergence of flow. This will permit the combined recovery of global flow in areas of coherent speckle movement and of details of poleward or shear flow in areas with singularities in the movement field. Alternatively, the computation of correlation lengths can be supported with a mechanical model of the cytoskeleton. Initial tests with such approaches deliver promising results. However, their discussion goes beyond the scope of this paper and we confine the presentation of results to flow fields computed with one globally and manually defined set of correlation lengths.

An application where global filtering is inappropriate arises with the densely interleaved anti-parallel tubulin flow present in the mitotic spindle. Here, global filtering would result in vectors of zero length approximately everywhere. In this case, the algorithm starts with a sorting procedure before filtering, where matches pointing towards one pole are separated from those pointing to the opposite pole. This operation is straightforward and robustly performed without further user-interaction (see Results and Fig. 3-6 (b)).

3.4 Results and Discussion

The scope of this section is to demonstrate the potential of our new single speckle tracker to extract flow information in different situations. We present three types of data: i.) simulated flow fields where artificial particles are tracked and the recovered matches are compared with the known displacement vectors; ii) the speckle flow at the front edge of a migrating cell is analyzed, to indicate the power of computational FSM to unravel the dynamics of lamellipodial and lamellar F-actin meshworks. Intentionally, we perform our study on FSM data already published and manually analyzed in order to point out the gain of high-content information achieved with our new computational schemes; iii) speckle flow representing interleaved microtubule flux in mitotic spindles is analyzed to emphasize the ability of our tracker to cope with anti-parallel movement. In addition, the spindle data is attractive to demonstrate the new possibilities we obtain with the wealth of quantitative

information we can now extract. We present two statistical population analyses of single speckle matches which provide novel insights of the microtubule organization and dynamic behavior inside the spindle.

3.4.1 Performance analysis on simulated flow fields

Data of the type “peas in a rotating dish” are traditionally used for testing tracking approaches and we have adhered to this practice here. For such data, the magnitude of the displacement depends heavily on the position, a feature shared with data from biological samples. We have generated at time point k a spatially random planar distribution of particles with random intensities. In the following, we always mean “obeying a uniform distribution” when we say “random”. Then, these particles were twice subjected to a rotation of three degrees to generate the particles at time point $k+1$ and at time point $k+2$. The particle sets were distributed over an area of 200×200 pixels and the first frame contained approximately 200 particles. From one frame to the next, random variations with a maximum of 0.5 times the intensity of the corresponding particle in the previous frame were imposed. These variations are significantly above those we could observe for real data and therefore constitute a demanding benchmark for the tracker. The parameters mentioned above were applied to all simulations, except when explicitly stated otherwise.

The quality of tracking was measured as the proportion between false matches and the number of recovered matches. As a rule of thumb, error rates below 20% do not seriously affect flow recovery and thus are acceptable. The average density of speckles in real FSM images generally guarantees 5 matches or more falling into the support area of the convolution kernel applied for flow filtering and interpolation. Consequently, with an error rate of 20% one out of five matches would deteriorate the convolution as an outlier. Since the correspondence search area is limited to the user-defined radius d , the magnitudes of outlier matches are also limited. In a strict mathematical sense this moves the break-point of the convolution to infinity (Rousseeuw and Leroy, 1987). In practical terms, this means that, in the worst case, filtered and interpolated flow vectors near outlier matches are biased by $d/5$.

In the same spirit, missing matches do not need to be counted as errors as they do not contribute to the recovery of filtered flow. Unless stated otherwise, the number of matches recovered was above 90 % for all of the following tests on synthetic data.

3.4.1.1 Influence of positional fluctuations

In real data, speckle trajectories are perturbed by various effects, including thermal fluctuations, local cytoskeleton contractions, and positional fluctuations due to photometric changes (see Chapter 2 for a discussion of these effects). Hence, we have evaluated the influence of positional fluctuations by subjecting the speckles in every frame to random perturbation displacements of variable mean. The proportion of mistakes committed by the matching algorithm changed from $1.8 \pm 0.75 \%$ to $5.3 \pm 1.6 \%$ ($n=3$), when progressively increasing the maximum perturbation displacement from 0 to 3 pixels imposed independently on both image directions.

3.4.1.2 Influence of particle appearance and disappearance

We have also evaluated the influence of speckle appearance and disappearance, which in real FSM data is associated with polymer turnover (Chapter 2). We ran separate tests for appearance and disappearance. To mimic appearance, new particles with random intensities were added to the particle sets in time point $k+1$ and $k+2$ at random positions. The rate of appearance is expressed as the number ratio between new particles and existing particles in the previous time point. To mimic disappearance, a certain fraction of existing particles were randomly deleted from the sets in time point $k+1$ and $k+2$. The rate of disappearance is expressed as the number of particles removed, divided by the number of particles present before their elimination in the next frame.

The proportion of mistakes committed by the algorithm when varying the appearance rate from 0 % to 80 % increased progressively from $1.8 \pm 0.75 \%$ to $11.5 \pm 2.7 \%$ ($n=3$), the one associated with disappearance rates between 0 % to 60 % from $1.8 \pm 0.75 \%$ to $2.5 \pm 0.5 \%$ ($n=3$). These results indicate that the tracker performs robustly in the presence of this type of perturbation.

3.4.1.3 Influence of the magnitude of the displacement

To examine the performance of the tracker as a function of the mean displacement, we varied the rotation angle from 0 to 7 degrees. The results clearly depend on the density of particles, so the latter was kept constant. In these simulations, the search distance d for candidate matches (see paragraph Algorithm - Generation of candidate matches) was set to the maximum displacement across the images. The proportion of mistakes committed by the algorithm when going from 0 to 7 degrees increased progressively from $1.8 \pm 0.75 \%$ to $9.7 \pm 3.7 \%$ ($n=3$).

3.4.1.4 Influence of anti-parallel flow

Anti-parallel flow is a distinctive characteristic of the mitotic spindle or of contracting actin/myosin assemblies. Hence, we tested our algorithm on a data set where two sets of particles were rotating in opposite directions. This was done by superposing two sets of data of the type used up to this point, where rotations were taking place in opposite directions (the total number of particles in each frame was approximately 400). The results are shown in Fig. 3-3A, and indicate that the tracker is not confused excessively with shear flow. The figure inset points at one of three particle clusters, where errors occur in the selection of matches.

Fig. 3-3 (a) shows the recovery without perturbation from displacement fluctuations, particle appearance or disappearance. We have also tested the influence of these parameters in the presence of shear flow (results not shown). To our surprise, the results were similar to those presented before with only parallel flow.

3.4.1.5 Influence of various effects applied simultaneously

Ultimately, a speckle tracker has to deal with multiple sources of perturbation simultaneously. To conclude these simulations, we show one example of flow estimation where the effects of speckle appearance, speckle disappearance, speckle intensity variation and positional fluctuations are simultaneously present (Fig. 3-3 (b)). As can be recognized in Fig. 3-3 (b), the global flow is recovered accurately. Moreover, the average rotation angle estimated from the recovered flow was equal to $2.5^\circ \pm 0.3^\circ$, underestimating the nominal value of 3° only slightly.

3.4.1.6 Comparative evaluation

The goal of the present paper is not to systematically compare our approach with other tracking algorithms, but to apply it to solve important biological problems. However, for a very partial, comparative evaluation of our software, we have tested it on a data set accepted as a benchmark in the computer vision community (Veenman *et al.*, 2001). The centroid coordinates of these particles were provided with the data set, and no other information than that was exploited to recover the trajectories. We have tracked the particles between the first three frames of the sequence, as shown in Fig. 3-3 (c).

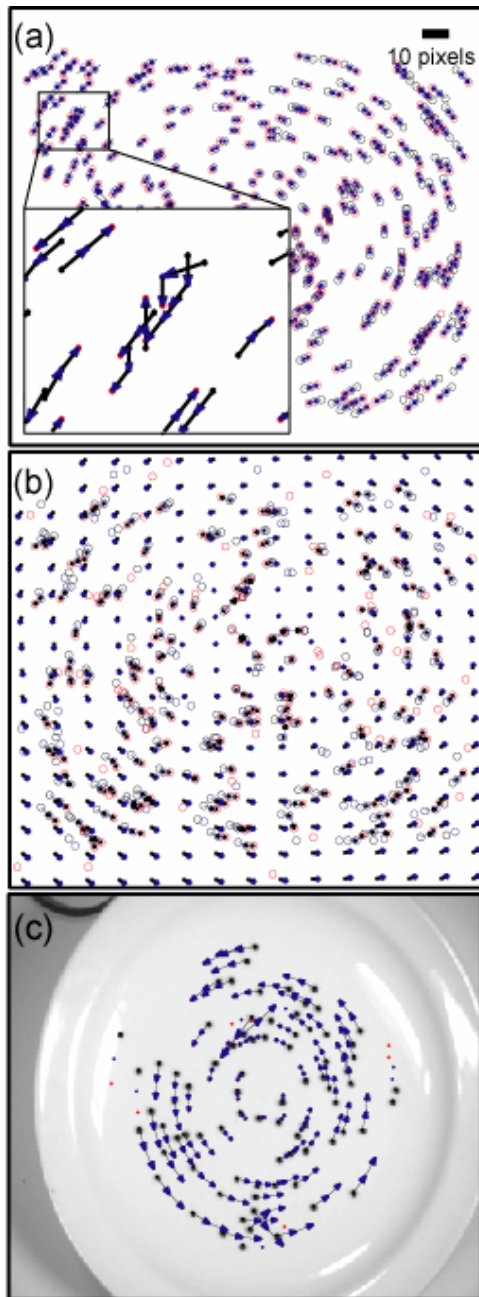


Figure 3-3

Performance tests of the algorithm using synthetic data sets. (a) Tracking of two interleaved and anti-parallel flow fields of ~ 200 particles each, rotating at an angular velocity of 3° per frame. Particles belonging to the first, second, and third frame are represented by black, blue and red circles, respectively. The recovered matches are indicated by arrows connecting the particles. The inset shows a region containing matching mistakes. Speckle intensity variations are also used for selecting the trajectories, sometimes leading to inappropriate matches. In the case of a rotating field, the true trajectory is not the smoothest of all possible, which is another source of mistakes. (b) Tracking a rotating flow field when multiple perturbations are applied. The rate of appearance between successive frames was 10% of the number of existing particles, while 10 % of existing particles were deleted between each pair of frames. The amplitude of random positional fluctuations in each frame was 2 pixels in both the horizontal and the vertical image direction. The width of the filter kernel was set to 20 pixels (cf. text for further parameters). Continuous thin arrows represent the recovered matches, while thick arrows represent the filtered vector field. The average recovered rotation angle was $2.5^\circ \pm 0.3^\circ$, only slightly underestimating the nominal rotation angle of 3° . (c) Tracking a standard test data set for particle tracking methods (Veenman *et al.*, 2001). The few mismatches correspond to trajectories, which are smoother than the correct ones (i.e. linked points are in almost perfect alignment). No intensity information was available for this data set.

While there are algorithms reported to be able to track this data without a single mistake, most of them experience difficulties with it (Veenman *et al.*, 2001). Moreover, our algorithm can handle data sets containing thousands of particles, whereas the rather complete panel of algorithms tested by (Veenman *et al.*, 2001) tends to fail for more than 100 particles. Finally, except for the fact that we have adjusted the parameter d (see paragraph Algorithm - Generation of candidate matches), we have used our algorithm without tuning it for this particular data set. In conclusion, our algorithm seems unique in being able to match thousands of particles, and performs well compared to other trackers on smaller problems.

3.4.2 F-actin flow recovery in a migrating newt lung epithelial cell

A cross-linked meshwork of F-actin continuously polymerizes in a highly regulated manner at the edge of migrating cells (Pollard *et al.*, 2000). Polymerization is thought to generate protrusive forces that push forth a lamellipodium and begin the cell motility cycle (Mogilner and Oster, 1996). Often, the growth of the polymerizing meshwork is compensated by myosin-driven rearward pulling of the meshwork, such that the F-actin cytoskeleton exhibits a retrograde flow (Lin and Forscher, 1995). In addition to myosin motor activity, the polymerization of the meshwork itself may contribute to pushing forces against the leading edge plasma membrane, promoting F-actin transport away from the edge. Spatial perturbations of the balance between polymerization and retrograde transport produce macroscopic shape changes in the cell boundary, which ultimately lead to a forward or backward movement of the lamellipodium. To understand the mechanics of cell migration, it is therefore essential to quantify the spatial modulation of F-actin retrograde flow and to relate it to molecular factors controlling motor activity, polymer turnover, and meshwork mechanical properties (Cramer, 1997; Lauffenburger and Horwitz, 1996). The direct coupling of cell shape variations and F-actin flow was demonstrated in (Danuser and Oldenbourg, 2000), where spatial changes in a high-resolution map of retrograde flow were accompanied by deformations of the cell outline. However, for technical reasons this study was limited to a steady state analysis. In order to understand how F-actin flow contributes to cell migratory and morphogenic responses, dynamic maps of the flow are required. As will be demonstrated in the following, FSM appears to be the ideal tool for this purpose.

3.4.2.1 Recovery of complete F-actin flow maps at the front edge of a migrating cell

We have analyzed newt lung epithelial cells micro-injected with fluorescently labeled actin during their migratory wound-healing response in tissue culture. In FSM images, the actin meshwork appears in these cells as an approximately even distribution of fluorescent speckles with brighter areas representing regions of high F-actin concentration (Salmon *et al.*, 2002). The dataset we analyzed was published in Fig. 3a of (Waterman-Storer *et al.*, 2000a) and the Quicktime movie is available as Supporting Material of the present paper (actinFlow.mov). Fig. 3-4 (b) shows the filtered flow obtained by convolving matches from the first 7 frames of the FSM movie, overlaid on the first frame. In the original publication, the analysis of F-actin flow was restricted to visual inspection or kymographs, such as shown in Fig. 3-4 (a) (see also Fig. 3c of Waterman-Storer *et al.* (2000a)). With our new tool we can now recover a complete vector field representing the flow in every point of the meshwork

(Fig. 3-4 (b)). For the sake of visualization, interpolated flow vectors are plotted on a grid (raster size $1\ \mu\text{m}$). Vector lengths are proportional to the flow velocity and their direction indicates the locally averaged direction of speckle movements. Spatial filtering was performed with a correlation length of $1.6\ \mu\text{m}$ (see paragraph Algorithm – Flow filtering), chosen in consideration of the mechanical persistence length of an F-actin meshwork (Tseng and Wirtz, 2001). The overall pattern of flow in our map corresponds closely to the visual impression one gains from simply watching the movie. However, there were regions that initially did not draw our attention in the movie, such as the anterograde flow near label A, or the flow converging towards a “pole” (label P). The use of our algorithm uncovered such patterns and, upon closer visual inspection, it became apparent that in this case computer vision outperformed the human eye not only in terms of quantification and objectivity, but also in terms of sensitivity in detection. This is a rather rare situation, as computer vision algorithms typically lag behind human vision in qualitative analyses of complex scenes. We speculate that the complexity inherent to the movements of the actin cytoskeleton and associated FSM data obscures significant details to the human observer.

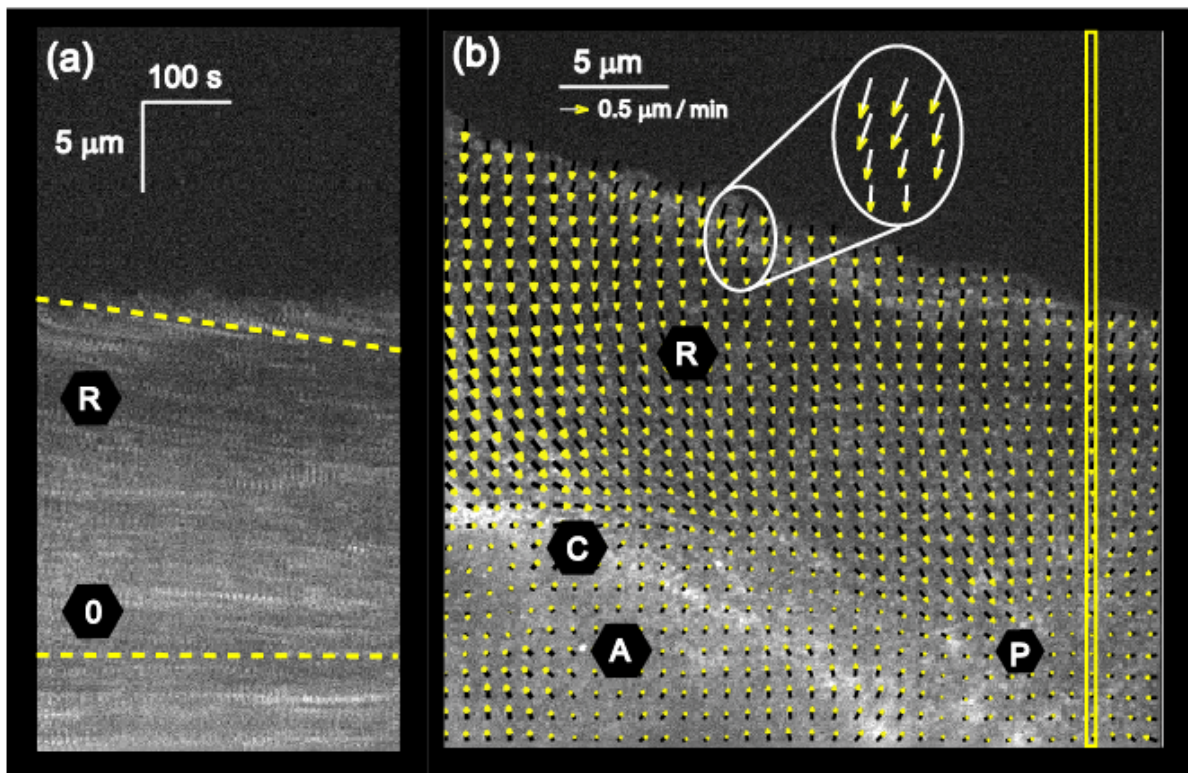


Figure 3-4

F-actin speckle flow in a migrating newt lung epithelial cell. (a) Kymograph analysis (cf. text for more details) in the region indicated by a narrow yellow box in panel B. The slopes of the streaks in the kymograph permit the measurement of the average speckle flow velocity along the vertical axis of the box, as indicated by two dashed lines highlighting streaks from two different populations of speckles. In the lamellipodium and lamellum, a retrograde flow of $0.45 \pm 0.05 \mu\text{m}/\text{min}$ is measured (label R). Further away from the leading edge the flow stops and the horizontal streaks indicate a flow of $0.0 \pm 0.05 \mu\text{m}/\text{min}$ (label 0). (b) Flow analysis of the entire cell front using the new single speckle tracker. The presented flow field is averaged over 7 frames and spatially filtered with a correlation length of $1.6 \mu\text{m}$. The flow vectors are interpolated on a grid with $1 \mu\text{m}$ side-length, and overlaid on the first frame of the movie. The flow appears to be organized in three main regions: i) retrograde flow (R); ii) converging (C) and poleward (P) flow; and iii) anterograde flow (A). Velocity vectors with an origin on the axis of the kymograph report a flow speed of $0.40 \pm 0.05 \mu\text{m}/\text{min}$ (R) with a transient slow down to $0.02 \pm 0.05 \mu\text{m}/\text{min}$, in agreement with the kymograph. Further down on this axis an anterograde flow of $0.08 \pm 0.04 \mu\text{m}/\text{min}$ is measured, which is not detectable with kymograph analysis. Flow speeds in other areas of the mapped field are higher than $0.40 \mu\text{m}/\text{min}$, e.g. at the very front (see zoom up). See text for further discussion of the flow map.

3.4.2.2 F-actin flow is organized in three distinct zones

Three distinct zones can easily be distinguished in the flow map: i) the lamellipodium and lamellum at the cell edge, where a prominent retrograde flow away from the cell edge is present (label R in Fig. 3-4 (b)); ii) further down in the direction of the cell body, a laminar convergence region, where most speckles coalesce and subsequently move parallel to the cell edge (label C in Fig. 3-4 (b)). As mentioned before, in the same zone we also find poles where speckles converge towards one point (label P in Fig. 3-4 (b)); iii) behind the convergence region, a flow of smaller magnitude is on average directed anterograde (towards the cell edge; label A in Fig. 3-4 (b)). The vector map presented here illustrates strikingly the spatial complexity of F-actin meshwork flow.

3.4.2.3 F-actin flow is dynamically modulated

By matching successive frames over time, complete movies of the flow can be constructed, revealing not only spatial but also interesting temporal modulations of F-actin flow. In Fig. 3-5, we map the temporal evolution of the vector field for a window in area C in Fig. 3-4 (b) where retrograde and anterograde flows converge. The anterograde flow is seen to turn its direction within a period as short as 40 seconds. We speculate that this could be induced by very local modulations of the myosin activity in this area. In summary, our FSM analysis technique gives us access to an entirely new body of knowledge on F-actin dynamics.

Such mapping can potentially uncover how the dynamics are affected by upstream molecular control factors, and how it correlates with downstream responses such as cell migration events. This new tool can be used to investigate and quantify F-actin dynamic responses to perturbations in actin-related signaling (Wittmann and Waterman-Storer, 2003), to drug application (Chapter 2), and to spatially modulated cell adhesion (Csucs *et al.*, 2003).

3.4.2.4 Comparison with previous kymograph analyses

The presence of the three regions, as revealed by Fig. 3-4 (b), agrees well with a comparatively sparse kymograph analysis of the flow in the same cell system (Salmon *et al.*, 2002). Although much less detailed and subject to potential artifacts, kymographs generated at a few critical locations were able to recover some of the main features of actin flow characteristics. An example of such a kymograph is given in Fig. 3-4 (a). Image slices (the position of the slice is shown by a yellow box in Fig. 3-4 (b)) of 5 pixels in width have been copied from the first 50 frames of the movie and have been pasted side by side to form the kymograph. Speckles that move along the long axis of the box for a sufficiently long period become visible as bright streaks in the kymograph. Their slope is a measure of speckle speed, as indicated by dashed lines in Fig. 3-4 (a). The speeds estimated for the lamellum and at the pole were equal to $0.45 \pm 0.05 \mu\text{m}/\text{min}$, and $0.0 \pm 0.05 \mu\text{m}/\text{min}$, respectively. In good agreement, our method delivered for the same locations and time period speeds of $0.40 \pm 0.05 \mu\text{m}/\text{min}$, and $0.02 \pm 0.05 \mu\text{m}/\text{min}$, respectively. As manifest in the kymograph of Fig. 3-4 (a) and the flow map of Fig. 3-4 (b), there is a difference in the flow speed between the lamellipodium proximal to the leading edge and the inner lamellum, suggesting that the flow in these two areas is driven by distinct molecular mechanisms (Waterman-Storer and Salmon, 1997; Waterman-Storer *et al.*, 2000a; Salmon *et al.*, 2002). Our new vector map permits the investigation of this apparent transition along the entire cell edge. In some regions we indeed find this same behavior. The lamellipodial speed (white ellipse and zoom-up in Fig. 3-4 (b)) can be up to two times faster than the fastest rates in the lamellum (around R label in Fig. 3-4 (b)). In other regions the difference is not as clear, indicating that there is substantial variation of flow velocity along the edge. However, at this point we are cautious not to draw too far reaching conclusions. Because the lamellipodium is very narrow in these cells, i.e. in many locations less than the support area of the convolution kernel, and naturally fluctuates in width beyond the lamellum (Waterman-Storer and Salmon, 1997), our flow filtering probably obscures some details of the velocity variations along the edge and in the transition zone between lamellipodium and lamellum. Here, adaptive adjustment of the correlation lengths

according to the underlying flow structure will likely reveal further insights. There is evidence that the retrograde actin flow in the lamellipodium is driven solely by forces associated with actin polymerization pushing on the leading edge plasma membrane, while actin flow in the lamellum is myosin dependent (Waterman-Storer and Salmon, 1997). Thus, a more precise spatial mapping of the velocity vectors with less filtering may uncover where exactly in the lamellipodium/lamellum junction myosin motors begin to engage actin filaments, a piece of information that can not be obtained by any other means.

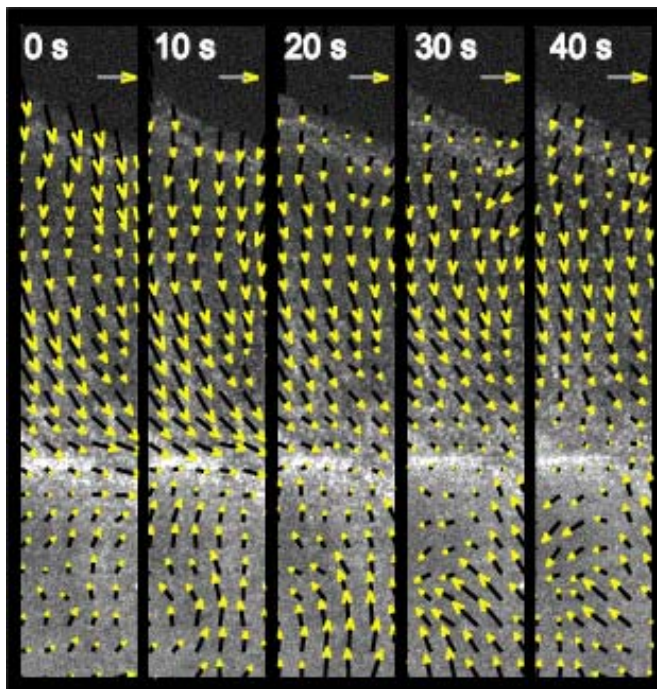


Figure 3-5

Dynamic changes in the actin cytoskeleton flow in the area C of Fig. 3-4 (b), where we suspect increased myosin concentration and activity (cf. text for more details). Dynamic maps are obtained by filtering the matches of every frame separately in the spatial domain only. The vector fields are then concatenated into movies with the same temporal resolution as the raw data.

3.4.3 Recovery of microtubule flux in a mitotic spindle

We have applied our single speckle tracker to an FSM movie of microtubules in metaphase spindles with replicated mitotic chromosomes assembled in meiotic *Xenopus* egg extracts as described in (Desai *et al.*, 1998; Murray *et al.*, 1996; Waterman-Storer *et al.*, 1998). Previous studies using fluorescence photoactivation (Desai *et al.*, 1998; Sawin and Mitchison, 1994) or fluorescent speckles to mark the microtubule lattice have reported poleward flux rates of 2.0 to 2.5 $\mu\text{m}/\text{min}$. Measurements by fluorescence photoactivation are of low resolution and yield only averages over the whole spindle. Previous FSM measurements were done by kymograph analysis along the spindle axis and represent only a narrow sample of speckle movements within the spindle. In contrast, our particle tracking

algorithm provides detailed velocity information throughout an optical section of the spindle as shown in Fig. 3-6. Panel 3-6 (a) displays a cartoon of the microtubule organization in a metaphase mitotic spindle, which is formed from microtubules extending from opposite spindle poles (SPs) with plus ends distal and minus ends proximal to the associated pole. Kinetochore microtubule bundles link sister chromosomes to the poles (population 1). Most spindle microtubules are non-kinetochore microtubules and interpolar spindle fibers are formed from bundles of overlapping non-kinetochore microtubules extending from opposite poles (population 2). The links between overlapping microtubules from opposite poles include microtubule associated motors (Sharp *et al.*, 2000), rendering the spindle a complex motile scaffold (Wittmann *et al.*, 2001b). Also indicated is the position of the metaphase plate (MP) where chromosome pairs align under balanced bipolar forces, before they start to segregate after inactivation of the mitotic checkpoint (see Introduction).

3.4.3.1 Single speckle tracking reveals bi-polar flux

In the metaphase arrangement, poleward microtubule flux coupled to minus end depolymerization produces a bi-polar flow pattern with anti-parallel components. When observed by FSM, this gives rise to a complicated speckle trajectory field with opposing velocity vectors (see Quicktime movie spindleFlow.mov in Supporting Material). Indeed, the speckle flow recovered from the present FSM data is clearly bipolar. Fig. 3-6 (b) shows the speckle matches found by the tracker for ten consecutive frames. For visual clarity the figure contains two speckle populations, as automatically sorted by the flow filtering algorithm (see Algorithm – Flow recovery by filtering and interpolation). Speckle matches in blue point towards the upper pole, those in red point towards the lower pole (see also cartoon in panel A). The single speckle vector map clearly indicates the ability of the tracker to reconstruct anti-parallel movements, which is imperative in this case. This is confirmed in more detail by the zoom-ups of insets (b-I) and (b-II). Although this paper does not exploit speckle matches for lifetime analysis, the data presentation draws one's attention to a phenomenon related to the lifetime: the lengths of connected speckle matches increase, the closer the speckles are located to their "home pole". This finding can easily be understood by examination of the cartoon in Fig. 3-6 (a). Non-kinetochore microtubules undergo dynamic instability where their plus ends rapidly switch between phases of growth and shrinkage. Therefore, speckles generated by fluorophore incorporation during growth will disappear again when the microtubule end reaches their position during shrinkage. The more distant speckles are from the microtubule plus end, the lower is the probability of disappearing by disassembly, as

reflected by the more stable trajectories towards the pole. The short trajectories of front speckles (see red trajectories in (b-I), respectively blue trajectories in (b-II)) of 2 – 3 frames suggest rates of catastrophe (switch from growth to shrinkage) and rescue (switch from shrinkage to growth) in the range of 20 – 30 s, as expected for the dynamic instability of these microtubules (Sawin and Mitchison, 1991). The tendency for prolonged speckle trajectories towards the “home pole” is further amplified by the kinetochore microtubules, which only reach the MP, and in vertebrates are more stable than the non-kinetochore microtubules that have free plus ends (Zhai *et al.*, 1995).

3.4.3.2 The velocity of microtubule flux is constant along the mitotic axis

Fig. 3-6 (c) visualizes the filtered and grid-interpolated flow ($1 \mu\text{m}^2$ raster) of the blue speckle population in Fig. 3-6 (b). The vectors were filtered over 4 frames and with a convolution kernel with a width of $0.9 \mu\text{m}$. The vector data are overlaid on the first image of the movie. As indicated by the vector map, the flow speed is almost constant along the pole-to-pole axis, with an average equal to $2.5 \pm 0.2 \mu\text{m}/\text{min}$. This value agrees well with previous measurements in kymographs (Mitchison and Salmon, 2001; Waterman-Storer *et al.*, 1998).

At the single speckle level some tracks do not head towards the poles but have a variable lateral component, or can even transiently reverse their direction (data not shown). Most of these events do not constitute matching mistakes, as verified by manual tracking of some of the implicated speckles. They only confirm that the spindle is a dynamic structure subjected to forces of multiple origins, including thermal bending fluctuations of microtubules. Analyzing the statistical properties of the speckle micro-movement should allow us in the future to recover information about the nature of the forces acting at this scale.

3.4.3.3 Histograms of the speckle number density along the mitotic axis reveal the microtubule organization and the spatial extension of the spindle poles

Visual observation of FSM movies cannot provide quantitative answers to questions like: what is the density of microtubules, as measured by the density of speckles moving towards one pole or towards the opposite pole, as a function of the distance along the mitotic axis? In Fig. 3-6 (d), the blue line indicates the distribution of speckles moving upwards, while the red line shows the distribution of those moving in the opposite direction. Note from Fig. 3-6 (a) that the flux direction is a signature identifying which microtubule sub-system a specific speckle belongs to. Therefore, Fig. 3-6 (d) also displays the distribution of distances reached by microtubule plus ends emanating from one pole towards the other pole.

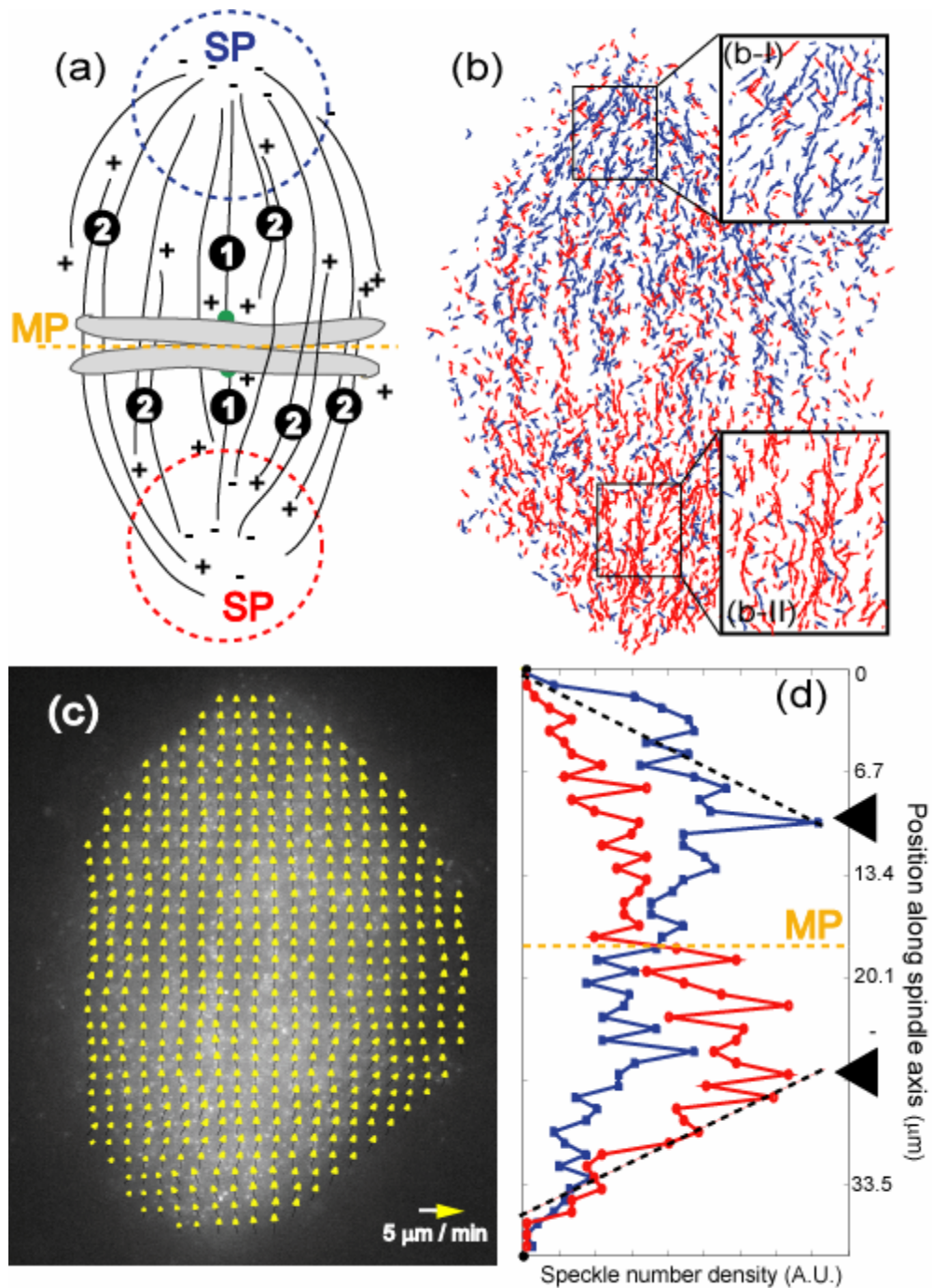


Figure 3-6

Tracking microtubule speckles in the mitotic spindle from *Xenopus leavis* egg extracts. (a) Schematic diagram of the microtubule organization in a metaphase spindle. Microtubules radiate from the two spindle poles (SPs). At metaphase, kinetochore microtubules establish bipolar attachment of the chromosomes via kinetochores (green dots; label 1), located in the metaphase plate (MP). Non-kinetochore fibers (label 2) are formed from bundles of overlapping microtubules extending from opposite poles and cross-linked by motors and other microtubule associated proteins. For a microtubule system emanating from one SP, all speckles flow poleward. Thus, in the bipolar system, the speckle flow direction is a signature of which subsystem the associated microtubule belongs to. (b) Speckle matches as recovered by the tracker aggregated over 10 frames. The populations moving upwards (blue) and downwards (red) are separated automatically before further filtering (see (c)). The number of matches

and the trajectory lengths are seen to increase as speckles approach their home pole. Both effects are discussed in more detail in the text. (c) An FSM image of metaphase spindle, overlaid by the filtered vector map of upward microtubule flux (blue matches in B; side-length of interpolation grid: 1 μm). The width of the Gaussian convolution kernel was 15 pixels (0.9 μm in the object domain). Time averaging was performed over 4 frames. The flow speed is almost constant across the whole spindle and amounts to $2.5 \pm 0.2 \mu\text{m}/\text{min}$. (d) Number density of speckles moving towards the upper SP (blue) and towards the lower SP (red) as a function of the position along the mitotic axis. See text for a further interpretation of this data.

At metaphase, kinetochore microtubules radiating from one pole reach only to the midzone, where they attach to chromosomes, while non-kinetochore microtubules can extend further towards the other pole. Consequently, one would expect for one microtubule sub-system that the density of microtubules suddenly decreases when going from one pole towards the other pole. In fact, this is what our measurements indicate and the most significant decrease occurs, as expected, at the position of the metaphase plate (Fig. 3-6 (d)). The symmetry of decrease in the two sub-systems suggests that bipolar attachment of chromosomes by their sister kinetochores to microtubules from opposite spindle poles must be complete in the present image data. In agreement with our expectation that only few non-kinetochore microtubules reach the opposite pole, the distributions progressively decrease beyond the MP.

A second remarkable conclusion that can be drawn from this distribution is the outreach of the pole region. After a peak in the speckle number approximately 10 μm away from the MP (arrow heads), the number of speckles drops, on average, monotonically towards the poles (see dashed lines). This suggests that the distribution of minus ends where microtubules depolymerize and thus, the pole itself, extends over a large area.

3.4.3.4 Flux in non-kinetochore microtubules is higher than in kinetochore microtubules

Based on histograms constructed from the set of all speckle displacements we have attempted to distinguish between two microtubule populations with putatively different flux behavior (Fig. 3-7). It could be expected that speckle velocities are higher for non-kinetochore microtubules as compared to kinetochore microtubules because the latter are linked to chromosomes, thereby introducing mechanical tension opposing the flux direction. To test this hypothesis, we considered the speckle population moving towards the upper spindle pole (represented by blue matches in Fig. 3-6 (b)). We then reasoned that, within this population, speckles starting their trajectory below the MP ought to belong to non-kinetochore microtubules. In contrast, both kinetochore and non-kinetochore microtubules are present

between the MP and the pole. If kinetochore microtubules flowed more slowly than non-kinetochore microtubules, we would expect the two histograms of the speckle speed for these halves be shifted relative to one another. Indeed, a Kolmogoroff-Smirnov test, performed on ~20,000 speckle matches over 25 frames of the movie, showed that non-kinetochore microtubules flow faster (2.57 $\mu\text{m}/\text{min}$ on average) than the mixed population (2.46 $\mu\text{m}/\text{min}$) of non-kinetochore and kinetochore microtubules (p-value: 0.0004).

We have repeated the analysis for speckles moving towards the lower spindle pole (represented by red matches in Fig. 3-6 (b)) and have obtained almost identical values: non-kinetochore microtubules flow at 2.64 $\mu\text{m}/\text{min}$ versus 2.5 $\mu\text{m}/\text{min}$ for the mixed population.

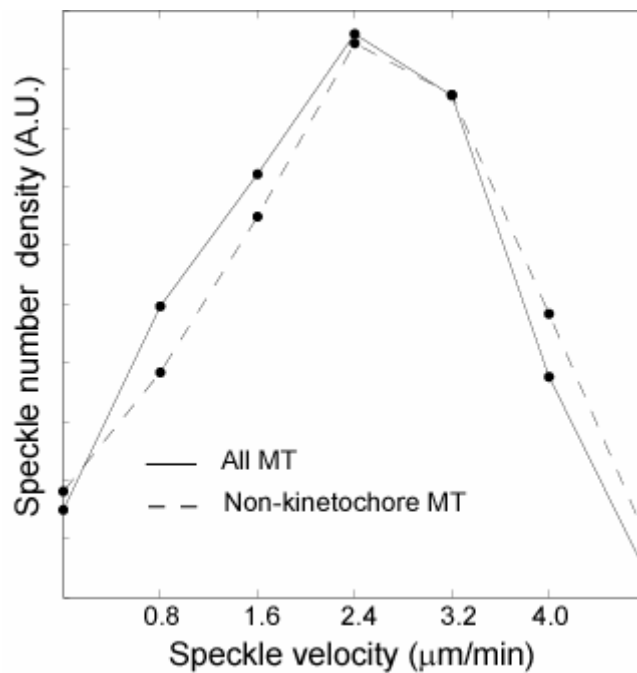


Figure 3-7

Distinguishing kinetochore microtubules from non-kinetochore microtubules, based on differences in flux. The two histograms represent the velocity distribution of the complete speckle population moving upwards (solid line) and of speckles located below the MP only (dashed line), respectively. The second population therefore contains only non-kinetochore microtubules. The two velocity distributions are very similar but the population containing only non-kinetochore microtubules exhibits slightly higher velocities making the distributions significantly different, as judged by a Kolmogorov-Smirnov statistical test (p-value = 0.0004).

3.4.4 Qualitative validation of tracking quality by speckle signal subtraction

The fraction of signal exploited for tracking can be evaluated by subtracting the signals of all speckles tracked from the raw image data. Visual inspection of the residual movies reveals in a qualitative sense how much of the speckle flow is “missed” by the software. Note that missed speckle flow does not necessarily add a new component to the overall flow field, but there is a certain probability that they could. On the other hand, if the residual images do not exhibit perceivable texture translocation, this is a sign that most of the information present in the images is exploited to recover the flow. Supplementary movies show a comparison for both actin retrograde flow and microtubule flux between the original time-lapse FSM images (left) and the corresponding residual images (right). Compared to the original data, little texture remains in the speckle-subtracted movies, and in almost all areas the signal is reduced to random flicker.

3.5 Conclusion

We have presented a new tool extending the possibilities of FSM as a quantitative method for analyzing protein dynamics in live cells. This tool was applied to two problems of biological relevance: the analysis of the F-actin flow pattern in a migrating cell and of the bi-directional microtubule poleward flux in a mitotic spindle. The exciting biological conclusions drawn from these analyses should be considered with care because in both cases they relied on the processing of a single movie and systematic experimental controls supporting the findings are missing. Our intent with these two biological applications was merely to illustrate the power of a new computational technique, which will finally allow exploitation of the full power of FSM, as proposed four years ago by (Waterman-Storer *et al.*, 1998). Now that these techniques are available, we plan to process extensive experimental data sets and to begin testing specific hypotheses in cytoskeleton biology, some of which are alluded to in the text. To do so, we face a few additional technical challenges. Currently, the processing of one movie of ~200 frames takes approximately 50 hours on a high-end, newest generation personal computer. To deal with several data sets, and to compare them quantitatively, we will have to modify our software for distributed computing in a computer network. As indicated in the text, the analyses presented in this paper represent only the tip of the iceberg in terms of the potential of this technique for FSM analysis.

3.5.1 The development of a novel tracking system was necessary to cope with the specific challenges of FSM.

In both fields of computer vision and pattern recognition, the problem of particle flow analysis is very actively studied for innumerable applications (see Grant, 1997; Veenman *et al.*, 2001; and references therein). In the biophysics community the problem has drawn significant attention over the past 10 years as well (see Cheezum *et al.*, 2001) for a comparative study of single particle tracking methods in light microscopy and its various applications to biophysical experiments). This begs the question whether we could have used an existing solution to solve our problem of speckle tracking in FSM. We have chosen to develop our own framework because on the one hand, we are not aware of an existing tracker capable of recovering reliably thousands of speckle trajectories simultaneously and on the other hand because it was critical to be able to fine-tune the program, for example to exploit intensity information for the correspondence search, which is typically neglected by other approaches. In the case of FSM, exploiting intensity information is critical as the average distance between the particles lies frequently in the range of the particle displacements themselves, making the correspondence search highly ambiguous. The solution to this problem must, therefore, rely on additional information cues.

3.5.2 The chosen particle tracking approach outperforms alternative, pattern-based tracking methods.

Alternative tracking approaches, which are often exploited in applications with image data containing a high density of features, are pattern- or window-based methods (see Corpetti *et al.*, 2002; Haussecker and Fleet, 2001) for most recent examples of tracking algorithms of this kind). This approach is especially powerful when the features are weak in contrast and proper feature extraction prior to tracking is difficult (Danuser, 2000). The basic concept of window-based tracking is to determine for a small image sub-window (e.g. an area of 25 x 25 pixels), two transition models which describe the positional and photometric evolution between subsequent frames for each pixel forming the texture of the window (Danuser, 2000). The parameters of the transition models are then estimated by maximizing an objective function, defining the similarity between the pattern in frame k , and the transformed pattern in frame $k+1$. This bears the advantage that correspondences do not have to be sought between thousands of features but only a few parameters per window have to be calculated for an optimal mapping of one pattern upon another. Indeed, we and others (Perlman *et al.*, 2001)

have attempted to apply such algorithms to FSM data with the hope that a windows-based tracking would allow us to circumvent some of the difficulties mentioned for particle-based methods. The result of such an analysis is shown in Fig. 3-8 where a speckle flow field has been recovered for the same movie as the one analyzed in Fig. 3-4. The weaknesses of this kind of analysis are evident: the windows-based tracker fails; i) in areas where the number of speckles per window changes dramatically (i.e. with strong polymer turnover); and ii) where speckle trajectories are anti-parallel, criss-cross or converge. For the F-actin meshwork displayed in Fig. 3-8, case (i) occurs at the leading edge (zone 1), where polymerization causes a constant appearance of new speckles. Case (2) occurs in areas of meshwork contraction, yielding anti-parallel (zone 2) or convergent (zone 3) speckle flow. Similar problems were encountered when applying such a tracker to the mitotic spindle data, where the anti-parallel flow of speckles made a reliable tracking of the microtubule flux impossible (data not shown). We conclude from these comparative experiments that only particle-based methods can cope with the generally complex conditions of FSM data, and that the resolution necessary for relevant biological findings, e.g. the examination of cytoskeleton contraction, requires tracking at the level of single speckles.

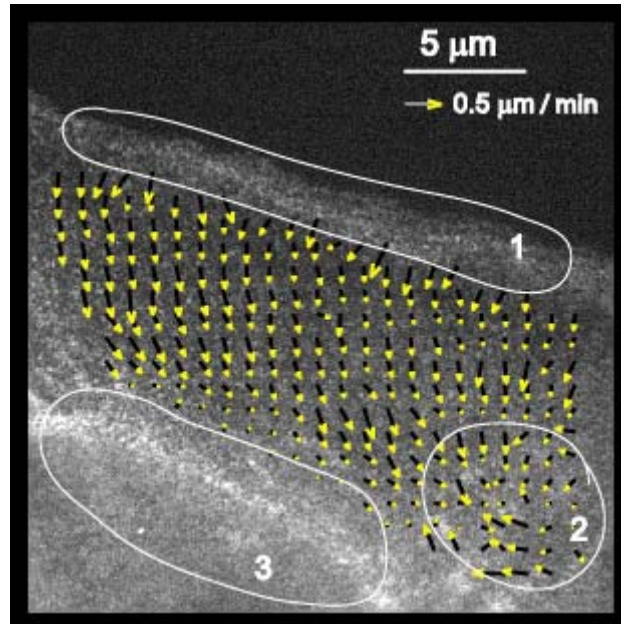


Figure 3-8

F-actin flow as recovered by a windows-based tracker. Where recovered, the flow agrees well in speed and direction with the flow field recovered by our new tracker (cf. Fig. 3-4 (b)). However, the flow cannot be recovered in some parts of the cell, and no information at the single speckle level is available. See text for a more detailed comparison of the two methods, and the specific sources of failure in the zones 1 – 3.

3.5.3 Single speckle tracking can reveal local polymer events and delivers extensive data for statistical analysis of cytoskeletal events.

A key feature of the solution we have presented in this work is that the displacements of individual speckles are accessible. This allowed us to validate the software on real data by visual inspection and hand tracking, and to perform statistical analyses at the single speckle level. In particular, we plan to extend the current framework to compute full trajectories in order to combine it with the kinetic analysis as described in Chapter 2. We will then be able to quantify depolymerization and polymerization activities that occur concurrently with flow, a project impossible to envision with a window-based tracking.

Another interesting element of a single speckle tracker is that we can determine whether a speckle population is homogeneous or heterogeneous for a property like velocity. In that way, the heterogeneity of the corresponding cytoskeletal structures becomes accessible. In general, with this novel tracker each speckle can now be considered a local reporter of polymer movement.

3.5.4 The new speckle tracker overcomes the limitations of previous kymograph analyses.

The method used until now to extract some quantitative flow information from FSM data was the kymograph analysis (Kapoor and Mitchison, 2001; Salmon *et al.*, 2002; Waterman-Storer, 2002; Waterman-Storer *et al.*, 1998). In a kymograph, successive images of the same thin rectangular image region, chosen with its long axis parallel to the average flow direction, are pasted side by side. The result of this operation displays diagonal bright streaks, whose slopes relate to the speed of the speckle flow (see Fig. 3-4 (a)). The nature of this relationship, however, is unambiguous only for simple cases. The component of the velocity perpendicular to the slice causes speckles to appear and disappear from the kymograph and also leads to underestimated speckle velocities. Nevertheless, when the amplitude of Brownian motion is limited and when the flow is coherent along the kymograph axis, such analysis and our tracking approach deliver identical results (see Fig. 3-4 (a)). Kymographs have further limits, however. For example, a kymograph cannot distinguish between a laminar convergence region and a pole, while the real nature of these flows is immediately visible in the complete mapping as shown in Fig. 3-4 (b) (C and P regions respectively).

3.6 Acknowledgements

We thank members of the Cell Division Group at the Marine Biological Laboratory, Woods Hole, MA, including Paul Maddox, Arshad Desai, Tarun Kapoor and Tim Mitchison for their help in recording the FSM sequence of the *Xenopus* extract spindle. Also, we are grateful to Alexandre Matov for writing the software for speckle flow subtraction. This project has been funded by the Swiss National Science Foundation, Grant Nr. 21-59452.99 to G.D., by the Human Frontiers in Science Program RG 5/2002 to C.WS. and G.D., and by the National Institute of Health, Grant GM60678 to E.D.S. and G.D.

4

Computational Fluorescent Speckle Microscopy II: High-Resolution Co-Mapping of F-Actin Flow and Turnover in Migrating Cells

4.1 Introduction

The cytoskeleton is a highly dynamic, multi-functional framework of filamentous (F-) actin, microtubules, and intermediate filaments and associated regulatory proteins. It forms the mechanical backbone of cell architecture and plays a fundamental role in many basic cellular activities including cell division, intracellular transport, cell motility, muscle contraction, and the regulation of cell polarity and organization. Cytoskeletal proteins have been implicated in the pathogenesis of a wide variety of human diseases, including cancer, cardiovascular, inflammatory, skin, and neurodegenerative disease, as well as fungal, bacterial and viral infections.

Fluorescent speckle microscopy (FSM) has become a powerful light microscope imaging mode for the analysis of cytoskeleton dynamics in living cells under normal and pathological physiology (Waterman-Storer and Danuser, 2002). In FSM, the random incorporation of a low concentration of fluorescently labeled subunits into the lattice of a cytoskeleton polymer results in a high spatial variation of fluorophore density along the polymer lattice. After convolution with the diffraction-limited point-spread function of the microscope, this distribution appears as a band-limited signal with a random texture of intensity maxima and minima. We define a speckle as a local intensity maximum in the signal, significantly brighter than its surroundings.

Fluorescent speckles are local reporters of translocation and turnover of the polymer lattice. In time-lapse FSM, speckle intensity changes are related to polymerization and depolymerization, whereas speckle movements are a measure for polymer flow. However, the relationships between the dynamics of speckle and polymer are only defined in a stochastic sense (Danuser and Waterman-Storer, 2003). Therefore, we began to develop software for the analysis of hundreds of thousands of speckles per FSM movie, allowing us to extract averaged information of cytoskeleton assembly, disassembly, and flow from the statistical distribution speckle trajectories and intensity changes.

In Chapter 2, we presented the computational analysis of FSM data to map the turnover of the F-actin network forming the cortex of contact-inhibited newt lung epithelial cells. The choice of this cell system was motivated by the observation that cells in culture, fully adhered to neighboring cells via adherens junctions, were non-polarized and contained F-actin which was on average spatially stationary (Waterman-Storer *et al.*, 2000a; Harris, 1999). This allowed us to concentrate the algorithmic development on measurements of actin turnover kinetics. The framework relied on the statistical analysis of the intensity changes at

the time-points of appearance and disappearance for each speckle (Chapter 2). We referred to these time-points as birth and death events, respectively. The first step of the algorithm was to classify by which mechanism a speckle appears or disappears. A speckle can either appear because of increase of the speckle foreground intensity, or because of a decrease of the background intensity in the speckle surroundings. The first case corresponds to a speckle birth due to local polymerization, the second case to a birth due to surrounding depolymerization. Similar considerations apply to the death of a speckle. The second step was then to measure the rate of intensity changes (kinetic scores) in these incidences, which is, on average, an unbiased estimator of the number of labeled monomers exchanged with the network over the period of a birth or death event. Despite the limitation to stationary networks, the analysis still involved speckle tracking, as speckle positions fluctuated due to local, motor-driven network contraction, Brownian motion, and effects inherent to the dynamic formation of speckles and their weak signal-to-noise ratio (SNR). However, tracking of these random movements could be accomplished essentially by simple nearest neighbor assignment of speckles in consecutive frames.

In a subsequent work, we demonstrated the potential of graph-based single particle tracking methods for the recovery of F-actin network transport in migrating cells (Chapter 3). We confirmed the existence of a retrograde flow away from the cell edge facing the direction of cell movement, previously described with other imaging modes (Wang 1985; Lin and Forscher 1995; Danuser and Oldenbourg, 2000; Caspi *et al.*, 2001). This flow, when coupled to substrate adhesion, is thought to drive forward cell traction. The high marker density typical to FSM permitted flow mapping at a much greater level of detail than any of these other methods, revealing novel insights of the complex dynamic organization of F-actin transport involved in the regulation of cell migration. Also, we indicated that the same algorithm can recover anti-parallel microtubule flux in mitotic spindles, originally discovered by photo-activation experiments with much lower resolution (Mitchison, 1989). An examination of the tracking quality on synthetic data indicated that 5 – 10% of the inter-frame correspondences of speckles returned by the algorithm are wrong. In addition, the tracker tends to miss 10 – 15% of the correspondences, breaking continuous speckle trajectories into several sub-trajectories. Whereas this performance is by far sufficient for the recovery of polymer flow (Chapter 3), it precluded combining flow tracking with the analysis of actin assembly and disassembly, which relies on complete speckle trajectories from appearance to disappearance (Chapter 2). Instead, we implemented a scheme based on the continuity equation of speckle field intensity in absence of polymer turnover (Vallotton *et al.*, 2003b).

Differences from this equation provide a robust measurement of the local net rate of polymer assembly or disassembly.

With the present paper we return to our original, single speckle approach to measuring polymer turnover (Chapter 2) with the aim to apply the schema also to spatially non-stationary F-actin networks. There are several advantages related to the processing of birth and death events as opposed to analyzing the entire speckle field intensity by the continuity equation approach. First, speckle births and deaths are highly localized changes of the speckle field allowing very localized measurement of assembly and disassembly dynamics. As a result, the kinetic maps produced by this method have a much higher resolution. Second, the single speckle approach selects the most meaningful event for evaluation of intensity changes. In the time point of birth or death, the contribution of local exchange of labeled subunits to the variation of the signal is significantly greater than the variations due to bleaching, focus drift or specimen movements in axial direction (Chapter 2). In contrast, the evaluation of the continuity equation includes large areas between speckles where little information on monomer exchange is available. This tends to reduce the sensitivity of detecting actual polymer turnover and makes the approach more susceptible to the before mentioned imaging artifacts.

To exploit single speckle analysis in networks with significant spatial dynamics, we had to invest in the enhancement of the tracking method. In the present paper we describe three critical steps towards this goal: (i) a hierarchical scheme for speckle extraction, which prevents the loss of speckles in ‘crowded’ image regions, i.e. when speckle signals interfere because of the limited optical resolution; (ii) a hierarchical scheme for speckle tracking, which improves the assignment of corresponding speckles in consecutive time-points through iterative processing ; and (iii) an adaptive scheme for flow filtering and interpolation, which tends to preserve flow field areas of high spatial gradients.

4.1.1 Organization and scope of the paper

In the next section we describe the cell system and experimental protocols used to test the performance of our new algorithms. Then, we lay out the technical details of the three algorithmic improvements in great detail, so that the reader may either be able to reimplement the schema in his / her own image analysis package or may be able to use our package, which will be downloadable upon request. Analyses of the F-actin turnover and flow dynamics are presented in a combined Results and Discussion section. It is not the scope of this paper to decipher the regulatory mechanisms of these dynamics by cell biological experiments, but to

report the availability of FSM as a quantitative tool with unprecedented capacity to analyze such cytoskeleton dynamics. It will now be interesting to combine FSM as the readout with carefully designed molecular perturbation studies to address the mechanisms of actin dynamics as related to migration and other cell physiological functions in a rigorously quantitative manner.

4.2 Materials and methods

4.2.1 Cell system

Cultures of newt lung epithelial cell monolayers were established as described by Reider and Hard (1990). Cells at the border of the monolayer establish a polarized morphology with the characteristic motile machinery of a protruding edge (Salmon *et al.*, 2002). However, because of strong contacts at the trailing edge to neighboring cells in the monolayer, they remain nearly stationary, with a movement of the leading edge at least one order of magnitude slower than F-actin flow analyzed in this paper. The use of this well-characterized cell system for software development and validation makes our results directly comparable to ones in Chapter 2, both in terms of technical performance as well as in terms of the similarities and distinctions between migrating and contact-inhibited cells.

Cells were cultered, microinjected with 0.5 mg/ml X-rhodamine labeled actin and prepared for imaging as described in Salmon *et al.* (2002) and Chapter 2.

4.2.2 Time-lapse spinning disk confocal FSM

Time-lapse FSM was performed using the spinning disk confocal microscope system on an inverted microscope (TE300 Quantum, Nikon, Inc) using a 100x 1.4NA Plan-Apochromatic DIC objective lens, as described in Adams *et al.* (2003). Images with an average exposure time of 500 – 1500 ms were collected at 5 or 10 sec intervals on an Orca 2 camera (Hamamatsu, Bridgewater, NJ) containing a 1280 x 1024 array of 6.7 x 6.7 μm pixels in progressive scan interline transfer configuration operated in the slow-scan (1.25 MHz) 14 bit-depth mode, where the noise is typically 3-5 electrons rms.

4.2.3 Image analysis

Raw TIFF image sequences were transferred from the MetaMorph (Downingtown, PA) software to our image processing package for FSM analysis. The program has been developed under MATLAB (The Mathworks, Nattick, MA) with some computationally

expensive modules written in C/C++. Algorithms for speckle extraction and tracking are either described in Chapter 2 or in the following section. The program runs on a standard high-end PC operated with either Linux or Windows and requires 1.0 GB RAM or more. Typical processing times of 500×500 pixels² movies of 100 frames are 10 hours on an AMD (Advanced Micro Devices, Sunnyvale, CA) Athlon XP 1.8 GHz processor. Graphical representations of the results have been programmed under MATLAB, using MATLAB's standard graphics functionality.

4.3 Algorithm

In this section, we introduce enhancements to our algorithm necessary to apply the computational framework described in Chapter 2 to F-actin networks with arbitrary spatial dynamics. In FSM time-lapse series, speckle appearance and disappearance are related to the assembly and disassembly of polymers in the network, while speckle movement indicates network translocation. Although the average flow of the network can be extracted from partial trajectories, the analysis of network assembly and disassembly, from hereon referred to as *kinetic* analysis, and delivering kinetic *scores*, requires faithful reporting of speckle birth and death events, thus complete trajectories. False birth and death events caused by deficient trajectory tracking will be misinterpreted as network turnover and deteriorate the kinetic measurements.

Fig. 4-1 outlines the new speckle extraction and tracking modules (cf. flow chart in Fig. 2-2). The modules and modifications to the previous software version are explained in detail in the following sections, along with the problems they tackle.

4.3.1 Hierarchical speckle extraction

4.3.1.1 Speckle fusions during low-pass filtering and local maximum detection

The speckle extraction relies on the definition of a speckle as a local cluster of network-bound fluorophores, convolved with the diffraction-limited point-spread function (PSF) of the light microscope. Consequently, a speckle represents a local maximum of the image in the neighborhood of the size of the PSF. Speckle candidates are extracted from the image after low-pass filtering of the raw data, which is applied to suppress signal peaks associated with high-frequency noise (cf. Chapter 2 for a full description and justification of this step).

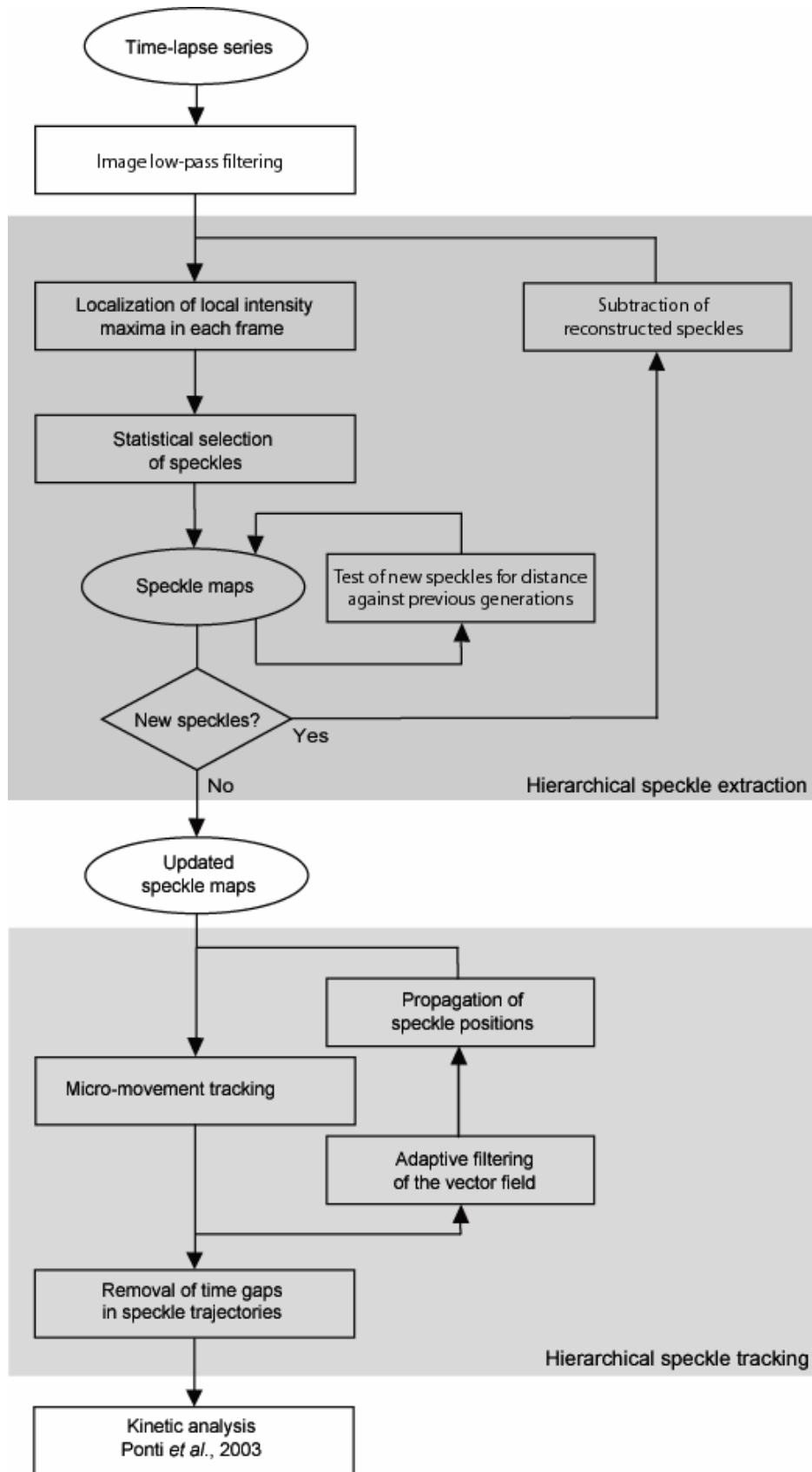


Figure 4-1

New features in the computational scheme for FSM data analysis described in Ponti *et al.* (2003). Hierarchical speckle extraction to handle signal overlaps in speckle clusters; hierarchical speckle tracking which relies on iterative propagation of speckle positions in the flow field to reduce ambiguity in the assignment corresponding speckles in consecutive frames (micro-movement tracking) and during gap closing.

Speckle candidates are identified by means of a local maximum operator with a support area equal to the lateral extension of the PSF. Because of low-pass filtering, speckle pairs separated in the raw image by a distance close to the diffraction limit of the microscope will fuse. Also, due to the low SNR of FSM data, noise-induced variations of the signal get convolved into the filtered image and may obscure the local maxima associated with true speckles. What is resolved as two nearby speckles in time point $t-1$ can thus become a single peak at time point t but get resolved again later, e.g. at $t+1$. In our birth and death statistics, we would therefore add a false speckle death at $t-1$ and a false birth at $t+1$.

To determine the extent to which speckle proximity and SNR contribute to speckle fusions, we ran Monte Carlo simulations measuring the success rate of the local maximum operator in detecting two proximate speckles. The two speckles were modeled as two-dimensional Gaussian intensity distributions with a relative intensity ratio $A=I_1/I_2$ and separated by a distance r . The distance r is limited to values greater than the Sparrow criterion (Inoué and Oldenbourg, 1995), meaning that under-noise free conditions, the two Gaussians need to be fully resolved before filtering. In the case $A=1.00$, the Sparrow criterion amounts to 3.20 pixels for $NA=1.4$, $6.7\ \mu\text{m}$ pixel size, and a magnification of 100x. With $A=2.00$, the value increases to 4.20 pixels. To simulate camera noise at a specific SNR, we perturbed the intensity distributions of the synthetic speckle signal with normally-distributed random values. This signal was then subjected to low-pass filtering followed by local maximum detection. Dependent on the settings for A , r , and SNR, the filtering causes the two speckles to fuse in one maximum.

In accordance with the speckle-to-speckle distance and intensity ratio in experimental FSM data, we analyzed the fusion characteristics for the parameter ranges $1 < A < 3$, $4.0 < r < 5.5$ pixels and four SNR values: ∞ , 10, 7, and 4. Fig 4-2 (a) displays the performance in detecting both speckles in the situation $A=1.55$ with an inter-speckle distance in the range 4.0 to 5.5 pixels. The success rate is defined as the number of Monte Carlo runs in which the local maximum operator detects two speckles after low-pass filtering divided by the total number of runs.

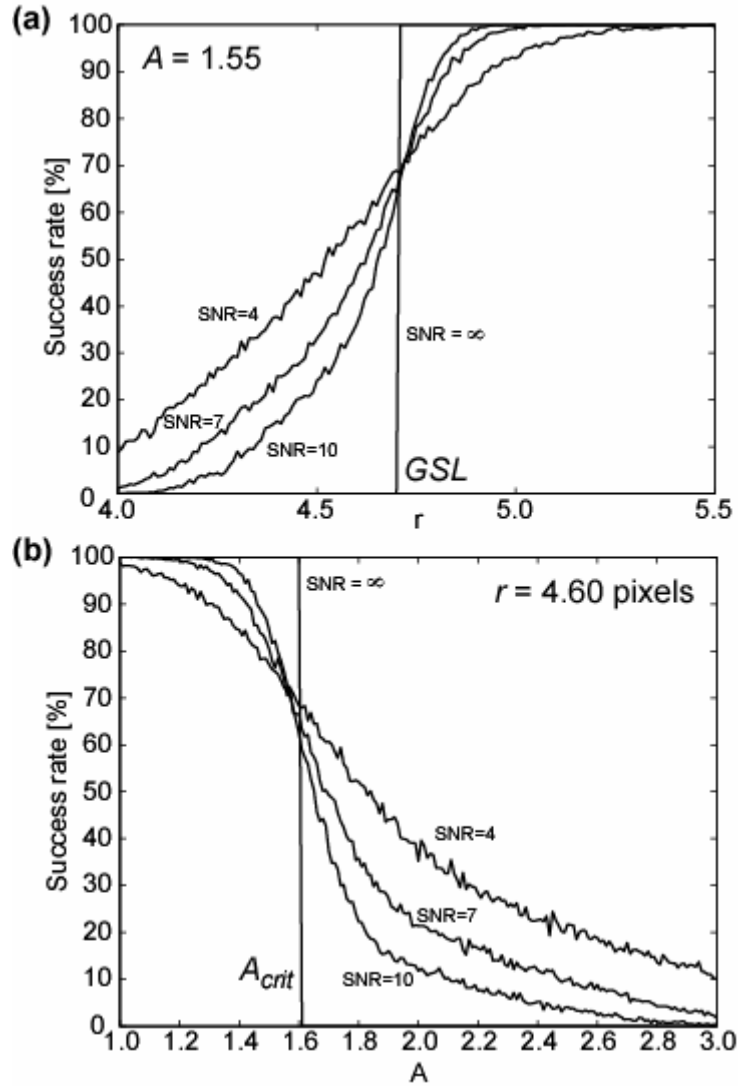


Figure 4-2

Success rate of the local maximum operator in detecting two proximate speckles after low-pass filtering. Low-pass filtering can result in speckle fusion dependent on inter-speckle distance, intensity ratio and SNR. *GSL*: generalized Sparrow limit. A_{crit} : critical intensity ratio (see text).

If no noise is added, two speckles of a certain intensity ratio will obey a specific distance limit r_0 below which the local maximum operator always fails to separate the two. Notice that due to the inequality of the peak intensities, the finite support of low-pass filter and local maximum operator, and the discretization of the signal, this limit is greater than the Sparrow limit. In the following we will refer to $r_0(A)$ as the *generalized Sparrow limit* (*GSL*). Importantly, in cases a speckle pair is detected at a distance $r < r_0$, at least one of the two represents a spurious, noise-induced speckle. As evident in Fig. 4-2 (a), the lower the

SNR the higher is the number of speckles falsely detected below the GSL. We will revisit this issue when we discuss a framework to recover lost but true speckles in clusters of multiple speckles. For distances $r > r_0$, we recognize that, dependent on the SNR, the local maximum operator can still fail to consistently detect both speckles. Below we describe a novel, hierarchical schema for the recovery of such pairs. Speckles that have so far been missed by our detector but are now retrieved by this new algorithm in the second or higher iteration step are referred to as higher-order speckles (*secondary*, *tertiary*, and so forth).

Analogously, we have examined the success rate of the local maximum operator as a function of the intensity ratio A . Fig. 4-2 (b) displays the behavior for a fixed distance $r = 4.60$ pixels. Again, there is a specific intensity ratio A_{crit} for the case $SNR = \infty$ associated with the generalized Sparrow criterion equal to this distance. Intensity ratios $A > A_{crit}$ at $SNR < \infty$ will cause the detection of spurious speckles, while true speckles are missed at $1 < A < A_{crit}$.

4.3.1.2 Hierarchical extraction of higher-order speckles

Speckles extracted by the old detection scheme described in Chapter 2 are termed *primary speckles*. The goal of our new approach is to recover *higher-order speckles* buried in clusters fused by the low-pass filtering step. How many speckles contribute to such a cluster is not known *a priori*. One method to obtain this information is by fitting mixture models of several PSFs to each cluster in the image. The *mixture model* consists of a superposition of n kernel functions and is formulated, in the case of diffraction-limited spots, as a superposition of n Gaussians, each one representing a version of the PSF shifted in space and with variable intensity. This method has successfully been used by Thomann *et al.* (2002) to detect a sparse set of fluorophore tags fused in one or two clusters. For our purpose, where potentially thousands of clusters per image have to be resolved, this approach is computationally too expensive.

Instead, we begin the speckle extraction with our old scheme, where local maxima are detected as speckle candidates and tested for statistical significance by comparing the difference between speckle peak intensity and local background estimate with the signal-dependent image noise (Chapter 2). After selection of the statistically significant candidates (speckles) we construct a superposition image of their noise-free signals and subtract it from the initial, low-pass filtered image (see below). This new difference image is again subjected to the old scheme of speckle extraction, including the statistical testing, to detect hitherto

masked, secondary speckles. The procedure is repeated until the fraction of additionally extracted speckles falls below a user-defined threshold or the maximum number of iterations allowed is reached (see below). In the following we will discuss the first two iterations of higher-order speckle extraction in greater detail. For the sake of clarity we will use the term first-order or primary speckles for those speckles extracted in the first iteration and the second-order speckles or secondary speckles for those extracted in the second iteration.

For the reconstruction of noise-free images of primary speckles, each speckle $i = \{1, \dots, N_p\}$ is represented by a Gaussian kernel located at the image position (x_i, y_i) and is scaled to match the peak intensity ΔI_i above the corresponding local background (Chapter 2).

$$G(r, s) = \Delta I_i \cdot e^{-\frac{1}{2} \frac{r^2}{s^2}} \quad (4.1)$$

The variable $r^2 = (x - x_i)^2 + (y - y_i)^2$ in Eq. (4.1) denotes the distance of a pixel at any image position (x, y) contributing to the intensity distribution of the primary speckle i . The parameter s defines the intensity drop off. For the selection of this parameter we have to account for the fact that a speckle in the filtered image is the result of a fluorophore cluster convolved twice with a low-pass filter kernel: the PSF of the microscope approximated with a Gaussian kernel with the drop-off parameter s_{PSF} matching the full-width half-maximum intensity of the exact PSF (Chapter 2) and the Gaussian low-pass filter with the parameter s_{LP} applied to suppress high-frequency noise introduced by the camera. Therefore, $G(r, s)$ in Eq. (4.1) is given by $G(r, s) = G(s_{PSF}) * G(s_{LP})$, with $s^2 = s_{PSF}^2 + s_{LP}^2$. As explained in Chapter 2, we choose $s_{PSF} = 1.25$ and $s_{LP} = 1.00$ pixels.

It has to be expected that some of the secondary speckles are artifacts created by subtraction and violate the generalized Sparrow criterion. Thus, we test in any iteration the distance of all newly extracted, higher-order speckles to any speckle extracted in any of the previous iterations against a distance criterion. To derive the distance criterion, we consider the case of two speckles modeled as the superposition of two Gaussian kernels in 1D with an intensity ratio $A = \Delta I_1 / \Delta I_2$:

$$I_{tot} = A e^{-\frac{1}{2} \frac{x^2}{s^2}} + e^{-\frac{1}{2} \frac{(x-r)^2}{s^2}} \quad (4.2)$$

Fig. 4-3 demonstrates this configuration for a speckle pair with $A = 1.5$. For sufficiently large values of r , the speckles are fully resolved by the local maximum operator

(Fig. 4-3 (a), $r > r_0 \approx 3.9$ pixels for $A=1.5$) but are lost when r falls below a critical value (Fig. 4-3 (b), $r < 3.9$ pixels). The critical situation $r = r_0$ is depicted by Fig. 4-3 (c). In contrast to the first-order extrema found in Fig. 4-3 (a) and (b), Fig. 4-3 (c) contains one second-order extremum, i.e. $I_{tot}' = I_{tot}'' = 0$. Solving this equation system, a relationship between the critical intensity ratio A_{crit} required to separate two speckles at r_0 is obtained:

$$A_{crit} = \frac{r_0 - \omega}{r_0 + \omega} \cdot e^{\left(\frac{\omega r_0}{2s^2}\right)}, \text{ with } \omega = \sqrt{r_0^2 - 4s^2}. \quad (4.3)$$

The inverse of this relationship is shown in Fig. 4-3 (d). It is used as the ultimate distance limit to avoid extraction of spurious higher-order speckles. Again, we explain the testing procedure for secondary speckles, which have to be compared to the positions of nearby primary speckles. For any of the secondary speckles $j=1, \dots, N_s$ we calculate the critical intensity ratio $A_{ij,crit}(r_{ij})$ with all primary speckles $i=1, \dots, N_{j,p}$ falling into a circular search area of radius $r_{max} = 5.5$ according to Eq. (4.3). If any $(A_{ij} = \Delta I_i / \Delta I_j) > A_{ij,crit}$, the secondary speckle j is rejected as invalid. Notice that in iterations of order $n = 3$ and higher, new speckles are tested against all speckles of orders $1, \dots, n-1$.

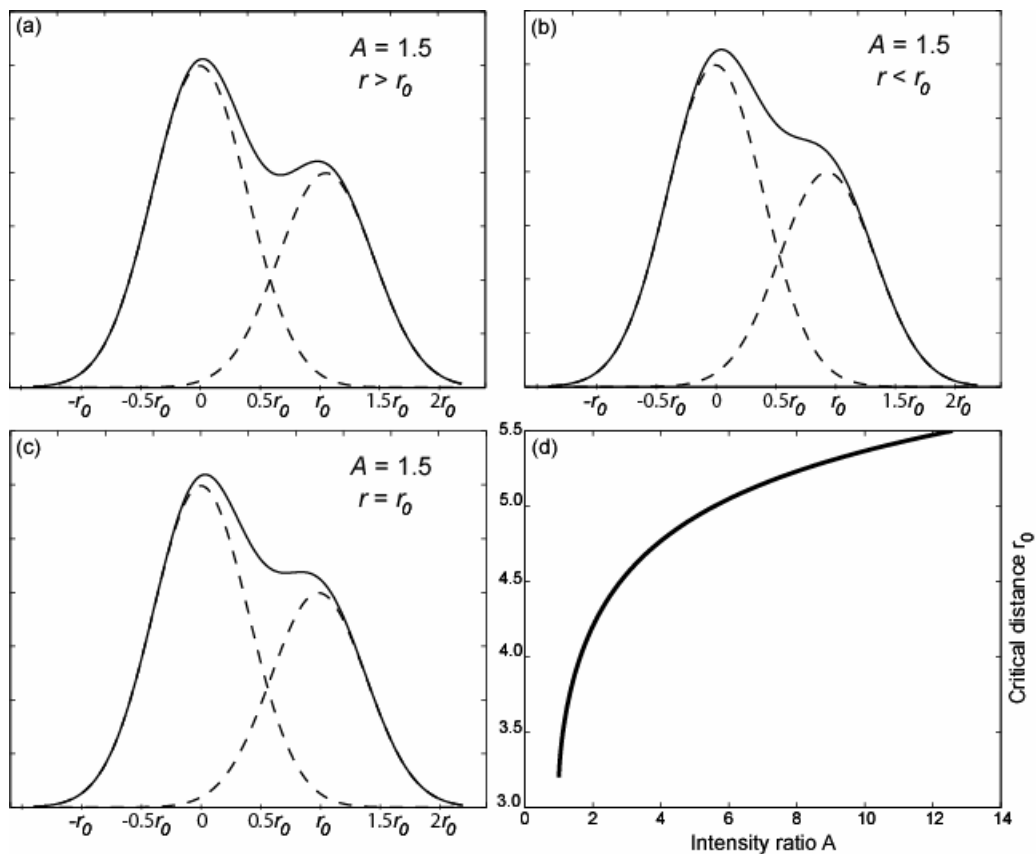


Figure 4-3

Generalized Sparrow limit (GSL) to discriminate real speckles from noise-induced artifacts after subtraction. (a) Two speckles at a distance above the GSL are fully resolved. (b) Below the GSL, speckles fuse in one feature. (c) At the GSL, both the first and the second derivative of the signal are zero. This provided a condition for the critical intensity ratio A_{crit} to resolve two speckles at distance r_0 . (d) The inverse relationship $r_0(A_{crit})$ is used to test the distance between speckles of a new generation and all speckles of previous generations in the hierarchical speckle extraction (see text for more details).

Besides the distance criterion, all newly extracted speckles have to pass the significance test against noise as described in Chapter 2. The combination of the two tests guarantees that higher-order speckles are not induced by camera noise. Furthermore, it ensures convergence of the algorithm, since at iteration n , the extracted speckles have, on average, lower intensities than in previous iterations, and thus smaller ΔI . This renders the passing of the significance test increasingly less probable for higher-order speckles.

Table 4-1 lists the relative number of recovered higher-order speckles, averaged over three experiments. Our software supports two modes of hierarchical speckle extraction: we can either perform a fixed number of iterations, independent of the increase in the number of recovered speckles; or stop the iteration when the fraction of newly extracted speckles is lower than a user-defined threshold. As a rule of thumb, iterations above 3 do not add a significant number of new speckles (see Table 4-1). Therefore, we usually stop the processing after three iterations to prevent unnecessary computation overhead.

Speckle order	Increase %	Extracted %
1	100.00	72.88 ± 2.59
2	31.64 ± 3.85	95.87 ± 0.70
3	5.04 ± 0.99	99.52 ± 0.20
4	0.59 ± 0.26	99.95 ± 0.05
5	0.07 ± 0.07	100.00

Table 4-1

Relative number of speckles recovered in higher iterations (up to order 5) averaged over 3 experiments.

In Fig. 4-4, we illustrate an example of a speckle cluster (marked by a red frame in panel (a)) and how the hierarchical scheme is able to recover multiple speckles, despite their fusion. In Fig. 4-4 (b), primary speckles are labeled in red, second-order speckles in yellow and third-order speckles in cyan. The numbers identify the speckles. To demonstrate the importance of higher-order speckles, we first concentrate on the primary speckles only. In frame t1, the local maximum operator was able to distinguish two speckles in the cluster,

numbered with *1* and *2*. In the subsequent frame *t2*, speckle *1* is again a primary speckle and can unambiguously be assigned to the number *1* in *t1* by any tracking mechanisms. Speckle *2*, however, is lost as primary speckle. In our kinetic analysis, this would be considered a speckle death and result in either a false polymerization or depolymerization event. Analogously, speckle *4* in *t2* has no partner among the primary speckles in *t1*, thus giving rise to a false speckle birth. While speckle *1* survives in all four frames as a primary speckle, the only other primary speckles with a lifetime longer than one frame is *6* (panel *t3* to *t4*). If we now consider higher-order speckles up to order three, we see that the speckle extraction is much more robust, allowing several new speckles to be tracked over all four frames, thus preventing a high number of false births and deaths. Speckle *2*, for instance, is always masked by speckle *1*, except in *t1*. Speckles *1*, *2*, and *3* are always present with *2* and *3* changing their hierarchical order repeatedly. Interestingly, speckle *3* becomes a primary speckle only in *t4*; and analogously, speckle *8* starts as a third-order speckle in *t2*, changes to second-order in *t3* and finally becomes a primary speckle in *t4*.

Once the hierarchical extraction is completed, the speckles are ready to be passed over to the hierarchical tracker which will deliver their complete trajectories.

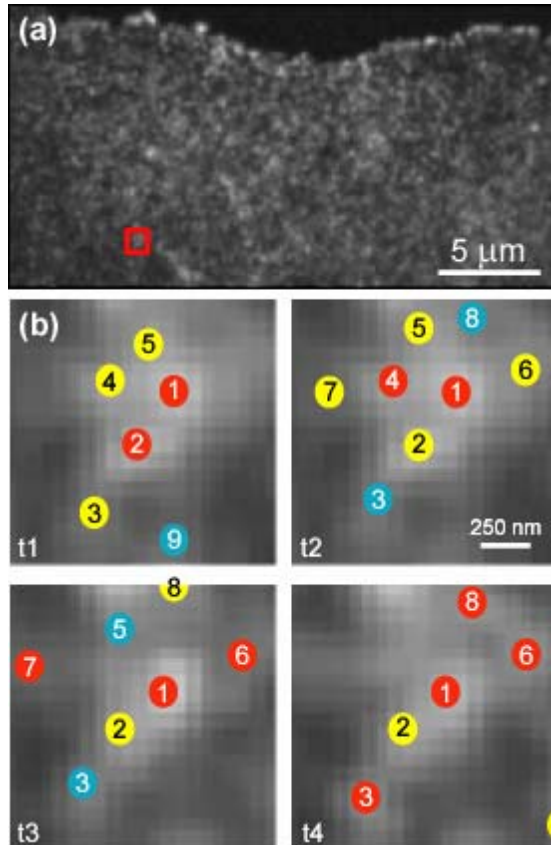


Figure 4-4

Hierarchical speckle extraction applied to the square region marked in (a). (b) Extraction in four consecutive time points (*t1* through *t4*). Red: first-order speckles; yellow: second-order speckles; cyan: third-order speckles. Numbers identify speckles.

4.3.2 Hierarchical tracking

In Chapter 2, we used a simple nearest-neighbor approach to assign speckle correspondence between consecutive frames, applying heuristic rules for the local resolution of topological conflicts. Topological conflicts occur, for example, when two speckles at time point t have the same nearest neighbor assignment in time point $t + 1$. We referred to this algorithm as the “micro-movement tracker” because it was well suited to follow the small, random movements of speckles associated with local network contraction, Brownian motion of filaments, and signal- and noise-induced fluctuations of the speckle peak position (Chapter 2). However, with the directed speckle movements associated with retrograde network flow in migrating cells, local rules tend to fail since more speckles compete for a larger number of possible assignments. Also, the assignments in one place start to influence the ones in other places, requiring a global resolution of topological conflicts. We thus have replaced our heuristic rules with a Self-Organized Map (SOM) neural network algorithm (Labonté, 2000) and further enhanced the tracker to cope with flow by means of a hierarchical approach.

Labonté’s algorithm cannot be used directly for the entire set of speckles to be assigned between two consecutive frames. When applied to thousands of particles which may disappear in t and new ones appear in $t+1$, the scheme fails to converge. Instead, we first extract unambiguous nearest-neighbor matches and eliminate those links from the input data of the SOM neuronal network algorithm. Typically, there are only a few tens to hundreds of topologically conflicting speckles remaining, whose correspondences can be resolved by the neural network. Also Labonté’s algorithm does preferably link speckles whose displacement is as short as possible. In contrast to our old micro-movement tracker, however, it guarantees the selection of the globally best solution, and will locally prefer non-nearest-neighbor assignments, should they be advantageous in the global configuration.

Despite the quasi-global assignment, the modified SOM neuronal network algorithm still tends to fail when applied to the reconstruction of F-actin network flow in migrating cells, the reason being a mean particle displacement in the range of or larger than the average minimal distance between speckles. Under these conditions, any tracker pursuing a minimal displacement strategy will perform insufficiently, no matter which method is used for the resolution of topological conflicts. To remedy this problem we exploit the fact that the movement of speckles probing the flow of an F-actin network is a superposition of two components: a component reflecting coherent flow, i.e. the velocities of speckles are correlated over a certain distance because of the mechanical coupling of network sites through

interconnected filaments; and a component reflecting spatially uncorrelated, random fluctuations of the speckle position around the coherent flow, of which the sources are described above. In our movies, both components have similar magnitudes. Critically, each component alone has an average magnitude smaller than the minimal distance between speckles which allows the application of the modified SOM neuronal network in a hierarchical framework to cope with the larger speckle movements accompanying F-actin network flow.

In the first iteration speckles are tracked as described above and a set of links $\mathbf{u}_i, i = 1, \dots, N_l$ are generated, where N_l denotes the number of links. Many of the returned links are wrong or deviate from the general direction of flow. Nevertheless, a sufficiently large sub-set does reflect the average direction and speed of the underlying network flow. Assuming that the vectors of wrong speckle assignments and random fluctuations have an expectation value close to zero, we can obtain a first estimate of the coherent flow component $\tilde{\mathbf{u}}_i$ by

$$\tilde{\mathbf{u}}_i = \frac{\rho_{ij} \mathbf{u}_j}{\sum_{j=1}^{N_l} \rho_{ij}}. \quad (4.4)$$

Eq. (4.4) uses Einstein summation over common indices. For visualization purposes, the same equation is applied for the interpolation of the flow component on $k = 1, \dots, N_g$ points on a regular grid. The correlation function ρ_{ij} for averaging or interpolation is defined as

$$\rho_{ij} = e^{-\frac{d_{ij}^2}{d_0^2}}, \quad (4.5)$$

where $d_{ij} = \sqrt{\Delta x_{ij}^2 + \Delta y_{ij}^2}$ denotes the distance between the origin of the filtered displacement or the grid point i and the origin of any of the unfiltered raw displacements j , with $\Delta x_{ij} = (x_j - x_i)$ and $\Delta y_{ij} = (y_j - y_i)$. The correlation length d_0 is chosen in consideration of the network deformability. The more rigid the network, the more are speckle links in spatially separated locations of the network correlated, rendering an averaging over longer distances more appropriate.

In hierarchical tracking, we exploit the filtered flow $\tilde{\mathbf{u}}_i$ to propagate the likely position of speckle i in $t+1$ by $\mathbf{x}_i^*(t+1) = \mathbf{x}_i(t) + \tilde{\mathbf{u}}_i$. Instead of seeking speckle correspondence between consecutive time points, the assignment is now done for the propagated and

measured speckle positions in $t+1$. The better the averaging the closer are the propagated positions to their targets, reducing the fraction of wrong matches. With every iteration the propagation quality gets enhanced. In the limit of convergence, correspondences have to be recovered over the magnitude of only the random component of speckle movement, for which, as argued earlier, a nearest-neighbor assignments with global resolution of topological conflicts provides the optimal solution. Convergence is typically achieved after two iterations.

Fig. 4-5 shows an example of how the hierarchical tracker can increase the quality of recovered matches between the first and second iteration. Panel (a) displays the links returned by the modified SOM neuronal network algorithm after the first iteration. The corresponding averaged flow is shown in panel (b). Panel (c) displays the links recovered after propagating the speckle positions with this field. The cell analyzed in this example exhibited strong polymerization at the leading edge (see also Results below). Thus, speckles in frame t encounter many new, nearby speckles in frame $t+1$ to be considered as possible matches for a nearest-neighbor tracker. Without information about the coherent movement component of the speckle field, the tracker will simply link the closest speckle pairs subject to resolving topological conflicts. In panel (a), this yields fewer links with a broader distribution of directions. Notice that a relatively large portion of the vectors actually point toward the cell edge, which is unlikely since it is well established that F-actin exhibits retrograde flow away from the edge in migrating cells. Panel (c) indicates that this limitation of nearest-neighbor tracking is greatly remedied by the hierarchical approach. The asterisk (*) in the insets highlights two vectors pointing toward the cell edge in panel (a) which are corrected in (c). A larger number of speckle links is extracted and a much higher fraction of them reflect retrograde flow. We have to point out, however, that the chosen hierarchical scheme converges to a robust solution only if the result of the first iteration is sufficiently accurate to extract the trends of coherent flow. This requirement is generally fulfilled if the frame rate is high enough to render the magnitudes of coherent and random displacements smaller than the mean distance between speckles.

Propagation of speckle movement is also applied to the gap closer of speckle trajectories (Chapter 2). The purpose of gap closing is to recover speckle positions in time points where the speckle temporarily remains undetected because of noise. The original criterion for such a recovery was that a speckle existing in frame $t-1$ and $t+1$ would have a weak local intensity maximum in the intersection of two circular search regions centered at the speckle positions in $t-1$ and $t+1$, respectively. Now, this criterion is modified to the

intersection of two circular search regions, the first centered at $\mathbf{x}_i^*(t) = \mathbf{x}_i(t-1) + \tilde{\mathbf{u}}_i(t-1)$, the second at $\mathbf{x}_i^{**}(t) = \mathbf{x}_i(t+1) - \tilde{\mathbf{u}}_i(t+1)$.

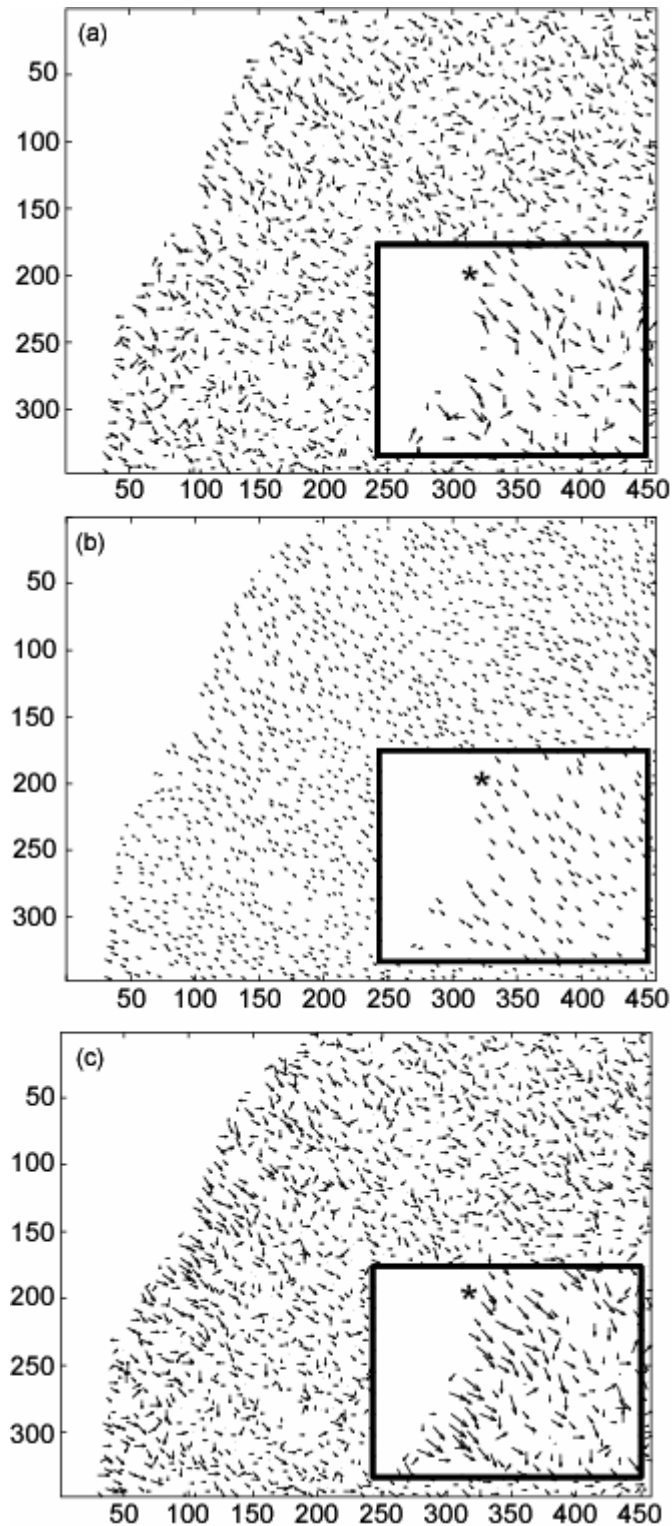


Figure 4-5

Hierarchical speckle tracking. (a) Nearest-neighbor tracking bound to fail when speckle displacements are larger than the mean distance between speckles, and where addition/removal of speckles create ambiguous candidate assignments. Both cases occur particularly at the leading edge of motile cells (inset). (b) Filtered vector field used to propagate speckle positions in the second iteration of tracking. (c) Vector field reconstruction after second iteration. Asterisk highlights vectors pointing in anterograde direction in (a), but corrected in (c). All vectors are 3x enlarged for better visualization.

4.3.3 Adaptive flow filtering and tracking

Hierarchical tracking relies on accurate flow filtering according to Eq. (4.4). As described in the previous section, the filter kernel is initially chosen independent of the flow structure. The choice has to compromise between preservation of details in the flow field and adequate averaging of random displacements. Particularly in the case of a flow field with an inhomogeneous distribution of areas of coherent flow and areas of incoherent flow, which may occur in contractile actin assemblies, the finding of a tolerable compromise can be impossible. To solve this, we have implemented a scheme, where the correlation length is iteratively adapted to the local flow structure. We take the magnitude of the divergence operator applied to the flow field as the measure for the local incoherence of flow, and adapt d_0 accordingly. Given the speckle links in any iteration of the hierarchical tracker, we calculate the divergence of the flow field at the position of a speckle i as:

$$\operatorname{div}(\mathbf{u}_i) = \underbrace{\left(\frac{\partial \rho_{ij}}{d(\Delta x)} \cdot \frac{\partial(\Delta x)}{dx_i} \right)}_{K_u} \cdot u_j + \underbrace{\left(\frac{\partial \rho_{ij}}{d(\Delta y)} \cdot \frac{\partial(\Delta y)}{dx_i} \right)}_{K_v} \cdot v_j, \quad (4.6)$$

with $\mathbf{u} = [u, v]$. The notation of Eq. (4.6) suggests that the divergence can be computed elegantly by first convolving the scalar field of all speckle displacements in direction u with a kernel K_u followed by convolution of all speckle displacements in direction v with a kernel K_v . The new correlation length for adaptive filtering in speckle i is then determined as

$$d_0^{(i)} = \frac{d_0^{user}}{1 + \alpha \left| \frac{\operatorname{div}(\mathbf{u}_i)}{\max(\operatorname{div}(\mathbf{u}_i))} \right|}. \quad (4.7)$$

The user has to define two parameters. As with non-adaptive filtering, a correlation length d_0^{user} which determines the maximum correlation length; and the gain parameter α , which determines the degree of length scaling. We currently restrict α to the range $[0, 1]$, i.e. the shortest correlation length is half the user-defined d_0^{user} . It turns out that for our cell system, F-actin flow is sufficiently homogeneous so that a relatively moderate adaptation provides satisfactory results. We also apply divergence-controlled filter kernels for the interpolation of flow fields onto regular grids, where the adaptive correlation length is interpolated from the $d_0^{(i)}$ values in adjacent speckles.

4.4 Results and discussion

The purpose of the three described algorithmic extensions is to retrieve speckle trajectories from birth to death without interrupts. Complete trajectories are required for robust measurements of network assembly and disassembly using statistical evaluation of intensity fluctuations at the time points of speckle births and deaths (Chapter 2). Interrupts in the trajectories introduce false birth and death events to these statistics and thus deteriorate the turnover rates. Our hierarchical speckle extraction targets at the apparent loss of speckles due to temporary signal interferences with adjacent speckles. The tracker itself is enhanced by yet another hierarchical scheme that can cope with speckle movements due to both cytoskeletal flow and random positional jitter. This has allowed us for the first time to apply the high resolution kinetic analysis described in (Chapter 2) to migrating cells, where the actin cytoskeleton undergoes characteristic myosin II motor-dependent retrograde flow.

4.4.1 Cell model for the analysis of the algorithmic performance

To assess the performance of the new algorithms we have analyzed four FSM time lapse series of F-actin dynamics at the ventral surface of living newt lung epithelial cells, grown in monolayers adhered to glass coverslips (see Materials and Methods). In this paper we concentrate on the technological aspects of these experiments. We will allude to some of the novel biological results that can now be obtained as a consequence of the novel high-resolution kinetic mapping, but defer more exhaustive analysis of molecular mechanisms underlying actin dynamics to a separate paper. Cells at the border of the monolayer establish a motile machinery, involving the dynamic assembly and disassembly, as well as myosin-dependent retrograde transport of an F-actin network as described in previous studies (Salmon *et al.*, 2002; Gupton *et al.*, 2002; Vallotton *et al.*, 2003b; Chapter 3). Briefly, a lamellipodium forms at the leading edge, facing the direction of migration, with a thickness of ~ 200 nm (Abraham *et al.*, 1999) and a width of 3 - 5 μm . It consists of a dense network of actin filaments whose fast-growing, barbed ends polymerize adjacent to the leading edge (Pollard *et al.*, 2000). In the lamellum next to the lamellipodium, the network splits to define actin cortices that provide mechanical support to the ventral and dorsal sides of the cell. Also, ventral lamellum F-actin network binds to cell-substrate adhesion sites. It couples to the ventral cytoskeleton of the main cell body via a convergence zone that is rich in myosin II. Both the lamellipodium and lamellum networks undergo retrograde flow and meet in a convergence zone with a slow anterograde flow from the cell body. The generally faster

lamellipodium flow depends on actin polymerization, whereas lamellum flow is sensitive to the perturbation of myosin motor activity (Waterman-Storer and Salmon, 1997; Gupton *et al.*, 2002; Vallotton *et al.*, 2003b), suggesting that the two flows are subject to different molecular mechanisms.

The movies *M1* to *M3* (see supplementary data) illustrate this polarized morphology and dynamic organization. The cells in *M2* and *M3* exhibit higher protrusive activity than the one in *M1*. For comparison with F-actin dynamics in the cortex of contact-inhibited cells (Chapter 2), we again show movie *C1*. As discussed in Waterman-Storer *et al.* (2000) these cells do not exhibit directed flow from the edges, but still maintain a dynamic turnover of F-actin, visible as a random flicker of the speckle signal.

4.4.2 Hierarchical speckle extraction results in a decrease of the mean intensity and of the standard deviation of the speckle signal

To test the applicability of the subtraction scheme used in hierarchical speckle extraction, we first analyzed the mean image intensity and standard deviation as measures of signal brightness and speckle contrast (Waterman-Storer and Salmon, 1998) in different regions of the cell in *M1*. As a control, we performed the same analysis on (non-speckled) background regions of the same images. We considered four sets of images: the raw FSM images (set *R*), the low-pass filtered images (*L*), and the same low-pass filtered images after one (*S1*) and two (*S2*) speckle subtractions, respectively.

In the background region, where it is unlikely that local maxima are classified as speckles, hierarchical speckle subtraction is activated very rarely. Therefore the images in *L*, *S1*, and *S2* were nearly identical, with equal mean intensity and standard deviation (Table 4-2). Compared to *R*, the standard deviations of *L*, *S1*, and *S2* were reduced by a factor 3.72, as a result of low-pass filtering. The same analysis on a synthetic field of random intensity values reduces the standard deviation between raw and filtered data by 3.54. This confirms that the signal in non-fluorescent areas of FSM movies is essentially associated with normally distributed camera dark noise.

When the same analysis was performed on speckled regions, both the mean and standard deviation decreased from *L* to *S1* and to *S2* (Table 4-2). Between *R* and *L* the mean was approximately constant and the decrease in standard deviation reflected the suppression of noise by low-pass filtering. Whereas the origin of the decrease in mean intensity from *L* to *S1* to *S2* is expected from the subtraction scheme, the simultaneous lowering of the standard deviation is more exciting. It confirms that with each subtraction step true speckle information

is removed from the images. The more true speckles are subtracted, the more the signal will resemble a background field with no speckles and thus low standard deviation. Also, it indicates that the subtraction scheme does not introduce new, artifactual features in the speckle signal. In lamellipodium regions, the standard deviation decreased by 29% from L to $S1$ and by 34% from L to $S2$. The relatively small percentage change from the first to the second subtraction is consistent with the low fraction of newly extracted speckles in the second iteration (see Table 4-1). In the lamellum, the decreases in standard deviation from L to $S1$ and from L to $S2$ were 39% and 43%, respectively. The difference between lamellipodium and lamellum can be explained by the higher mean signal intensity in the lamellipodium, likely caused by higher filament density, which diffuses the speckle pattern and thus reduces the efficiency of the subtraction scheme. Similar findings were made for the convergence zone (27% from L to $S1$ and 32% from L to $S2$) and the cell body (36% from L to $S1$ and 39% from L to $S2$). We conclude that the subtraction scheme for hierarchical speckle extraction is appropriate to recover additional speckles, otherwise masked by the limited resolution of the imaging and the image processing procedures.

		R	L	S1	S2
Background	mean	0.143	0.143	0.143	0.143
	std	0.037	0.010	0.007	0.007
Lamellipodium	mean	0.356	0.356	0.323	0.317
	std	0.076	0.051	0.037	0.034
Lamellum	mean	0.307	0.307	0.275	0.270
	std	0.071	0.044	0.027	0.025
Convergence zone	mean	0.671	0.671	0.635	0.625
	std	0.107	0.080	0.059	0.054
Cell body	mean	0.502	0.502	0.481	0.477
	std	0.060	0.030	0.019	0.018

Table 4-2

Dependence of mean and standard deviation (std) of the speckled image signal on the processing. (R) raw signal; (L) low-pass filtered signal; (S1) signal after subtraction of primary speckles; (S2) signal after extraction of secondary speckles.

4.4.3 The role of higher-order speckles in the extraction of complete trajectories

We follow up on the previous conclusion and examine the implication of hierarchical speckle extraction not only on the level of the overall signal but for each higher-order speckle. The first question addressed is how many of them represent real image features versus how

many are artifacts generated by the subtraction scheme. The example of Fig. 4-4 (discussed in the Algorithm) provided evidence that they indeed carry valuable information which would otherwise be lost. However, as much as the subtraction scheme can prevent losing this information by recovery of higher-order speckles, it could also introduce new image features that are misinterpreted as speckles.

We reasoned that if higher-order speckles were artifactual features, they would neither share the characteristics of local contrast and statistical significance of intensity variation at the time points of birth and death with primary speckles, nor integrate with the population of primary speckles in terms of lifetime and flow. In contrast, if they do represent significant features in the speckle signal, they will increase the lifetime, improve the statistics of kinetic scores measured at the birth and death events, and contribute to a more robust flow tracking.

4.4.4 Hierarchical speckle extraction increases the number of kinetic scores by 20% in spatially stationary F-actin meshworks

Table 4-3 presents extended statistics of the contributions of higher-order speckled to these measurements. In contact-inhibited cells (*CI*), hierarchical extraction up to third-order speckles yields 35.8% more speckles than with an extraction of only primary speckles. After tracking and aggregation of speckle links into complete trajectories, we obtain 23.0% more birth and death events. The percentage increase of speckles is clearly higher than the percentage increase in the number of birth and death events, indicating that many of the additional speckle positions are actually integrated in trajectories of speckles with at least two primary speckle positions.

At this point we have to reintroduce the notion of *ghost speckles* (Chapter 2), which are speckles with a lifetime of only 1 frame. Those are not counted towards the statistics of birth and death events. However, speckles that are classified as ghosts with primary speckle selection can become regular speckles as higher-order speckle positions are added to generate a trajectory with a lifetime of two frames or longer. Remarkably, the percentage of ghost speckles remains unchanged with hierarchical extraction (Table 4-3 last row), suggesting that ghost speckles removed from the list of primary speckles are substituted by an equal amount of new ghost speckles associated with unlinked higher-order speckles.

All these cases are expected to prolong the speckle lifetime significantly. Yet, the mean speckle lifetime changes only slightly, from 45.9 to 46.5 s (+1.4%). This could be explained in two ways: i) many of the higher-order speckles fill gaps in trajectories of primary speckles that were bridged in the original algorithm by the gap closer (Chapter 2).

	<i>C1</i>			<i>M1</i>			<i>M2</i>			<i>M3</i>		
	(I)	(II)	(III)	(I)	(II)	(III)	(I)	(II)	(III)	(I)	(II)	(III)
Total number of speckles	98449	133659 +35.77	133670 +0.01% +35.78 %	222452	290785 +30.72%	290880 +0.03% +30.76%	226204	287978 +27.31%	288012 +0.01% +27.32%	156595	204039 +30.30%	211315 +3.57% +34.94%
Total number of events	44977	55340 +23.04%	55236 -0.1879% +22.81%	140794	156521 +11.17%	153227 -2.10% +8.83%	160270	189883 +18.48%	184823 -2.66% +15.32%	103291	123498 +19.56%	107043 -13.32% +3.63%
Total number of valid events	24191	30180 +24.76%	30083 -0.32% +24.36%	74249	89499 +20.54%	87270 -2.49% +17.54%	72283	86168 +19.21%	85057 -1.29% +17.67%	51906	65148 +25.51%	57999 -10.97% +11.74%
Total number of scores	8876	10666 +20.17%	10598 -0.64% +19.40%	35676	43893 +23.03%	42707 -2.70% +19.71%	34320	43135 +25.68%	42484 -1.51% +23.79%	26545	34203 +28.85%	30520 -10.77% +14.97%
Total number of complete trajectories	21654	26528 +22.51%	26476 -0.20% +22.27%	67465	74432 +10.33%	72786 -2.21% +7.89%	76343	90076 +17.99%	87545 -2.81% +14.67%	49940	59502 +19.15%	51205 -13.94% +2.53%
Number of gaps closed	535	400 -25.23%	411 +2.75% -23.18%	749	1421 +89.72%	1516 +6.694% +102.40%	2581	638 -75.28%	672 +5.33% -73.96%	479	194 -59.50%	576 +196.91% +20.25%
Lifetime (s)	45.9	46.5 +1.42%	46.5 +0.03% +1.45%	62.2	68.6 +10.34%	70.0 +2.11% +12.67%	61.6	65.7 +6.60%	66.5 +1.26% +7.94%	65.4	67.3 +2.95%	78.5 +16.53% +19.97%
Ghost speckles (% of all complete trajectories)	47	47 +0%	47 +0% +0%	48	44 -8.33%	44 +0% -8.33%	56	56 +0%	55 -1.79% -1.79%	50	48 -4.00%	47 -2.08% -6.00%

Table 4-3

Statistics of the influence of hierarchical speckle extraction and tracking on the number of speckles, ghost speckles, birth and death events, kinetic scores, and the lifetime of speckles. (I) primary speckles only, no hierarchical tracking; (II) hierarchical speckle extraction (up to order 3), no hierarchical tracking; (III) hierarchical speckle extraction (up to order 3), hierarchical tracking (two iterations). *Total number of speckles*: number of speckles extracted, comprising gaps (weak local maxima rescued to the status of speckles). *Total number of events*: total number of speckle appearances and disappearances. *Total number of valid events*: total number of events belonging to trajectories longer than 1. *Total number of scores*: number of statistically significant speckle births and deaths. *Total number of complete trajectories*: number of speckle trajectories linked from speckle appearance to disappearance. *Number of gaps closed*: number of weak local maxima temporarily masked by noise and restored by the gap closing algorithm to rescue false trajectory interrupts (see text). *Ghost speckles (% of all complete trajectories)*: fraction of all speckles with a complete trajectory with a lifetime of one frame only. See text for a discussion of these results.

Indeed, the number of closed gaps drops by 25.2 % (Table 4-3); ii) higher-order speckles form new trajectories with lifetimes > 1 frame, or complement primary ghost speckles to trajectories with lifetimes > 1 frame. But both kinds have a lifetime significantly (40-50%) shorter than the one of trajectories with a lifetime > 1 retrieved without hierarchical speckle extraction.

Whether these new speckle classes add significant information to the computation of kinetic scores is statistically verified by testing that intensity changes in the time points of birth and death reflect the actual exchange of labeled monomers and are not only caused by noise (Chapter 2). From all valid events in trajectories with only primary speckles, merely 36.7% are significant for the calculation of kinetic scores. Including higher-order speckles, this fraction further drops to 35.3%, indicating that indeed some of the trajectories gained by higher-order speckle extraction do not contribute to the kinetic mapping at all. Nevertheless, the total increase of significant birth and death events (scores) amounts to 20.2%, enhancing the resolution of the kinetic mapping remarkably.

All the above mentioned values have been calculated without hierarchical tracking. The application of hierarchical tracking in spatially stationary F-actin networks does not change the situation. Since the mean field of speckle displacements is close to 0 (not shown), the propagation scheme barely moves the speckles and reiterated tracking returns the same result as the first round of tracking without propagation.

4.4.5 Hierarchical speckle extraction in combination with hierarchical tracking increases the number of kinetic scores by 26% in F-actin meshworks undergoing flow, and prolongs the lifetimes by 13%.

In networks subjected to retrograde flow, the percentage of additional speckles retrieved by hierarchical extraction amounts to 29.4 ± 1.9 % (n=3 experiments *M1-M3*, ~600'000 speckles). This is less than for a stationary network. On the other hand, the percentage increase in significant scores is larger (25.9 ± 1.7 %), suggesting that higher-order speckles tend to carry more relevant information in translocating than in stationary fields. This is supported further by the larger relative prolongation of speckle lifetime (6.6 ± 2.1 % *M1-M3* as compared to 1.3% in *CI*). Also, for a field with significant flow, the application of the hierarchical tracker has a critical effect on the lifetime. In all movies the lifetime is further increased by hierarchical tracking, with the largest relative change found in *M3* (+16.5%). In combination, hierarchical speckle extraction and hierarchical tracking result in a prolongation of the lifetime of 13.5 ± 3.5 % (*M1-M3*).

A second notable difference between stationary and motile networks concerns the role of gap closing. With the exception of *M2*, the inclusion of higher-order speckles in motile networks is accompanied by a large number of additionally closed gaps in speckle trajectories, whereas it drops in stationary ones. This indicates that in motile networks, higher-order speckles tend to extend sub-trajectories belonging to the same speckle until they are separated by only one frame, so that they can be linked to complete trajectories by the gap closing scheme.

As with the stationary network, the fraction of ghost speckles remains unaffected, confirming that ghost speckles do not arise from insufficient speckle extraction or tracking but represent a significant feature of the FSM signal. As discussed in Chapter 2, we suspect that they are associated with fast network contraction and filament turnover events occurring at rates beyond the currently achievable frame rate.

4.4.6 The role of higher-order speckles in mapping F-actin turnover

Fig. 4-6 compares a kinetic map extracted from movie *CI* using primary speckles only (a) and speckles up to third order (b). Arrowheads point to regions where false polymerization activity is reported by panel (a). Arrows indicate false depolymerization. The symbol * shows a peak of polymerization in (b) that was underestimated in (a). Although the fundamental properties of cyclic turnover of cortical actin in a dynamic equilibrium, described in Chapter 2 based on primary speckles, do not alter, Fig. 4-6 indicates that higher-order speckles do shift the peak locations of polymerization and depolymerization. This will become relevant when FSM is being used to map out the kinetics at the micron scale, e.g. when looking at actin cortex dynamics in response to endocytic events.

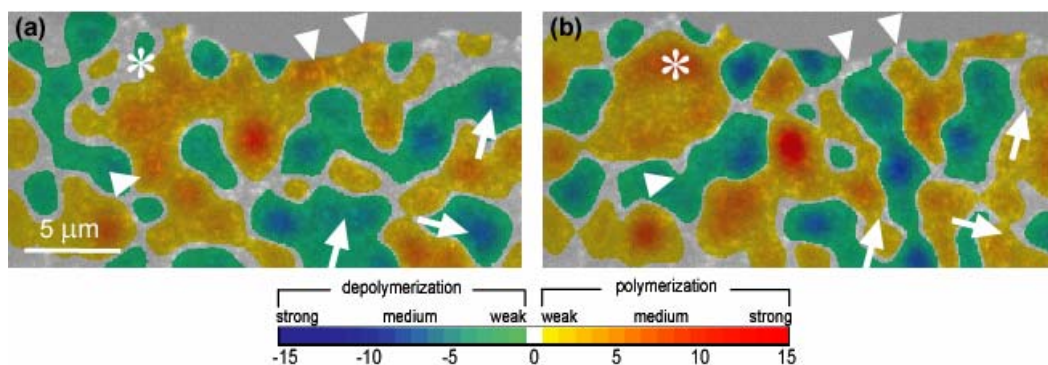


Figure 4-6

Comparison of kinetic scores calculated for movie *CI* from primary speckles (a) and speckles up to order three (b). Arrowhead and arrows highlight regions where wrong local polymerization respectively depolymerization activity is recorded in (a). The * symbol indicates a strong local polymerization in (b) which is underestimated in (a).

4.4.7 The role of higher-order speckles in mapping F-actin flow

Fig. 4-7 (a) shows the results of the hierarchical tracking of all speckles up to order three for one frame pair of experiment *MI*. The contribution of primary speckles versus higher-order speckles are displayed in Fig. 4-7 (b) and (c), respectively. Higher-order speckles contribute 33% to the displacement vectors. The corresponding displacement field (c) reflects the same overall flow structure as panels (a) and (b), despite the lower vector density. We conclude that higher-order speckles carry the same flow information as primary speckles. Panel (d) shows the vector differences between (b) and (c), interpolated onto a regular grid and enlarged 2x for better visualization.

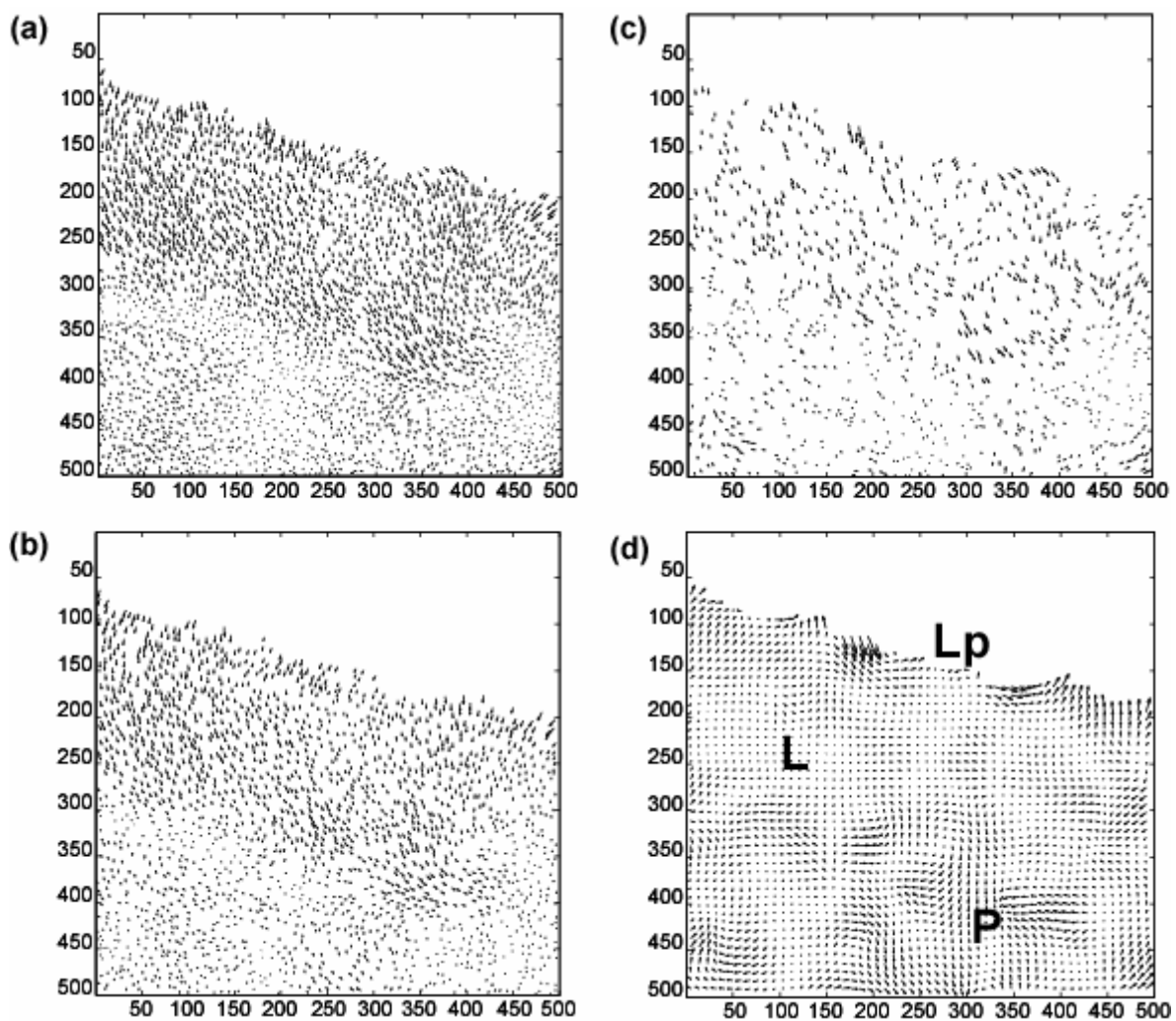


Figure 4-7

Flow information carried by higher-order speckles (investigated in movie *MI*). (a) Average flow field recovered from trajectories of speckles up to order three. (b) Average flow field recovered from primary speckle trajectories. (c) Average flow field recovered from speckles of order two and three. (d) Difference map for the vector fields in (b) and (c) interpolated on a regular grid ($0.7 \times 0.7 \mu\text{m}$) and enlarged 2x.

In zones of coherent flow, like the lamellum (L), the differences are small. In contrast, in regions of high speckle density like the lamellipodium (Lp), which exhibit a significant amount of speckle fusion, or in zones of network compression (e.g. the pole P present in the convergence zone), the differences are larger. It is in these most critical zones, where hierarchical speckle extraction enhances the robustness of flow recovery.

4.4.8 What does the lifetime of a speckle mean?

Now that we are confident that the majority of speckles is properly tracked from birth to death, we revisit the question of what the lifetime of a speckle means in terms of polymer turnover. As discussed in Chapter 2, multi-fluorophore speckles can appear because of association of labeled monomers in the PSF volume of the speckle signal (polymerization) or because of dissociation of labels in the immediate surroundings (depolymerization). By analogy, a speckle can disappear because of label removal from the PSF volume of the speckle signal or because new label is added to the neighborhood. This behavior fundamentally contrasts the characteristics of single fluorophore speckles, where the appearance and disappearance unambiguously report polymerization and depolymerization, respectively (Watanabe and Mitchison, 2002).

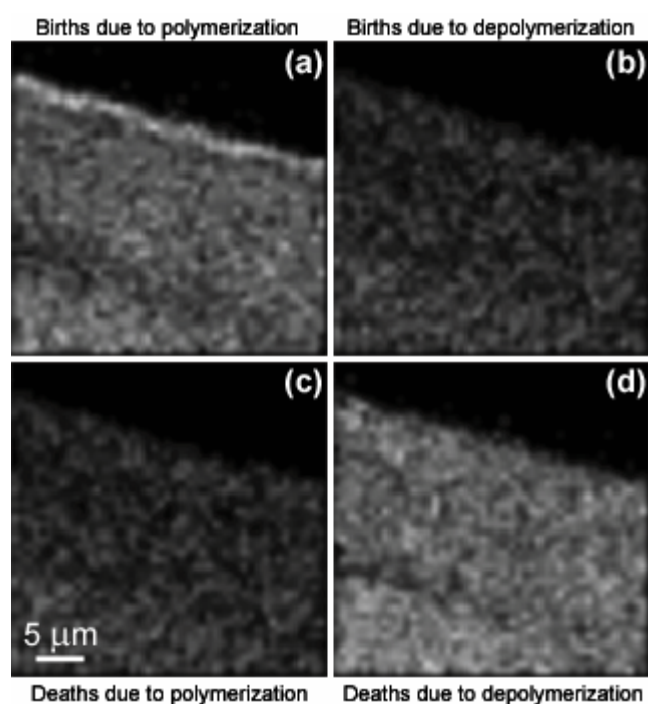


Figure 4-8

Frequency distribution of occurrence of the four speckle birth/death event classes (see text) in movie *MI*. (a) Speckle births due to polymerization. (b) Speckle births due to depolymerization. (c) Speckle deaths due to polymerization. (d) Speckle deaths due to depolymerization.

The frequency distribution of occurrence of the four event classes is illustrated in Fig. 4-8. 68.07% of all speckle births are due to network polymerization, whereas 31.93% are due to depolymerization. Speckle deaths are distributed similarly: 25.22% of speckle deaths are due to polymerization and 74.78% to depolymerization. The same trend holds for the average over all experiments (data not shown), indicating that the intuitive interpretation of a speckle forming because of polymerization and dissolving because of depolymerization does not apply to dense polymer networks.

Given the percentages above we would, however, expect that the majority of all speckles still follow the intuitive case of speckles appearing due to polymerization and disappearing due to depolymerization ($68\% \times 75\% = 51\%$). Evidently, we can perform this statistics only on speckles with both a statically significant and thus classifiable birth and a statistically significant death event. Fig. 4-8 includes statistics of all significant events, independent of whether a significant birth is paired with a significant death. Interestingly, the fraction of speckles with birth due to polymerization and death due to depolymerization amounts to $63.54 \pm 6.71\%$ (Table 4-4), significantly higher than our expectation. Speckles which appear with a significant polymerization event have a higher probability to disappear with a significant depolymerization event. We do not have a conclusive explanation for this behavior, but suspect that the modes of appearance and disappearance contain relevant information of the underlying network structure. We defer to a future report for a detailed examination of this potentially valuable property of the speckle signal.

		Death	
		Polymerization	Depolymerization
Birth	Polymerization	$13.06 \pm 2.18\%$	$63.54 \pm 6.71\%$
	Depolymerization	$5.79 \pm 2.08\%$	$17.62 \pm 3.04\%$

Table 4-4

Distribution of speckles in four classes, calculated for experiments *MI-M3*. The classes are defined by the pairwise combinations of birth and death due to polymerization and depolymerization, respectively.

We performed the same analysis on movie *CI*, including a study of the possible changes of these numbers, when considering primary speckles only as compared to all speckles (Table 4-5). We did not find any significant changes to the previous statistics, suggesting that neither the type of network, moving or stationary, nor the order of speckles have an influence on this behavior.

		Death	
		Polymerization	Depolymerization
Birth	Polymerization	(a) 9.66%	(a) 67.85%
		(b) 10.30%	(b) 69.35%
	9.98 ± 0.45 %	68.60 ± 1.06 %	
	Depolymerization	(a) 5.86%	(a) 16.63%
(b) 4.06%		(b) 16.29%	
		4.96 ± 1.27 %	16.46 ± 0.24 %

Table 4-5

Distribution of speckles in the same class assignment as Table 3, calculated for experiment *CI*. (a) Primary speckles, no hierarchical tracking; (b) third-order speckles, no hierarchical tracking. The hierarchical tracker does not change the result (not shown).

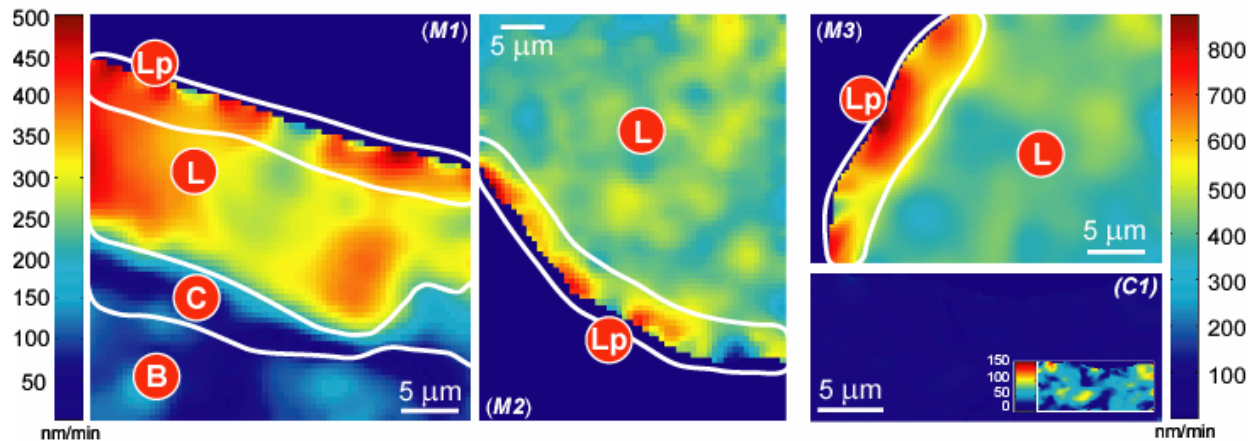
The mean lifetime of a speckle appearing due to polymerization and disappearing due to depolymerization should represent the actual lifetime of the actin filaments within the speckle volume. Interestingly, the lifetimes of all four speckle classes are similar (Table 4-6).

	Total	BP and DD	BP and DP	BD and DP	BD and DD
<i>CI</i>	46.54 s	48.01 s	41.07 s	40.97 s	44.96 s
<i>M1</i>	70.03 s	70.57 s	71.51 s	60.36 s	71.40 s
<i>M2</i>	66.54 s	66.07 s	70.32 s	56.98 s	68.81 s
<i>M3</i>	78.48 s	79.48 s	76.20 s	63.05 s	80.36 s

Table 4-6

Mean speckle lifetimes listed separately for the four classes of speckles. *BP*: birth due to (speckle) polymerization; *BD*: birth due to (background) depolymerization; *DP*: death due to (background) polymerization; *DD*: death due to (speckle) depolymerization.

There seems to be no exception in the interpretation of lifetimes for a speckle that appears due to polymerization and disappears due to depolymerization. Nevertheless, we focused on this class and calculated, where possible, the mean speckle lifetime in the lamellipodium (*Lp*), lamellum (*L*), cell body (*B*), and iv) convergence zone. Fig. 4-9 reveals the kinematically distinct characteristics of these zones in maps of flow speed. The maps were extracted as the magnitude from vectorial velocity maps (not shown), averaged over three consecutive time points. Animated velocity and speed maps are provided as supplementary data. The maps indicate that lamellipodium retrograde flow is consistently faster than lamellum flow, with a more prominent gradient found in *M2* and *M3*. In *M1* we also resolve the convergence zone and cell body, where velocities drop below 150 nm, similar to the velocities obtained for the cortical F-actin in *CI*.


Figure 4-9

Speed maps for the movies *M1-M3* (motile cells), and *C1* (contact-inhibited cell). Animated versions of these maps are provided as supplementary data. Lamellipodium (*Lp*) and lamellum (*L*) are separated by a significant speed gradient. Cell body (*B*) and lamellum are separated by the convergence zone (*C*), where flow halts completely. The maps for *M3* and *C1* are represented on the same color scale for direct comparison. Stretching of the color scale (inset *C1*) reveals unorganized residual flow in contact-inhibited cells.

	Lamellipodium	Lamellum	Convergence zone	Cell body
<i>M1</i>	68.14 s	80.13 s	65.13 s	59.48 s
<i>M2</i>	51.22 s	71.79 s	—	—
<i>M3</i>	50.82 s	88.65 s	—	—

Table 4-7

Mean speckle lifetimes in different regions of the protruding edge (where applicable).

Table 4-7 summarizes the speckle lifetimes associated with these zones. Consistently, we found an increase of lifetime from lamellipodium to lamellum. The changes are more dramatic for experiments *M2* and *M3*, in accord with the more prominent speed gradients in these movies. In *M1* we additionally measured the lifetime in the convergence zone and cell body. Compared to the lamellum, the convergence zone has again a significantly shorter lifetime. The shortest lifetime is found in the cell body, where we observed the least kinematic activity. This agrees with our finding that speckles in contact-inhibited cells have a significantly shorter lifetime than in any area of migrating cells (see Table 4-6). We conclude that the more stationary a network is in space, the more active it is in terms of turnover.

Graded velocities and lifetimes are illustrated in Fig. 4-10 for movie *M1*. Panel (a) displays the flow velocity map interpolated on a regular grid of $0.7 \mu\text{m} \times 0.7 \mu\text{m}$. Speckle displacements of 3 consecutive frames of the movie were integrated.

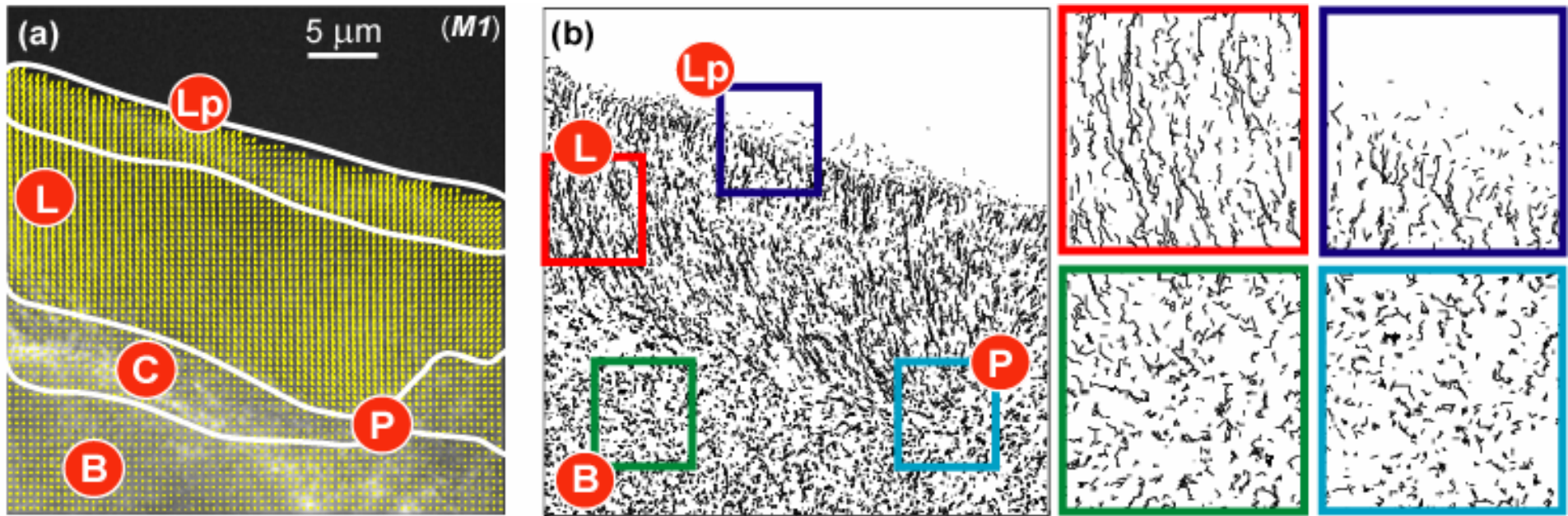


Figure 4-10

Velocity map of F-actin flow for *MI*. (a) Flow interpolated on a regular grid of $0.7 \times 0.7 \mu\text{m}$ from speckle trajectories over 3 consecutive frames. Lamellipodium (*Lp*) and lamellum (*L*) exhibit retrograde flow. The anterograde flow of the cell body (*B*) and retrograde flow of the lamellum meet in the convergence zone (*C*). In this movie, the convergence zone contains a peculiar pole (*P*) in the flow field. (b) Complete trajectories for speckles born in the first 20 frames of the movie. Sample windows are enlarged to indicate differences between the zones in terms of lifetime and trajectory coherence.

In panel (b), we accumulate all speckle trajectories starting with a speckle birth event in the first 20 frames of the time-lapse series and show enlargements of regions in the lamellipodium, lamellum, and cell body. We also plot the trajectories for a peculiar region in the convergence zone where the network converges from all sides towards one pole. In agreement with Table 4-7, the lamellum exhibits long, straight, and almost parallel trajectories, suggesting high stability of the underlying network. All the other regions contain clearly shorter trajectories, with a remarkable difference in terms of the degree of flow coherence between the lamellipodium and the two other windows in the cell body and convergence zone.

4.4.9 The flow organization is replicated by four zones of different turnover

The analysis of the spatial distribution of speckle lifetime projects a putative relationship between the kinematics of F-actin flow and the turnover. We now have for the first time the tool to investigate the coupling of these two parameters of F-actin dynamics. In this paper we focus on presenting the co-organization of time-resolved flow and turnover and defer the quantitative study of the molecular origins of this relationship to a separate paper currently in preparation. Fig. 4-11 displays turnover maps of all movies analyzed for this paper as a two channel color overlay (red channel for polymerization, green for depolymerization). For static mapping we integrated the scores over the entire frame sequence of a movie. Time-resolved, animated maps are provided for **M2** as supplementary data, indicating that the F-actin turnover is not a steady-state process.

The static maps are sufficient to indicate the clear match between the spatial organizations of flow (Fig. 4-9) and turnover. For the migrating cells, all maps reveal spatially confined, high polymerization at the very leading edge of the cell (arrowheads in **M1 - 3**). Over a distance as short as 1 μm , polymerization converts into a band of strong depolymerization. The border of the band (arrow) colocalizes with the maximum of the speed gradient of retrograde flow characterizing the junction of lamellipodium and lamellum. We conclude that the actin network undergoes a major modification both in terms of kinetics and kinematics when entering from the lamellipodium into the lamellum.

We have measured several profiles at different locations and found that $83.20 \pm 8.75\%$ ($n = 6$ profiles) of the F-actin polymerized at the leading edge is disassembled still in the lamellipodium. This disassembly would therefore maintain a high concentration of G-actin subunits which diffuse only over short distances before getting re-incorporated into the network (treadmilling). This view is consistent with recent findings by Cramer (1999);

Fischer *et al.* (2003); Pantaloni *et al.* (2001), who suggested depolymerization being the rate limiting step of lamellipodial protrusion. Fast treadmilling seems also to agree with the nucleation-dendritic model (Pollard *et al.*, 2000; Mogilner and Edelstein-Keshet, 2002), which requires a constant and large pool of free actin monomers close to the actively polymerizing barbed ends.

A second area of strong disassembly is located in the contraction zone, where we suspect high myosin activity. It will take a series of additional experiments where our mapping techniques will be combined with pharmacological manipulation of F-actin to examine whether depolymerization is the result of network contraction, or whether contraction is promoted in areas of strong network disassembly where the network stiffness might be reduced.

Turnover in the lamellum and cell body is characterized by cycles of assembly and disassembly in a dynamic equilibrium (see animated maps provided as supplementary data). In the static maps the dynamics of the equilibrium appears as a random distribution of patches with preferential polymerization or depolymerization.

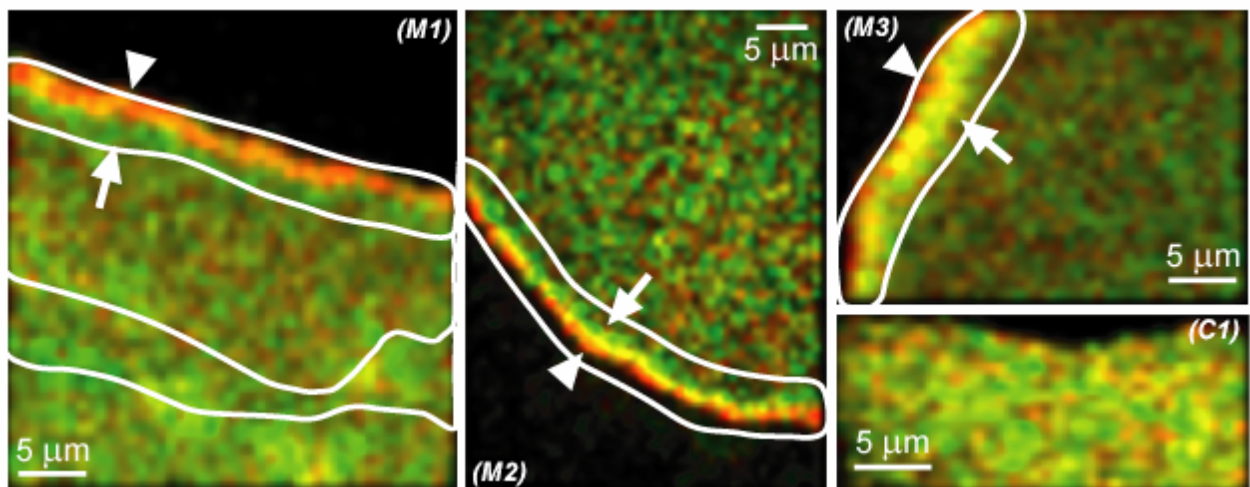


Figure 4-11

F-actin turnover represented by two-channel color maps (red: polymerization, green: depolymerization) for the four experiments *M1-M3* and *C1*. The organization of these maps matches the organization of the speed maps in Fig. 4-9. Highly confined polymerization in the lamellipodium next to the cell membrane (arrowheads in *M1*, *M2* and *M3*) is followed by a belt of depolymerization at the lamellipodium-lamellum junction (arrows). Strong depolymerization is also present in the convergence zone. Lamellum and cell body exhibit a dynamic equilibrium of network assembly and disassembly, similar to the one of cortical networks in contact-inhibited cells (*C1*).

4.4.10 Lamellum turnover reveals peak frequencies in the power spectrum similar to those of turnover of cortical F-actin of contact-inhibited cells

The kinetic organization in the lamellum region closely resembles the map of cortical F-actin turnover in contact-inhibited cells (Fig. 4-11, *CI*). This suggests that the two network types are regulated by similar molecular mechanisms, distinct from those underlying network turnover in lamellipodium and convergence zone. To test if turnover in lamellum and cortex network are indeed comparable, we calculated power spectra in the lamellum of *M2* and the network in *CI*, as we did in Chapter 2. To apply the required Fourier analysis, we first had to sample average kinetic scores in windows moving with the retrograde flow field (Fig. 4-12a).

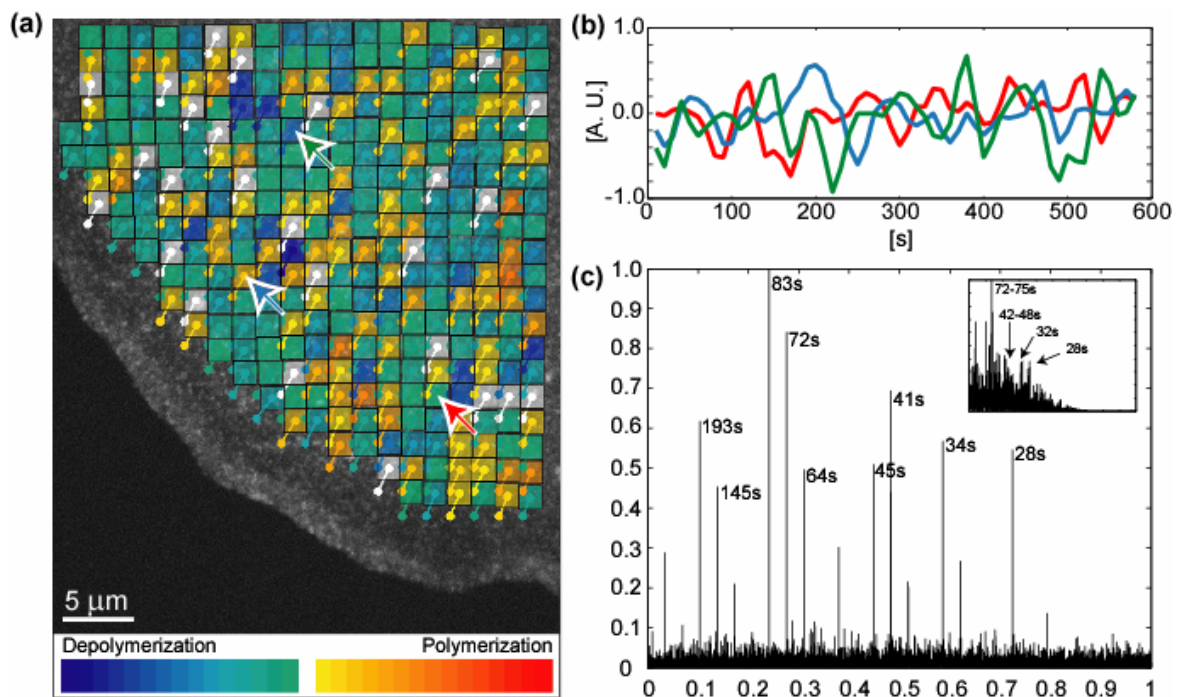


Figure 4-12

Comparison of F-actin turnover in the lamellum of a motile cell and in the cortex of a contact-inhibited cell. (a) In the lamellum, the analysis of kinetic scores in a time series has to be performed in windows moving with the average flow of the network. Windows are drawn in their final location, with a short connector indicating the window displacement between first and last frame. Window colors represent the net turnover over 600 s (color codes are defined by the color bar). (b) Time series of kinetic scores for three sample windows (arrows in (a) match with the line color). They reveal cyclic turnover with a remarkably constant period between the series. (c) Power spectrum integrated over all windows in (a) with peak frequencies in good agreement with those of cortical actin in contact-inhibited cells (inset).

Fig. 4-12b displays the time series of average kinetic scores for three arbitrary sample windows in the lamellum of the cell in *M2*. Two of them (red and green) have a negative integral over the entire 600 s of the movie, reflecting net disassembly of the corresponding network patch. The net turnover of each analyzed window is color-coded in Fig. 4-12a, ranging from dark blue for strong depolymerization to dark red for polymerization. Independent of net turnover, the three windows undergo cycles with a remarkably stable frequency. Fig. 4-12c displays the combined power spectrum of all windows plotted in panel Fig. 4-12a. Peak frequencies are located at 83 s, 72 s, 64 s, 45 s, 41 s, 34 s, and 28 s in close agreement with the peak frequencies (72 – 75 s, 42 – 48 s, 32 s, and 28 s) measured in cortical F-actin (Fig. 4-12c inset). This supports the hypothesis that the same reaction-diffusion mechanisms of actin-binding proteins may regulate the dynamic equilibrium of network turnover in lamellum and cortical actin networks. The two power spectra, however, match less for the low frequency peaks. This holds particularly true for the DC value, which is absent for cortical F-actin but is significant for the lamella in migrating cells because of the overall disassembly of the network. Differences in the noise level of the power spectra are mainly due to the larger number of sample windows included in the analysis of movie *M2* as compared to movie *C1*.

4.5 Conclusion

We report critical extensions of the computational framework for FSM data analysis introduced in Chapter 2, which permits us now to simultaneously map F-actin turnover and flow in cytoskeletal networks with a broad range of dynamics. Three additional algorithms were necessary to achieve this goal: i) hierarchical speckle extraction allowing the detection and localization of speckles with signal interference to neighboring speckles; ii) hierarchical tracking based on iterative flow propagation to reduce ambiguity in the assignment of corresponding speckles in consecutive frames; iii) adaptive flow filtering preserving significant flow gradients while reducing the random jitter in the trajectories of single speckles. To demonstrate the importance of these algorithms for the reconstruction of complete speckle trajectories we presented extensive statistics of the influence of each processing step on the number of speckles, their lifetime, birth and death distribution, as well as the generation of F-actin flow and turnover maps. Also, these data reconfirmed that speckle appearance and disappearance in a polymer network such as the F-actin cytoskeleton relate only indirectly to network assembly and disassembly. To exploit speckles as local reporters of polymer turnover in the manner we suggested in Chapter 2, we require faithful trajectories

from birth to death. Because of the improved tracking performance we are now able to satisfy this requirement and present for the first time maps of the kinematic and kinetic organization of F-actin networks at equal resolution.

There are several reasons why we are confident in the kinetic maps reflecting true molecular events: i) the software does not rely on organizational models of turnover, but is restricted to independent statistical processing of each speckle. The fact that the program returns maps with high spatial organization demonstrates the robustness of the underlying stochastic models; ii) the stochastic models are designed conservatively to exclude signal artifacts. A kinetic score is accepted only if there is twofold evidence that a speckle birth or death event reflects true monomer exchange. First, intensity changes in the speckle and surrounding background have to be significant relative to noise-induced signal variation (Chapter 2). Second, not only foreground and background *per se* have to be significant, but the changes have to be mutually consistent. We test the divergence (for speckle birth) and convergence (for speckle death) of $d(\Delta I)/dt = dI_{\text{speckle}}/dt - dI_{\text{background}}/dt$ for significance with respect to its uncertainty. Events showing a strong intensity change in, e.g. the speckle foreground, but a similarly strong change also in the background are discarded as unclassifiable. In total, approximately 35 - 55 % of all speckle events are accepted as a significant signal of local monomer exchange; iii) the maps confirm well-characterized properties of F-actin dynamics, including retrograde flow and high polymerization activity at the leading edge of migrating cells and the break down of flow under contact-inhibition. This provides confidence in new dynamic properties revealed as a consequence of the enhanced algorithmic framework.

A first finding uncovered by the new maps is that lamellipodium and lamellum networks may be kinetically and kinematically distinct cytoskeletal structures. Because of the high spatial resolution of the mapping, we were able to extract turnover gradients that reflect coexistence of network assembly and disassembly in the lamellipodium over distances as short as 1 μm . The same holds true for velocity gradients in the flow field. This result will have major implications on our understanding of the function and coordinated action of lamellipodium and lamellum in guiding cell migration. We will now apply our tools in combination with pharmacological intervention to tease apart the molecular relationships between these two cytoskeleton parts. Importantly, future work will also be directed towards testing these new tools on other cytoskeletal polymer assemblies.

4.6 Acknowledgments

Funded by Human Frontiers Science Program Young Investigator award RGY5-2002 to C.M.W.-S. and G.D. and National Institutes of Health grant R01 GM67230 to C.M.W.-S and G.D. (subcontract).

5

Quantitative Fluorescent Speckle Microscopy Analysis of the Dynamic Coupling of Lamellipodial and Lamellar F-Actin Meshworks

5.1 Introduction

Fluorescent Speckle Microscopy (FSM) has matured to a highly quantitative technique for the analysis of cytoskeletal dynamics and turnover kinetics through the development of dedicated automated software (Chapter 2; Chapter 4). Hand tracking of only a few speckles has been employed, but is incredibly laborious, prone to error, and leaves the majority of information unexploited (Schafer *et al.*, 2002; Salmon *et al.*, 2002; Gupton *et al.*, 2002; Watanabe and Mitchison, 2002). In previous work, we implemented an algorithm for the fully automatic analysis of the turnover kinetics of the cortical actin meshwork of contact-inhibited newt lung epithelial cells (Chapter 2) and we subsequently enhanced it to perform the same analysis on motile cells (Chapter 4). With our algorithm we were able to obtain quantitative information with unprecedented spatial and temporal resolution for both the kinetic and kinematic characteristics of F-actin meshworks. First analyses suggested a peculiar organization of the leading edge of motile cells, and our software proved to deliver the resolution necessary to investigate the different organization of those different structures.

Fig. 5-1 sketches the structure of a motile newt-lung epithelial cell (see also Fig. 1 in Salmon *et al.*, 2002). The cell body (Cb) is the thickest region of cytoplasm containing the nucleus (Nu), and is separated from the lamellum by the so-called convergence zone (C), where a belt of myosin motors are responsible for the traction of the cell body during cell translocation. The convergence zone is therefore located where forward and rearward traction forces are likely to meet. In fact, speckle flow in FSM time-lapses is directed anterograde in the cell body and retrograde in the lamellum. The convergence zone appears to be a region of massive F-actin disassembly (Salmon *et al.*, 2002). In the cell body and tail (T), F-actin at the ventral cell surface forms bundles that may be contractile and mediate retraction of the cell rear (Cramer *et al.*, 1997). The lamellum (La) is a wide and thin structure where the F-actin meshwork gets pulled backwards towards the convergence zone. Close to the cell membrane, the lamellipodium (Lp) is a zone of high actin polymerization responsible for membrane protrusion and establishment of new contact sites with the underlying substratum. In fish epidermal keratocytes, the lamellum is completely absent, and the lamellipodium spans the whole leading edge, from the cell body to the cell membrane. Svitkina *et al.* (1997) proposed that in fish epidermal keratocytes the forward translocation of the cell body and retrograde flow in lamellipodia are both driven by contraction of an actin-myosin network in lamellipodial/cell body transition zone.

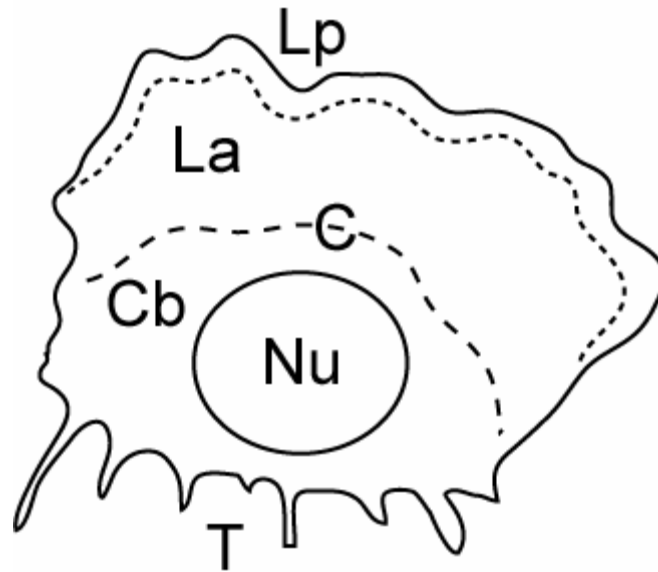


Figure 5-1

Structural organization of a motile newt lung epithelial cell. The thick cell body (Cb) contains the nucleus (Nu) and is separated by the lamellum (La) by the convergence zone (C). At the very leading edge, the lamellipodium (Lp) is responsible for membrane protrusion and establishment of new contact sites with the substratum. The traction forces generated primarily in the convergence zone cause the forward translocation of the cell body and tail (T).

Visual inspection of FSM time-lapse series of motile newt lung epithelial cells, reveals significantly higher signal density and speckle flow velocity in the lamellipodium with respect to the lamellum. In this work, we will exploit our algorithm for an in-depth analysis of the dynamic coupling of lamellipodial and lamellar actin meshworks in motile cells. The *material* coupling of the two regions can be assessed either as the fraction of the concentration of label (obtained from a spatial integration of the *kinetic scores*, see Chapter 2), which is transferred from the lamellipodium into the lamellum or as the fraction of all individual speckles generated in the lamellipodium which cross the transition between the lamellipodium and the lamellum and disappear in the lamellum. Furthermore, the analysis of the time evolution of retrograde speed velocities in the lamellipodium and lamellum can give a measure of the *mechanical* coupling of these two regions. Their interdependence can also be assessed by means of perturbation experiments, where their stability is affected by short perfusions with drugs.

5.2 Results and discussion

5.2.1 Material coupling

The scores returned by our kinetic analysis (Chapter 2) are an unbiased measure for the average local addition and removal of labeled monomers over time. The spatial integral of such a kinetic map is therefore a measure for the local concentration of label (and, indirectly, of total F-actin). Fig. 5-2 (a) shows the kinetic map calculated for a motile newt lung epithelial cell imaged during a wound-healing experiment in culture. The red and green channels depict the total polymerization and depolymerization over 600s, respectively. It is evident how the kinetic organization of lamellipodium and lamellum are distinct. In the lamellipodium, the strong, concentrated polymerization belt at the very leading edge is immediately followed by a region of depolymerization with comparable strength. In contrast, throughout the whole lamellum, weak polymerization and depolymerization spots seem to alternate rather regularly.

Visual inspection of FSM movies of motile cells shows very clearly, without the need for any computational analysis, that the lamellipodium has on average much higher signal intensity than the lamellum and furthermore that speckles in the lamellipodium flow faster than those in the lamellum. Our finding, that the F-actin meshwork seems to be at least partially disassembled before the transition into the lamellum (Chapter 4), is another hint that these two regions are distinct entities. We analyzed therefore what is the fraction of label incorporated into the actin meshwork at the cell membrane which is disassembled and fails to enter the lamellum. The boxes in Fig. 5-2 (b) show three analyzed regions of the kinetic map, with their axis x perpendicular to the local cell membrane. These regions are reported in Fig. 5-2 (c), (d) and (e). The underlying graphs show the three rates of polymerization (dC^p , red), depolymerization (dC^d , blue), and change ($dC^c = dC^p + dC^d$, green) in arbitrary units. From these graphs, it is clear that the lamellipodium displays a much stronger kinetic activity than the lamellum. Furthermore, the peak in polymerization (dashed red line, corresponding to the maximum in the dC^p curve) clearly precedes the peak in depolymerization (dashed blue line, at the minimum of dC^d) when moving away from the leading edge. We define mathematically the transition between the lamellipodium and lamellum as the position x where there is the second root of the change rate dC^c (dashed green line). The fraction F of material which is disassembled in the lamellipodium is calculated as the ratio:

$$F = \frac{\int_0^{x_i} dC^p dx}{\left| \int_0^{x_i} dC^d dx \right|}.$$

This value accounts to 83.67% for the region in Fig. 5-2 (c), to 86.50% for (d), and 74.63% for (e). Analysis from several other movies (not shown) revealed that on average, $83.20 \pm 8.75\%$ of the material which is assembled at the leading edge is disassembled before the transition with the lamellum. Our hypothesis is that this strong disassembly of the F-actin meshwork in the lamellipodium maintains a pool of concentrated, free G-actin monomers in the lamellipodium, minimizing the distance over which monomers must diffuse before reincorporation at the leading edge. This provides the cell with an efficient control mechanism for fast lamellipodial protrusion.

The integral of the change rate, $\int_0^L dC^c dx$, is the label concentration $C(x)$, and is represented by a yellow curve overlaid to the three boxes in Fig. 5-2 (c), (d), and (e). The interesting observation here is that the lamellum, although gently, depolymerizes more and more with increasing distance from the leading edge. The fact that the value for $C(x)$ becomes negative in this representation for large values of x implies that at the leading edge the concentration $C(x=0)$ of F-actin must be larger than zero, suggesting that polymerization adds material on top of an already existing meshwork. A possible interpretation might be that this meshwork extends from the lamellum into the lamellipodium and up to the cell membrane; the lamellipodium is thus a transient, thin meshwork which is locally assembled and disassembled on top of the lamellar F-actin meshwork with the purpose of membrane protrusion or ruffling. Our kinetic analysis returns a measure for the *relative change* in actin concentration, but cannot return an absolute value for the concentration itself. To obtain this offset, one has to measure the actual F-actin concentration or calibrate the FSM signal in terms of the number of labeled fluorophores which contribute a given intensity in the image.

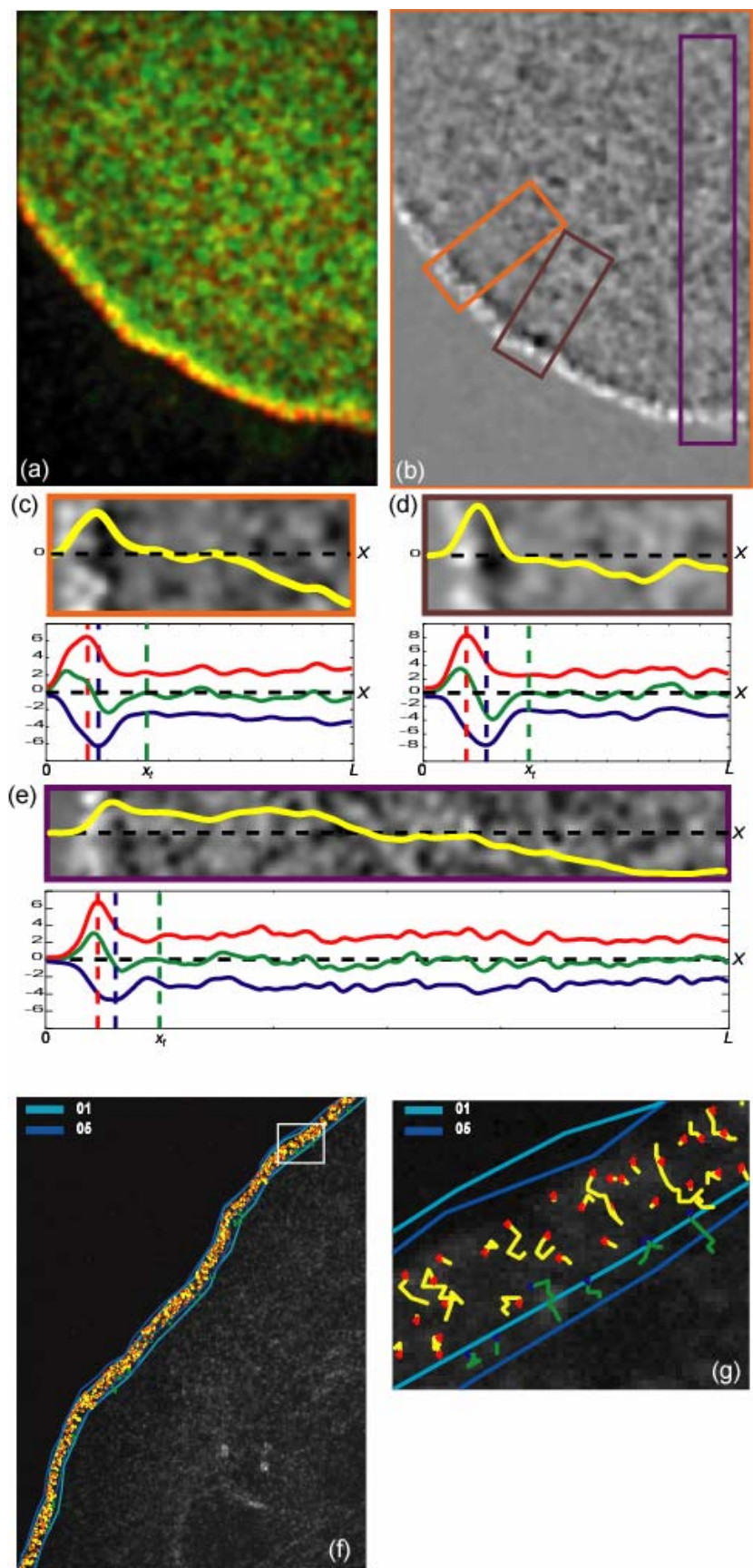


Figure 5-2

Material coupling between the lamellipodium and the lamellum. (a) Kinetic map of a motile new lung epithelial cells. The maps for total polymerization and depolymerization are shown as the red and green channels of the same map, respectively, for easier localization. (b) The change map, which reflects the net label production over time is the sum of the channels of (a). Integration of the change map along an axis x perpendicular to the cell leading edge is a measure for the material being transported away from the cell membrane. The yellow, brown and purple regions are analyzed in (c), (d), and (e) respectively. The red, blue, and green lines in the graphs of (c), (d), and (e) are the polymerization, depolymerization and change rate, respectively. The yellow lines overlaid to the extracted image regions of interest correspond to the spatial integral of the change rate. (f) An alternative approach to assess the material coupling between the lamellipodium and the lamellum is to determine the fraction of speckles born in the lamellipodium which escape depolymerization and enter the lamellum. (g) Zoom up of the boxed portion of the leading edge from (f). See text for all the details.

Another way to test how much of the material flows from the lamellipodium into the lamellum is to consider individual speckles which were born in the lamellipodium and check how many of them enter the lamellum. In analogy, to what seen before, only 8.53 ± 1.97 % of all speckles leave the lamellipodium ($n = 3$ experiments). This confirms the previous result that most of the F-actin which is polymerized at the leading edge (thus resulting in the formation of speckles) does not survive the depolymerization phase (which cause their disappearance). Fig. 5-2 (f) shows the result of this analysis performed on a motile newt lung cell. The boxed region is zoomed up in Fig. 5-2 (g), and shows a few speckles (green trajectories starting from a blue dot) which were born in the lamellipodium in either one of frames 1 to 4 (only the lamellipodium boundaries from frame 1 are shown in dark blue) and end their lives in the lamellum in frame 5 or later (the light blue line delimits the lamellipodium in frame 5). Notice how the lamellipodium-to-lamellum transition moves away from the cell body in the direction of cell protrusion along with the leading edge. Most of the speckles (yellow trajectories starting from red dots) appear and disappear in the lamellipodium and never reach the boundary with the lamellum.

To further assess the distinct nature of the F-actin meshwork in the lamellipodium with respect to the lamellum, we analyzed the mean speckle lifetimes from several FSM time-lapses of motile newt lung epithelial cells. On average, the mean lifetime of speckles in the lamellipodium is 44.07 ± 28.62 % shorter than in the lamellum (for a deeper analysis, see Chapter 4).

5.2.2 Mechanical coupling

Analysis of the mean retrograde flow velocity over time in the lamellipodium of motile cells revealed an oscillating behavior with a rather constant period. For the cell of Fig.

5-3 (a), the velocity oscillations in the lamellipodium (red region) span a large interval, from 400 to more than 800 nm/min with a period of about 75 to 100 s. Other cells showed similar behaviors with slightly different periods and velocity ranges. These differences might be due to both differences in the actual cellular parameters as well as to the quality of FSM data, since averaging noisy data can result in the damping of the values of interest. Interestingly, the analysis of the flow in two regions of the lamellum at increasing distances from the leading edge (green and cyan regions, respectively) revealed as well velocity oscillations in the range 400 to 600 nm/min which were in good phase agreement with the oscillations in the lamellipodium (Fig. 5-3 (b)). Therefore, although the lamellipodium and lamellum appear to be uncoupled with respect to their retrograde flow velocities, these results suggest the existence of some mechanical coupling which propagates from the lamellipodium into the lamellum or vice versa. The velocity in the lamellum seems to be independent of the distance from the leading edge. Notice the steady, slight acceleration of the lamellar velocities accompanied with an increased amplitude in the lamellipodial velocity oscillations.

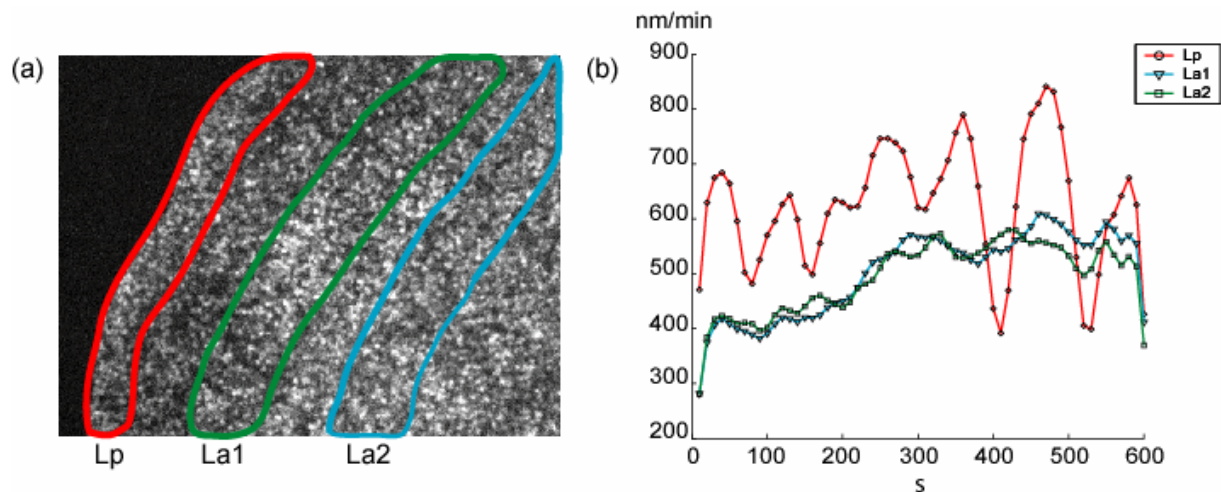


Figure 5.3

Analysis of the retrograde flow velocities in three distinct zones of leading edge of a newt lung epithelial cell. (a) The lamellipodium (red region labeled with Lp) and two areas in the lamellum (La1, green) and (La2, cyan) at increasing distances from the leading edge are analyzed for their velocity evolution over time. (b) All velocities oscillate over time with rather constant period and in good phase with each other, suggesting that the lamellipodium and lamellum might be mechanically coupled.

5.2.3 Perturbation experiments

Jasplakinolide is a naturally occurring cyclic peptide from the marine sponge *Jaspis johnstoni*, which has both fungicidal and antiproliferative activity. It exerts its cytotoxic effect

in vivo by stabilizing pre-existing actin filaments. Blebbistatin is a non-muscle myosin II ATPase activity inhibitor (Straight *et al.*, 2003). We perfused motile newt-lung epithelial cells with either 1 μ M jasplakinolide or 100 μ M blebbistatin to test possible effects these drugs would have on the lamellipodial and lamellar organization. Fig. 5-4 summarizes the results from the two experiments. For both the experiments, the retrograde flow behavior was quantified as well as the kinetic organization. For every experiment we analyzed the cells before perfusion as control.

5.2.3.1 Jasplakinolide

The lamellipodium of motile newt lung epithelial cells is characterized by a higher retrograde flow velocity than in the lamellum and by high polymerization activity immediately followed by depolymerization with similar strength. Perfusion with 1 μ M jasplakinolide causes the rapid disassembly of the lamellipodium which collapses onto the lamellum (red arrows in Fig. 5-4 (a)). After the lamellipodium has disappeared, the cell front does not move any more, confirming that cell protrusion is mediated completely by the lamellipodium. Along with the lamellipodium, the region of higher velocity disappears as well, as evident in Fig. 5-4 (b). Interestingly, the retrograde flow slows down in the lamellum as well. After perfusion, the total polymerization in the lamellum decreases by 13% while the total depolymerization sinks more, by 23%, in agreement with the stabilizing effect of jasplakinolide on existing filaments, which causes as well a 10.4% increase in the mean speckle lifetime in the lamellum, from 69.03 to 76.21 s. More stable, longer-living filaments might explain the reduction of lamellar flow.

5.2.3.2 Blebbistatin

Blebbistatin is a myosin II ATPase activity inhibitor, therefore its effect on the cell should be a decrease in the mean lamellar retrograde flow. In fact, the mean lamellar velocity is reduced from 59.9 ± 16.6 nm/min before perfusion to 26.1 ± 11.2 nm/min (-56.4%). Because the retrograde flow in the lamellipodium is polymerization-driven, the inhibition of myosin II should not have any direct effect on the lamellipodial flow. Still, the flow in the lamellipodium goes from 122.5 ± 17.7 nm/min to 146.7 ± 30.3 nm/min (+19.8%). However, this might be the consequence of the averaging of velocities over a region, which moves slower after perfusion. In fact, the velocity of cell protrusion drops by about 32% from 220 to 150 nm/min. This effect can be indirectly seen in the total kinetic activity of Fig. 5-4 (c). Both the polymerization and depolymerization belts are thinner and more concentrated, because of

the shorter distance traveled by the lamellipodium in the right panel. However, with respect to control the total polymerization in the lamellipodium after perfusion drops by 47% whereas depolymerization gets reduced by 41%. In contrast, polymerization and depolymerization in the lamellum decrease only by 9 and 8%, respectively. Therefore, the inhibition of myosin causes a reduction in the lamellar flow as expected, but also a reduction in the turnover kinetic in the lamellipodium. The mean speckle lifetime in the lamellipodium decreases 11% and in the lamellum 23%.

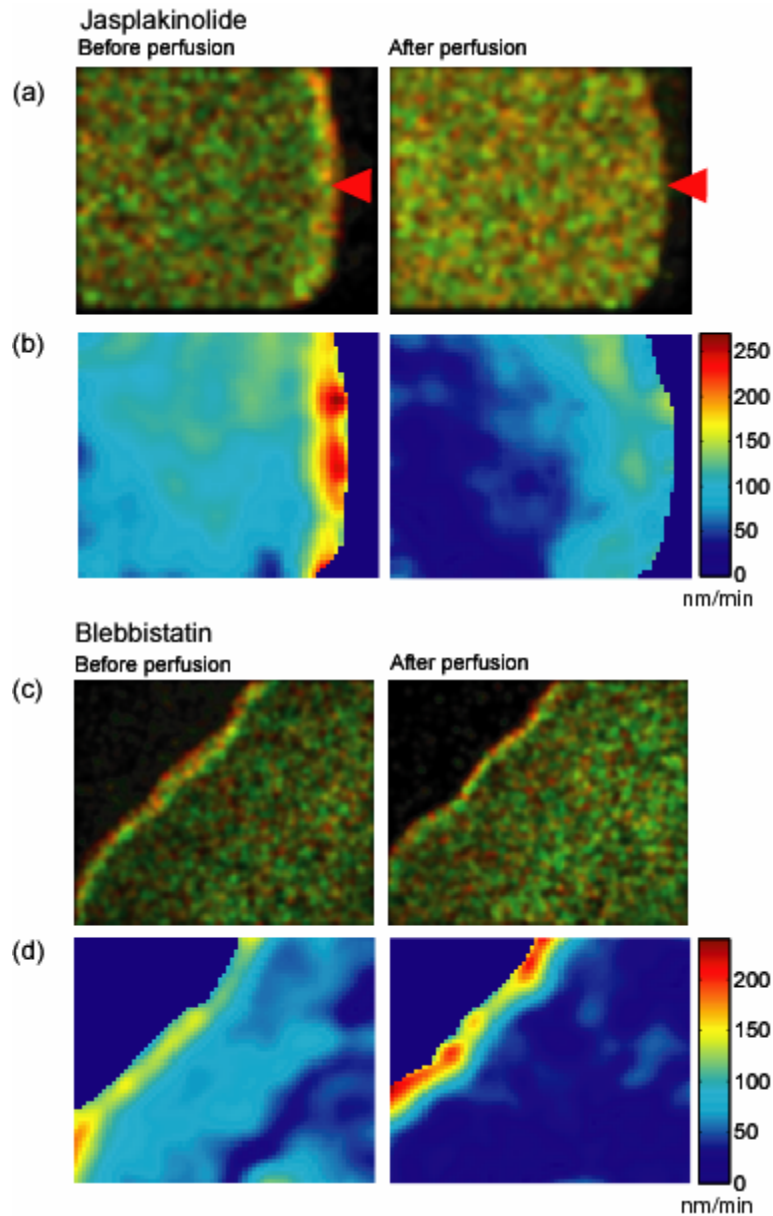


Figure 5-4

Effects of external perturbations on the organization of the lamellipodium and lamellum in motile newt lung epithelial cells. Cells were perfused with jasplakinolide ((a) and (b)) and blebbistatin ((c) and (d)) and their effect on the kinetic activity ((a) and (c)) and actin meshwork retrograde flow behavior ((b) and (d)) were examined.

See text for details. The arrowhead indicated the collapse of the lamellipodium after perfusion with jasplakinolide.

5.3 Conclusion

The lamellipodium and lamellum in motile newt lung epithelial cells appear to be to a high extent uncoupled structures. They show different retrograde flow behaviors with the lamellipodium exhibiting much higher velocities than the lamellum. This is known to be a consequence of two different mechanisms for flow generation, namely the force generated by actin polymerization against the cell membrane in the lamellipodium, and the traction of myosin motors in the convergence zone which pulls actin filaments in the lamellum. They show as well a highly different kinetic organization. The lamellipodium actively polymerizes and depolymerizes its actin filaments at high rates to maintain a large pool for free actin monomers close to the membrane and thus assuring the maintenance of a responsive machinery for protrusion and membrane ruffling. In contrast, the lamellum exhibits a dynamic net steady state obtained by alternation of moderate levels of depolymerization and polymerization, in a way similar to what we observed in the cortical actin of contact-inhibited cells.

Although differently regulated and possibly highly uncoupled, the lamellipodium and lamellum show however some possible interactions. For instance, oscillations in the retrograde flow velocities in the lamellipodium propagate to the lamellum. Furthermore, the application of blebbistatin, a myosin II inhibitor, strongly reduces the turnover activity in the lamellipodium possibly as a response to the reduced traction exerted on the lamellum.

6

Conclusion

6.1 Summary

During the three years of my thesis, I developed a first, stable version of a software package for the automated analysis of Fluorescent Speckle Microscopy data. This work was motivated by the frustration generated by the huge limitations of the previous analysis methods, such as hand tracking and kymograph analysis (Waterman-Storer *et al.*, 1998, 1999, 2000a; Kapoor and Mitchison, 2001; Schafer *et al.*, 2002; Salmon *et al.*, 2002; Gupton *et al.*, 2002; Watanabe and Mitchison, 2002; Brust-Mascher and Scholey, 2002). FSM movies contain a considerable amount of quantitative information – simply too much to be really exploited without fully automated computational tools. Even though some quantitative information can be extracted even with simple hand tracking, like partial velocity estimations, for more complex analyses, like the kinetic analysis presented in full detail in chapter 2, computational tools are mandatory. Because of the stochastic nature of speckles, any measurement must rely on statistical processing – based on mathematical models of the expected variations in speckle intensity and position over time – and subsequent spatial and temporal averaging of *large* numbers of speckles (see chapters 2 and 4). The more speckles can be extracted and fully characterized from appearance to disappearance in time-lapse series, the higher the resolution of the analysis and the confidence on the obtained result. Therefore, the result of a few hand-tracked speckles cannot simply be trusted if not under extraordinary circumstances.

Newt lung epithelial cells imaged during a wound-healing assay (Waterman-Storer *et al.*, 2000a) in culture were the cell system chosen to develop, test, debug, and tune the software. The main advantage assured by these cells was that depending on where they are located in the wounded epithelium (namely at the periphery or somewhere in the center), they show one of two possible configurations of their actin-based machinery for motility. Cells at the periphery of the cell monolayer are supposed to try and close the wound, and therefore they display all characteristics of a motile cell, with a ruffling and protruding lamellipodium, and an obvious retrograde flow of the F-actin meshwork which starts at the leading edge and reaches the zone of transition to the cell body. In contrast, cells embedded within the cell monolayer completely turn off their retrograde flow. Still, visual inspection of the FSM image sequences of these contact-inhibited cells clearly showed a strong photometric activity, indicating that although the cells were stationary, F-actin was undergoing steady turnover.

6.1.1 Summary of Chapter 2

Contact-inhibited cells were therefore the optimal starting point for the development of a kinetic analysis module where speckle kinematics could be almost completely neglected. Minor micro-movements due to Brownian motion, meshwork contractions, label addition or noise could be optimally addressed with a very simple nearest-neighbor tracker.

The kinetic module maps the assembly and disassembly of the F-actin meshwork by considering speckle appearances and disappearances as markers for polymer assembly and disassembly. Intensity changes at the time points of speckle appearances and disappearances are on average proportional to the local addition or removal of labeled actin monomers. Careful statistical classification of speckle births and deaths assign *scores* to these events, and their subsequent spatial and temporal averaging produces kinetic maps of the F-actin meshwork.

Our kinetic maps revealed for the first time a kinetic cycling of F-actin, where phases of polymerization alternate with depolymerization in a spatially coordinated fashion and with a period of ~40s. Similar reaction-diffusion waves (Vicker, 1999) or other cyclic behaviors of the F-actin meshwork (Ballestrem *et al.*, 2000) had already been reported in the literature.

Analysis of cells treated with low doses of latrunculin A revealed that this drug changed these cycle rates and introduced disorder into the system. The software turned out to be very sensitive, suggesting a future evolution of the software for screening or diagnostic purposes.

With a series of controls, we proved the algorithm to be robust against intensity variations due to noise and photobleaching, and focus plane drifts.

6.1.2 Summary of Chapter 3

Our first software version had the drawback that it could only be applied to the analysis of non-flowing speckles due to the weakness of the simple nearest-neighbor tracker implementation. However, our search for alternative trackers was unsuccessful. Existing trackers, mainly region-based approaches, would miserably fail to robustly track speckles: correlation approaches get confused by the high variability of the signal from one frame to the next. Particle trackers were not able to cope with several thousands of particles per frame, showing very slow convergence (if any) and getting disorientated by the changing number of particles over time.

Therefore, we developed a brand new particle method based on ideas from operational research and graph theory. All credits for the idea to apply graph methods to speckle tracking are to be attributed to the first author of this work, Pascal Vallotton.

After an initial validation of the tracker on some benchmark tests like the well known “peas in a rotating dish”, we tested it on interesting and difficult biological problems. With the new tracker, we were able to track speckle movement at the leading edge of migrating newt lung epithelial cells, and to show different local meshwork organizations based on flow characteristics. More impressively, we were able to track anti-parallel flow of speckles along MTs in the (metaphase) mitotic spindles with replicated mitotic chromosomes assembled in meiotic *Xenopus* egg extracts and produce maps of MT poleward flux.

Unfortunately, this tracker was not robust enough to return complete speckle trajectories, and was therefore not applicable to our kinetic analysis.

6.1.3 Summary of Chapter 4

The graph-based tracker was replaced in this work by a new particle tracker for flow recovery, which was able to return complete sets of speckle trajectories. This tracker bases on an iterative propagation scheme which relies on the continuum-mechanical characteristics of the flow field to locally adapt the filtering strength. In addition, we addressed the problem of partial speckle fusions during low-pass filtering of FSM data by means of a hierarchical extraction scheme, thus highly increasing the resolution of our analysis even for the case of stationary meshworks.

The enhancements in resolution and quality of the analyses were statistically tested. The software proved to be ready to be applied for the kinetic and kinematic analysis of actin meshworks in motile cells. In this paper we concentrated on the validation of the software, and postponed to the next paper the more detailed studies of biologically relevant questions which could be now addressed. Still, we anticipated the potential of the new algorithm by showing our first results revealing different organization of the lamellipodium and lamellum at the leading edge of motile cells in terms of both filament turnover and retrograde flow.

6.1.4 Summary of Chapter 5

In this last paper, we deepened the analysis on the organization of the leading edge of migrating cells introduced in the previous work. By means of our high-resolution analysis, we observed that the lamellipodium and lamellum are both kinetically and kinematically independent structures. The expected high lamellipodial polymerization activity at the leading

edge, responsible for membrane protrusion, is almost completely compensated by a belt of depolymerization at the transition between lamellipodium and lamellum. We speculate that this almost complete disassembly of the F-actin meshwork maintains a pool of concentrated, free G-actin monomers in the lamellipodium, providing the cell with an efficient control mechanism for fast protrusion.

The fast retrograde flow in the lamellipodium display oscillating velocities, with a period in the range of 75-100 s. The slower lamellar retrograde flow shows similar waves, although much smaller in amplitude, in good phase agreement with those in the lamellipodium.

Perfusion with jasplakinolide and blebbistatin, drugs which affect filament stability and myosin II activity, respectively, revealed interesting combined effects in both the lamellipodium and lamellum.

All the mathematical details of the current algorithm for *Computational Fluorescence Microscopy (cFSM)* have been published as a complete reference for the interested reader who wants to reimplement the algorithm in part or in its entirety. Alternatively, the software will be made available for download upon request. The software was developed under MATLAB (The Mathworks, Nattick, MA) with some computationally expensive modules written in C/C++ and features a handy user interface and a vast set of tools for image handling, post-processing and visualization functions. It is a robust software, where much effort has been dedicated to exception handling, meant to be used by other people in other labs in an intuitive way, with great ease of use. It can be run on Microsoft Windows-based machines as well as Unix systems. Still, this represents only the nucleation site for the future development of a larger software platform, which will integrate more and better tools for the analysis of all those molecular processes which affect the cytoskeleton.

6.2 Outlook

The results we could achieve with our software and the fast development of FSM over the last few years, convinced us that cFSM has the potential to become the tool of choice to investigate cytoskeleton dynamics in various cellular processes. As development on both software and microscopy sides progresses, cFSM will mature into fully automated assays that could be applied to live-cell screens for toxins, chemicals, drugs and genes that affect cytoskeletal dynamics. Together with automated analysis regimes, cFSM has the potential to become a core tool in automated, cell-based molecular diagnostics in cases where variations

in cytoskeletal dynamics are a sensitive signal for the state of a disease or the activity of a molecular perturbant.

There are several ways to go for the near future. One of the first priorities will be the calibration of the FSM signal. Right now, our kinetic analysis can only return *relative turnover rates*, because we do not know yet the factor which links a change in 1 gray value in the FSM signal intensity to the number of labeled monomers actually added or removed from the polymer. Knowing this factor and the labeling ratio f , we would be able to calculate real monomer association and dissociation rates (Pollard, 1986).

An immediate enhancement of the software can be achieved by substituting the adaptive flow filtering described in chapter 4 with e.g. the method of *least-squares collocation* (LSC). The LSC method (Moritz, 1973) is a combination of least squares adjustment and least squares prediction and is most popular in the field of geodesy. In the model, the measured data consists of a systematic part known as trend, and a stochastic part. The basic idea of the collocation is to distinguish between two different stochastic quantities: a purely random quantity termed noise and another random quantity, the signal part. When the signal is overlaid to the trend the best approximation in a least-squares sense of the true data is obtained. A preliminary study of this method has been performed by a diploma student of mine, Luca Baldini, with excellent results: the method is capable of robust filtering of flow under SNR conditions below 1.

It is evident from simple considerations on the extremely complex organization and regulation of the actin cytoskeleton during motility (see Introduction), that one important future achievement must be the careful modeling of the systems we are interested in. What we can do at the moment is to perturb the cytoskeleton by means of drugs, or activate signaling pathways through external agonists (for instance, actin polymerization is initiated by growth factors, chemoattractants, extracellular matrix, and phagocytic particles, among others), or selectively target genes which encode proteins involved in the activity of interest. Analysis of the reactions of the cytoskeleton to such changes can help elucidating some of the mechanisms involved, therefore additional perturbation experiments should be performed and the palette of reactions carefully analyzed. The study of the long-term cellular adaptation to external (or internal) stresses can as well help deciphering regulation mechanisms.

Still, this kind of approach can be extremely time-consuming and prone to error. It is an universal rule that biological experiment have a high chance to be repeated. Apart from such stereotypical considerations, though, the coupling of experiments with mathematical models is the way to go. Experiments deliver the parameters needed for setting up a model of

the system of interest, which in turn allows better experiments to be planned by delivering the *prior knowledge* needed to prevent a simple trial-and-error approach. This generates a mutual feedback which renders the system more robust at every iterations and improves the fidelity of the model.

For the case of the actin meshwork, a 3D model of the filament network might be built, and as many as possible known players considered (for an incomplete list, see the Introduction). Parameters to be taken into account will include protein concentrations, association and dissociation rates, competitive behaviors, spatial organizations, filament branching organization, effects of signaling pathways. Once a model of the actin meshwork is set up, one can create synthetic FSM images or image sequences by setting a fraction of the G-actin to be fluorescently labeled and simulating the optics of a virtual microscope. The software can be run on the generated time-lapse series and the results from synthetic data can be compared to those from real cells. When the goodness of the model is assessed, one can perform *in-silico* perturbation experiments. One or more of the parameters are changed, or new parameters are added, and one characterizes quantitatively how the model reacts to the perturbation.

In addition, one could build *in-vitro* actin meshworks, and image them with FSM. In such a system, the labeling ratio can be easily defined. Furthermore, the concentration and identity of all the involved players are known. The link to the mathematical model would then be much easier. This would add a third layer to the *in silico* – *in vivo* system, and the comparison of results from perturbations *in vivo*, *in vitro*, and *in silico* would return even stronger evidence for the role of individual molecules.

FSM benefits from the fact that the principle can flexibly adapt to other types of existing fluorescent microscopy. Spinning disk confocal microscopy has replaced the initially used conventional wide-field epifluorescence light microscopy, and we have recently begun to explore the application of FSM to total internal reflection microscopy (TIRFM), which allows excitation of proteins within a region of 100- to 200-nm depth, thus significantly reducing the out-of-focus fluorescence.

Based on spinning disk imaging technology it will also be possible to extend FSM to 3D. Naturally, with 3D FSM acquisition the availability of analytical software will become imperative. Not only will the visualization of the data become very demanding, but the manual analysis of 3D speckle fields will be essentially impossible.

Our 3D model of the actin meshwork will not need to be modified. Only the virtual optics will need to be enhanced to generate a stack of images instead of a plain image with the projection of the 3D meshwork onto the focus plane.

In contrast, our speckle extraction scheme will need to be extended to handle the 3D case. This calls for a different approach as the one we are using now, and we might envision methods from, e.g., scale-space theory.

Additionally, capabilities for the parallel analysis of two fluorescence channels might be developed for e.g. parallel analysis of F-actin meshwork and microtubules at the leading edge of motile cells.

But these are only a few suggestions.

We are just at the beginning.

References

- Abercrombie, M., J. E. Heaysman, and S. M. Pegrum. 1972. Locomotion of fibroblasts in culture. V. Surface marking with concanavalin A. *Exp Cell Res.* 73:536-539
- Abercrombie, M. 1980. The crawling movement of metazoan cells. *Proc. R. Soc. London B Biol. Sci.* 207: 129-147
- Abraham, V. C., V. Krishnamurthi, D. Lansing Taylor, and F. Lanni. 1999. The Actin-Based Nanomachine at the Leading Edge of Migrating Cells. *Biophys. J* 77:1721-1732
- Alberts, B., A. Johnson, J. Lewis, M., Raff, K. Roberts, and P. Walter. 2002. *Molecular biology of the cell*. New York: Garland Science
- Anderson, K., Y. Wang, and J. V. Small. 1996. Coordination of protrusion and translocation of the keratocyte involves rolling of the cell body. *J. Cell Biol.* 134(5):1209-1218
- Bagrodia, S. and R. A. Cerione. 1999. PAK to the future. *Trends Cell Biol.* 9, 350-355
- Ballestrem, C., B. Wehrle-Haller, B. Hinz, and B. A. Imhof. 2000. Actin-dependent lamellipodia formation and microtubule-dependent tail retraction control-directed cell migration. *Mol. Biol. Cell* 11:2999-3012
- Beckerle, M. C. 1998. Spatial Control of Actin Filament Assembly: Lessons from Listeria. *Cell.* 95:741-748
- Blanchoin, L., K. J. Amann, H. N. Higgs, J.-B. Marchand, D. A. Kaiser, and T. D. Pollard. 2000. Direct observation of dendritic actin filament networks nucleated by Arp2/3 complex and WASP/Scar proteins. *Nature* 404:1007-1011
- Bloom, K. 1993. The centromere frontier: kinetochore components, microtubule-based motility, and the CEN-value paradox. *Cell* 73:621-624
- Boquet, I., R. Boujema, M.-F. Carlier and T. Pr eat. 2000. Ciboulot Regulates Actin Assembly during Drosophila Brain Metamorphosis. *Cell.* 102:797-808
- Borisy, G. G. and T. M. Svitkina. 2000. Actin machinery: pushing the envelope. *Curr. Opin. Cell Biol.* 12:104-112
- Bray, D. and J. G. White. 1988. Cortical Flow in Animal Cells. *Science.* 239(4842):883-888
- Brust-Mascher, I. and J. M. Scholey (2002). Microtubule Flux and Sliding in Mitotic Spindles of Drosophila Embryos. *Mol. Biol. Cell* 13(11):3967-3975

- Bulinski, J. C., D. J. Odde, B. J. Howell, E. D. Salmon, and C. M. Waterman-Storer. 2001. Rapid dynamics of the microtubule binding of ensconsin in vivo. *J Cell Sci* 114(21):3885-3897
- Cameron, L. A., P. A. Giardini, F. S. Soo, and J. A. Theriot. 2000. Secrets of actin-based motility revealed by a bacterial pathogen. *Nat Rev Mol Cell Biol* 1: 110-119
- Carlier, M.-F., F. Ressad, and D. Pantaloni. 1999. Control of actin dynamics in cell motility. *The Journal of Biological Chemistry* 274(48):33827-33830
- Caspi, A., O. Yeger, I. Grosheva, A. D. Bershadsky, and M. Elbaum. (2001). A New Dimension in Retrograde Flow: Centripetal Movement of Engulfed Particles. *Biophys. J.* 81(4):1990-2000
- Chang S., T. M. Svitkina, G. G. Borisy, and S. V. Popov. 1999. Speckle microscopic evaluation of microtubule transport in growing nerve processes. *Nat. Cell Biol.* 1(7):399-403
- Cheezum, M. K., W. F. Walker, and W. H. Guilford. 2001. Quantitative Comparison of Algorithms for Tracking Single Fluorescent Particles. *Biophys. J.* 81(4):2378-2388
- Cheney, R. E., M. A. Riley, and M. S. Mooseker. 1993. Phylogenetic analysis of the myosin superfamily. *Cell Motil. Cytoskel.* 24:215-223
- Condeelis, J. S., J. B. Wyckoff, M. Bailly, R. Pestell, D. Lawrence, J. Backer, and J. E. Segall. 2001. Lamellipodia in invasion. *Cancer Biol.* 11:119 - 128
- Corpetti, T., E. Memin, and P. Perez. 2002. Dense estimation of fluid flows. *IEEE Trans Pattern Analysis Machine Intelligence* 24(3):365-380
- Cramer, L.P. 1999. Role of actin-filament disassembly in lamellipodium protrusion in motile cells revealed using the drug jasplakinolide. *Curr Biol.* 9:1095 - 1105
- Cramer, L. P. 1997. Molecular mechanics of actin-dependent retrograde flow in lamellipodia of motile cells. *Frontiers in Bioscience* 2:d260-27
- Csucs, G., R. Michel, J. W Lussi, M. Textor, G. Danuser. 2003. Microcontact printing of novel co-polymers in combination with proteins for cell-biological applications. *Biomaterials.* 24(10):1713-1720
- Cunningham, C. C., J. B. Gorlin, D. J. Kwaitkowski, J. H. Hartwig, P. A. Janmey, H. R. Byers, and T. P. Stossel. 1992. Actin-binding protein requirement for cortical stability and efficient locomotion. *Science.* 255:325-327
- Daniels, R. H. and G. M. Bokoch. 1999. p21-activated protein kinase: a crucial component of morphological signaling? *Trends Biochem. Sci.* 24:350-355

- Danuser, G. and C. M. Waterman-Storer. 2003. Fluorescent speckle microscopy: where it came from and where it is going. *J Microsc.* 211(3):191-207
- Danuser, G. 2000. Tracking differential interference contrast diffraction line images with nanometre sensitivity. *J. Microsc.* 198(1):34-53
- Danuser, G. and R. Oldenbourg. 2000. Probing F-actin flow by tracking shape fluctuations of radial bundles in lamellipodia of motile cells. *Biophys. J.* 79:191-201
- Desai, A. and T. J. Mitchison 1997. Microtubule Polymerization Dynamics. *Annu. Rev. Cell Dev. Biol.* 13(1):83-117
- Desai, A., P. S. Maddox, T. J. Mitchison, and E. D. Salmon. 1998. Anaphase A chromosome movement and poleward spindle microtubule flux occur At similar rates in *Xenopus* extract spindles. *J Cell Biol.* 141(3):703-13
- Fechheimer, M. and S. Zigmond. 1993. Focusing on unpolymerized actin. *J. Cell Biol.* 123(1):1-5.
- Fischer, R. S., K. L. Fritz-Six, and V. M. Fowler. 2003. Pointed-end capping by tropomodulin3 negatively regulates endothelial cell motility. *J. Cell Biol.* 161(2):371-380
- Forscher, P. and S. J. Smith. 1988. Actions of cytochalasins on the organization of actin filaments and microtubules in a neuronal growth cone. *J. Cell Biol.* 107:1505-1516
- Frischknecht, F. and M. Way. 2001. Surfing pathogens and the lessons learned for actin polymerization. *Trends Cell Biol.* 11:30-38
- Garcia, M. and D. W. Cleveland. 2001. Going new places using an old MAP: tau, microtubules and human neurodegenerative disease. *Curr. Opin. Cell. Biol.* 13:41 – 48
- Glacy, S. D. 1983. Subcellular distribution of rhodamine-actin microinjected into living fibroblastic cells. *J. Cell Biol.* 97: 1207-1213
- Goldberg, A. V. 1997. An Efficient Implementation of a Scaling Minimum-Cost Flow Algorithm. *J. Algorithms* 22:1-29
- Goode, B. L., A. A. Rodal, G. Barnes, and D. G. Drubin. 2001. Activation of the Arp2/3 Complex by the Actin Filament Binding Protein Abp1p. *J. Cell Biol.* 153:627-34
- Goodson, H. V. 1994. Molecular evolution of the myosin superfamily: application of phylogenetic techniques to cell biological questions. *Soc. Gen. Physiol. Ser.* 49:141-157
- Grant, I. 1997. Particle image velocimetry: A review. *Proc. Inst. of Mechanical Engineering, Part C. J. of Mechanical Engineering Science* 211:55-76

- Grego, S., V. Cantillana, and E. D. Salmon. 2001. Microtubule treadmilling in vitro investigated by fluorescence speckle and confocal microscopy. *Biophys. J.* 81(1):66-78
- Gupton, S. L., W. C. Salmon, and C. M. Waterman-Storer. 2002. Converging populations of F-actin promote breakage of associated microtubules to spatially regulate microtubule turnover in migrating cells. *Curr. Biol.* 12:1891-1899
- Hahne, P., A. Sechi, S. Benesch, J. V. Small. 2001. Scar/WAVE is localised at the tips of protruding lamellipodia in living cells. *FEBS Lett.* 492(3):215-220
- Hall, A. 1998. Rho GTPases and the actin cytoskeleton. *Science* 279:509-514
- Harris, A.K. 1999. A dozen questions about how tissue cells crawl. *Biochem Soc Symp.* 65:315-341
- Haussecker, H. W and D. J. Fleet. 2001. Computing Optical Flow with Physical Models of Brightness Variation. *IEEE Trans. Pattern Analysis Machine Intelligence* 23(6):661-673
- Hug, C., P. Y. Jay, I. Reddy, J. G. McNally, P. C. Bridgman, E. L. Elson, and J. A. Cooper. 1995. Capping protein levels influence actin assembly and cell motility in Dictyostelium. *Cell.* 81:591-600
- Inoué, S. and R. Oldenbourg. 1995. Microscopes. In Handbook of Optics, 2nd Ed., Vol. 2. M. Bass, editor. McGraw-Hill, New York. 17.1-17.52
- Kaksonen, M. H, B. Peng, and H. Rauvala. 2000. Association of cortactin with dynamic actin in lamellipodia and on endosomal vesicles. *J. Cell Sci.* 113:4421-4426
- Kapoor, T. M, and D. A., Compton. 2002. Searching for the middle ground: mechanisms of chromosome alignment during mitosis. *J. Cell Biol.* 157(4):551-556
- Kapoor, T. M. and T. J. Mitchison. 2001. Eg5 is static in bipolar spindles relative to tubulin: evidence for a static spindle matrix. *J Cell Biol.* 154(6):1125-33
- Karsenti, E. and I. Vernos. 2001. The mitotic spindle: a self-made machine. *Science* 294(5542):543-7
- Kessels, M. M., Å. E. Y. Engqvist-Goldstein, and D. G. Drubin. 2000. Association of Mouse Actin-binding Protein 1 (mAbp1/SH3P7), an Src Kinase Target, with Dynamic Regions of the Cortical Actin Cytoskeleton in Response to Rac1 Activation. *Mol. Biol. Cell.* 2000 11:393-412
- Kranewitter, W.J., C. Danninger, and M. Gimona. 2001. GEF at work: Vav in protruding filopodia. *Cell Motil. Cytoskeleton* 49(3):154-160

- Kraynov, V.S., C. Chamberlain, G. M. Bokoch, M. A. Schwartz, S. Slabaugh, and K. M. Hahn. 2000. Localized Rac activation dynamics visualized in living cells. *Science* 290, 333-337
- Labonté, G. 2000. On a neural network that performs an enhanced nearest-neighbour matching. *Pattern Analysis & Applications*. 3:267-278. Springer-Verlag London Limited
- Langanger, G., J. de Mey, M. Moeremans, G. Daneels, M. de Brabander, and J. V. Small. 1984. Ultrastructural localization of alpha-actinin and filamin in cultured cells with the immunogold staining (IGS) method. *J. Cell Biol.* 99:1324-1334
- Lanni, F. 1993. Feedback-stabilized focal-plane control for light microscopes. *Rev. Sci. Instr.* 64:1474-1477
- Lauffenburger, D. A. and A. F. Horwitz. 1996. Cell Migration: A Physically Integrated Molecular Process. *Cell* 84:359-369
- Lin, C. H. and P. Forscher. 1995. Growth cone advance is inversely proportional to retrograde *F-actin* flow. *Neuron* 14:763-771
- Maddox, P. S., K. S. Bloom, and E. D. Salmon. 2000. The polarity and dynamics of microtubule assembly in the budding yeast *Saccharomyces cerevisiae*. *Nat. Cell Biol.* 2(1):36-41
- Maddox, P. S., B. Moree, J. C. Canman, and E. D. Salmon. 2003. A spinning disk confocal microscope system for rapid high resolution, multimode, fluorescence speckle microscopy and GFP imaging in living cells. In, *Biophotonics*, Parts, A and B. G. Marriot and I. Parker, editors. Academic Press, San Diego, CA. And *Methods in Enzymology*. 2003. Vol. 360:597-617
- Machesky, L. M. and R.H. Insall. 1998. Scar1 and the related Wiskott–Aldrich syndrome protein, WASP, regulate the actin cytoskeleton through the Arp2/3 complex. *Curr. Biol.* 8:1347-1356
- Margolis, R. L and L. Wilson. 1991. Microtubule treadmills - possible molecular machinery. *Nature* 293(5835):705-711
- Michaelson, D., J. Silletti, G. Murphy, P. D'Eustachio, M. Rush, and M. R. Philips. 2001. Differential localization of Rho GTPases in live cells: regulation by hypervariable regions and RhoGDI binding. *J. Cell Biol.* 152:111-126
- Mikhailov, A.V. and G.G. Gundersen. 1995. Centripetal transport of microtubules in motile cells. *Cell Motil. Cytoskeleton.* 32:173-186

- Miki, H., H. Yamaguchi, S. Suetsugu, and T. Takenawa. 2000. IRSp53 is an essential intermediate between Rac and WAVE in the regulation of membrane ruffling. *Nature* 408:732-735
- Miki, H., S. Suetsugu, and T. Takenawa. 1998. WAVE, a novel WASP-family protein involved in actin reorganization induced by Rac. *EMBOJ.* 17:6932-6941
- Mitchison, T. J. 1989. Polewards microtubule flux in the mitotic spindle: evidence from photoactivation of fluorescence. *J Cell Biol.* 109(2):637-52
- Mitchison, T. J. and E. D. Salmon. 1992. Poleward kinetochore fiber movement occurs during both metaphase and anaphase-A in newt lung cell mitosis. *J. Cell Biol.* 119:569-582
- Mitchison, T.J., and L.P. Cramer. 1996. Actin-based cell motility and cell locomotion. *Cell.*84:371-379
- Mitchison, T. J. and Salmon, E. D. 2001. Mitosis: a history of division. *Nat. Cell Biol.* 3(1):E17-21
- Mogilner, A. and L. Edelstein-Keshet. 2002. Regulation of Actin Dynamics in Rapidly Moving Cells: A Quantitative Analysis. *Biophys. J.* 83(3):1237-1258
- Mogilner, A. and G. Oster. 1996. Cell motility driven by actin polymerization. *Biophys J.* 71(6):3030-45
- Moon, A. and D. G. Drubin. 1995. The ADF/cofilin proteins: stimulus-responsive modulators of actin dynamics. *Mol. Biol. Cell* 6:1423-1431
- Moritz, H. 1973. Least Squares Collocation. Deutsche Geodätische Kommission. Reihe A: Theoretische Geodäsie. Heft Nr. 75. München.
- Murray, A. W., A. B. Desai, and E. D. Salmon. 1996. Real time observation of anaphase in vitro. *Proc. Natl. Acad. Sci. Am.* 93(22):12327-12332
- Nakagawa, H., H. Miki., M. Ito, K. Ohashi, T. Takenawa, and S. Miyamoto. 2001. N-WASP, WAVE and Mena play different roles in the organization of actin cytoskeleton in lamellipodia. *J. Cell Sci.* 114:1555-1565
- Nobes, C. D. and A. Hall. 1995. Rho, Rac, and Cdc42 GTPases regulate the assembly of multimolecular focal complexes associated with actin stress fibers, lamellipodia, and filopodia. *Cell* 81:53-62
- Oshiro, M. 1998. Cooled CCD Versus Intensified Cameras for Low-Light Video – Applications and Relative Advantages. *Methods in Cell Biology.* Vol. 56:45-62
- Pantaloni, D., C. Le Clainche, M.-F. Carrier. 2001. Mechanism of actin-based motility. *Science.* 292:1502-1506

- Pantaloni, D., R. Bujemaa, D. Didry, P. Gounon, and M.-F. Carrier. 2000. The Arp2/3 complex branches filament barbed ends: functional antagonism with capping proteins. *Nat. Cell Biol.* 2(7):385-391
- Papoulis, A. 1991. Probability, Random Variables, and Stochastic Processes, 3rd Edition, McGraw-Hill International Editions, New York
- Perez, F., G. S. Diamantopoulos, R. Stalder, and T. E. Kreis. 1999. CLIP-170 highlights growing microtubule ends in vivo. *Cell* 96(4):517-27
- Perlman, Z. E., Kapoor, T. M., and T. J. Mitchison. 2001. Automated analysis of flux in fluorescent speckled mitotic spindles. *Biophys. J.* 80(1):2571 Part 2
- Pollard, T. D. and J. A. Cooper. 1984. Quantitative analysis of the effect of Acanthamoeba profilin on actin filament nucleation and elongation. *Biochemistry* 23, 6631-6641
- Pollard, T. D. 1986. Rate constants from the reactions of ATP-actin and ADP-actin with the ends of actin filaments. *J. Cell Biol.* 103:2747-2754
- Pollard, T. D., L. Blanchoin, and R. D. Mullins. 2000. Molecular mechanisms controlling actin filament dynamics in nonmuscle cells. *Annu. Rev. Biophys. Biomol. Struct.* 29:545-76
- Ponti A., Valotton P., Salmon W.C., Waterman-Storer C.M. and Danuser G. 2003. Computational Analysis of f-Actin Turnover in Cortical Actin Meshworks using Fluorescent Speckle Microscopy. *Biophys. J.* 84:3336-3352
- Price, L.S., J. Leng, M. A. Schwartz, and G. M. Bokoch. 1998. Activation of Rac and Cdc42 by integrins mediates cell spreading. *Mol. Biol. Cell* 9:1863-1871
- Pring, M., L. Cassimeris, and S. H. Zigmond. 2002. An unexplained Sequestration of Latrunculin A is Required in Neutrophils for Inhibition of Actin Polymerization. *Cell Motil Cytoskeleton.* 52:122-130
- Ridley, A. J. 2001. Rho family proteins: coordinating cell responses. *Trends Cell Biol.* 11:471-477
- Rieder, C. L. and R. H. Hard. 1990. Newt lung epithelial cells: cultivation, use and advantages for biomedical science. *Int. Rev. Cytol.* 122:153-220
- Rousseeuw, P. and A. M. Leroy. 1987. Robust Regression and Outlier Detection. New York: John Wiley & Sons
- Safer, D. and V. T Nachmias. 1994. Beta thymosins as actin binding peptides. *Bioessays* (invited review) 16:473-479

- Salmon, E. D., S. L. Shaw, J. Waters, C. M. Waterman-Storer, P. S. Maddox, E. Yeh, and K. Bloom. 1998. A high-resolution multimode digital microscope system. *Meth. Cell Biol.* 56:185-215
- Salmon, W. C., M. C. Adams, and C. M. Waterman-Storer. 2002. Dual-wavelength fluorescent speckle microscopy reveals coupling of microtubule and actin movements in migrating cells. *J. Cell Biol.* 158:31-37
- Sase, I., H. Miyata, J. E. Corrie, J. S. Craik, and K. Kinosita Jr. 1995. Real time imaging of single fluorophores on moving actin with an epifluorescence microscope. *Biophys. J.* 69(2):323-328
- Sawin, K. E. and T. J. Mitchison. 1991. Poleward microtubule flux mitotic spindles assembled in vitro. *J Cell Biol.* 112:941-954
- Sawin, K. E. and T. J. Mitchison. 1994. Microtubule Flux in Mitosis Is Independent of Chromosomes, Centrosomes, and Antiparallel Microtubules. *Mol. Biol. Cell* 5(2):217-226
- Schaefer, A. W., N. Kabir, and P. Forscher. 2002. Filopodia and actin arcs guide the assembly and transport of two populations of microtubules with unique dynamic parameters in neuronal growth cones. *J. Cell Biol.* 158(1):139-52
- Schafer, D. A. 2002. Coupling actin dynamics and membrane dynamics during endocytosis. *Curr. Opin. Cell. Biol.* 14(1):76-81
- Scita, G., P. Tenca, E. Frittoli, A. Tocchetti, M. Innocenti, G. Giardina, and P. P. Di Fiore. 2000. Signaling from Ras to Rac and beyond: not just a matter of GEFs. *EMBOJ.* 19:2393-2398
- Sedgewick, R. 2002. Algorithms in C++, Graph algorithms: Addison-Wesley
- Sethi, J. K. and R. Jain. 1987. Finding Trajectories of Feature Points in a Monocular image sequence. *IEEE Trans Pattern Analysis Machine Intelligence* 9(1):56-73
- Sharp, D. J., G. C. Rogers, and J. M. Scholey. 2000. Microtubule motors in mitosis. *Nature* 407:41-46
- Small, V. 1981. Organization of actin in the leading edge of cultured cells. *J. Cell Biol.* 91:695-705
- Spector, I., N. R. Shochet, Y. Kashman, A. Groweiss. 1983. Latrunculins: novel marine toxins which disrupt microfilament organization in cultured cells. 1983. *Science.* 214:493-495

- Stradal, T., K. D. Courtney, K. Rottner, P. Hahne, J. V. Small, and A. M. Pendergast. 2001. The Abl interactor proteins localize to sites of actin polymerization at the tips of lamellipodia and filopodia. *Curr. Biol.* 11:891-895
- Straight, A. F., A. Cheung, J. Limouze, I. Chen, N. J. Westwood, J. R. Sellers, and T. J. Mitchison. 2003. Dissecting temporal and spatial control of cytokinesis with a myosin II inhibitor. *Science* 299(5612):1743-1747
- Sun, H. Q., K. Kwiatkowska, D. C. Wooten, and H. L. Yin. 1995. Effects of CapG overexpression on agonist-induced motility and second messenger generation. *J. Cell Biol.* 129(1):147-156
- Svitkina, T. M., A. B. Verkhovsky, K. M. McQuade, and G. G. Borisy. 1997. Analysis of the Actin-Myosin II System in Fish Epidermal Keratocytes: Mechanism of Cell Body Translocation. *J. Cell Biol.* 139(2):397-415
- Svitkina, T. M. and G. G. Borisy. 1999. Arp2/3 Complex and Actin Depolymerizing Factor/Cofilin in Dendritic Organization and Treadmilling of Actin Filament Array in Lamellipodia. *J. Cell Biol.* 145(5):1009-1026
- Theriot, J. A. and T. J. Mitchison. 1991. Actin microfilament dynamics in locomoting cells. *Nature* 352:126-131
- Theriot, J. A., J. Rosenblatt, D. A. Portnoy, P. J. Goldschmidt-Clermont, and T. J. Mitchison. 1994. Involvement of profilin in the actin-based motility of L-Monocytogenes in cells and in cell free extracts. *Cell* 76(3):505-517
- Theriot, J. A. 1997. Accelerating on a Treadmill: ADF/Cofilin Promotes Rapid Actin Filament Turnover in the Dynamic Cytoskeleton. *J. Cell Biol.* 136(6):1165-1168
- Thiery, J. P. and D. Chopin. 1999. Epithelial cell plasticity in development and tumor progression. *Cancer Metastasis Rev.* 18(1):31-42
- Thomann D., D. Rines, P. Sorger, and G. Danuser. 2002. Automatic fluorescent tag detection in 3D with super-resolution: application to the analysis of chromosome movement. *J. Microscopy.* 208:49-64
- Tseng, Y. and D. Wirtz. 2001. Mechanics and Multiple-Particle Tracking Microrheology of alpha-Actinin-Cross-Linked Actin Filament Networks. *Biophys. J.* 81:1643-1656
- Vallotton, P., A. Ponti, C. M., Waterman-Storer, E. D. Salmon, and G. Danuser. 2003a. Recovery, visualization, and analysis of actin and tubulin polymer flow in live cells: A Fluorescent Speckle Microscopy study. *Biophys. J.* 85(2):1289-1306

- Vallotton, P., C. M. Waterman-Storer, and G. Danuser. 2003b. Computational fluorescent speckle microscopy: A new window on actin cytoskeleton dynamics in motile cells. In revision for Proc Natl Acad Sci USA
- Van Aelst, L. and C. D'Souza-Schorey. 1997. Rho GTPases and signaling networks. *Genes Dev.* 11:2295-2322
- Van der Flier, A. and A. Sonnenberg. 2001. Structural and functional aspects of filamins. *Biochim. Biophys. Acta.* 1538:99-117
- Veenman, C. J., M. J. T. Reinders, and E. Backer. 2001. Resolving motion correspondence for densely moving points. *IEEE Trans. Pattern Analysis Machine Intelligence* 23(1):54-72
- Verkhovsky, A. B., T. M. Svitkina and G. G. Borisy. 1999a. Network contraction model for cell translocation and retrograde flow. *Cell Behaviour: Control and Mechanism of Motility.* London, PORTLAND PRESS LTD:207-222
- Verkhovsky, A. B., T. M. Svitkina, and G. G. Borisy 1999b. Self-polarization and directional motility of cytoplasm. *Curr Biol.* 9(1):11-20
- Vicker, M. G. 2000. Reaction-diffusion waves of actin filament polymerization / depolymerization in Dictyostelium pseudopodium extension and cell locomotion. *Biophysical Chemistry* 84:87-98
- Wadsworth, P. and E. D. Salmon. 1986. Analysis of the treadmilling model during metaphase of mitosis using fluorescence redistribution after photobleaching. *J. Cell Biol.* 102(3): 1032-1038
- Wang, Y. L., J. M. Heiple, and D. L. Taylor. 1982. Fluorescent analog cytochemistry of contractile proteins. *Methods Cell Biol.* 25:1-11
- Wang, Y.L. 1985. Exchange of actin subunits at the leading edge of living fibroblasts: possible role of treadmilling. *J. Cell. Biol.* 101:597-602
- Watanabe N. and T.J. Mitchison. 2002. Single-molecule speckle analysis of actin filament turnover in lamellipodia. *Science.* 295:1083-1086
- Waterman-Storer, C.M. Fluorescent speckle microscopy (FSM) of microtubules and actin in living cells. *Current Protocols in Cell Biology*, J.S. Bonifacino, M. Dasso, J.B. Harford, J. Lippincott-Schwartz, and K.M. Yamada, editors. John Wiley & Sons, New York. 1:4.10.1-4.10.26
- Waterman-Storer C. M. 2002. Fluorescent speckle microscopy (FSM) of microtubules and actin in living cells. *Current Protocols in Cell Biology.* NY. John Wiley, NY

- Waterman-Storer, C. M. and G. Danuser. 2002. New Directions in Applications and Quantitative Analysis for Fluorescent Speckle Microscopy. *Curr. Biol.* 12:R633-640.
- Waterman-Storer, C. M., W. C. Salmon, and E. D. Salmon. 2000a. Feedback interactions between cell-cell adherens junctions and cytoskeletal dynamics in newt lung epithelial cells. *Mol. Biol. Cell* 11:2471-2483
- Waterman-Storer, C. M., D. Y. Duey, K. L. Weber, J. Keech, R. E. Cheney, E. D. Salmon, and W. M. Bement. 2000b. Microtubules remodel actomyosin networks in *Xenopus* egg extracts via two mechanisms of F-actin transport. *J. Cell Biol.* 150:361-376
- Waterman-Storer, C. M., A. Desai, J. C. Bulinski, and E. D. Salmon. 1998. Fluorescent speckle microscopy: visualizing the movement, assembly, and turnover of macromolecular assemblies in living cells. *Curr. Biol.* 8:1227-1230
- Waterman-Storer, C. M. and E. D. Salmon. 1997. Actomyosin-based retrograde flow of microtubules in the lamella of migrating epithelial cells influences microtubule dynamic instability and turnover and is associated with microtubule breakage and treadmilling. *J. Cell Biol.* 139:417-434
- Waterman-Storer, C.M. and E.D. Salmon. 1998. How microtubules get fluorescent speckles. *Biophys J.* 75:2059-2069
- Waterman-Storer, C. M. and E. D. Salmon. 1999. Fluorescent speckle microscopy of microtubules: how long can you go? *FASEB J.* 13 (Suppl):S225-S230
- Waterman-Storer, C. M., J. W. Sanger, J. M. Sanger. 1993. Dynamics of organelles in the mitotic spindle of living cells: membrane and microtubule interactions. *Cell Motil. Cytoskeleton.* 26:19-39
- Weaver, A. M., A. V. Karginov, A. W. Kinley, S. A. Weed, Y. Li, J. T. Parsons, and J. A. Cooper. 2001. Cortactin promotes and stabilizes Arp2/3-induced actin filament network formation. *Curr. Biol.* 11:370-374
- Welch, M. D., J. Rosenblatt, J. Skoble, D. A. Portnoy, and T. J. Mitchison. 1998. Interaction of human Arp2/3 complex and the *Listeria monocytogenes* ActA protein in actin filament nucleation. *Science* 281:105-108
- Welch, M. D., A. Iwamatsu, and T. J. Mitchison. 1997. Actin polymerization is induced by Arp2/3 protein complex at the surface of *Listeria monocytogenes*. *Nature* 385:265-269
- Wesselman, J. P. and J. G. De Mey. 2002. Angiotensin and cytoskeletal proteins: role in vascular remodeling. *Curr. Hypertens. Rep.* 4(1):63-70

- Westphal, R. S., S. H. Soderling, N. M. Alto, L. K. Langeberg, and J. D. Scott. 2000. Scar/WAVE-1, a Wiskott–Aldrich syndrome protein, assembles an actin-associated multi-kinase scaffold. *EMBOJ.* 19:4589-4600
- Wiesner, S., E. Helfer, D. Didry, G. Ducouret, F. Lafuma, M.-F. Carlier, and D. Pantaloni. 2003. A biomimetic motility assay provides insight into the mechanism of actin-based motility. *J. Cell Biol.* 160(3):387-398
- Wittmann, T., and C.M. Waterman-Storer. 2001a. Cell motility: can Rho GTPases and microtubules point the way? *J. Cell Sci.* 114:3795-3803
- Wittmann, T., A. Hyman, and A. Desai. 2001b. The spindle: a dynamic assembly of microtubules and motors. *Nat. Cell Biol.* 3(1):E28-E34
- Wittmann, T., G. M. Bokoch, and C. M. Waterman-Storer. 2003. Regulation of leading edge microtubule and actin dynamics downstream of Rac1. *J. Cell Biol.* 161:845-851
- Wolf, D. E. 1989. Designing, building, and using a fluorescence recovery after photobleaching instrument. *Meth. Cell Biol.* 30: 271-306
- Yarmola, E. G, T. Somasundaram, T. A. Boring, I. Spector, M.R. Rubb. 2000. Actin-latrunculin A structure and function – Differential modulation of actin-binding protein function by latrunculin A. *J. Biol. Chem.* 275:28120-28127
- Zettl, M. and M. Way. 2001. New tricks for an old dog? *Nat. Cell Biol.* 3: E74–E75
- Zhai, Y, P. J. Kronenbusch, and G. G. Borisy. 1995. Kinetochore microtubule dynamics and the metaphase-anaphase transition. *J. Cell Biol.* 131:721-734

Supplementary data

The previous chapters refer to 5 supplementary movies, which were submitted for publication along with the manuscripts. The interested reader may request them at the following e-mail address: gdanuser@scripps.edu.

Chapter 3

actinFlow.mov

Left panel: movie of F-actin flow at the front edge of a migrating newt lung epithelial cell, generated from a time lapse series of FSM raw images captured at 10 s intervals. Right panel: the same movie after subtraction of the signal of all speckles exploited for flow recovery.

spindleFlow.mov

Left panel: movie of microtubule flux in a mitotic spindle of *Xenopus* egg extracts, generated from a time lapse series of FSM raw images captured at 10 s intervals. Right panel: the same movie after subtraction of the signal of all speckles exploited for flow recovery.

Chapter 4

M1.avi

Movie size: 500 x 500 pixels (original size). Movie frame rate: 5 s⁻¹. Experimental sampling interval: 10 s. Total experiment duration: 740 s.

M2.avi

Movie size: 264 x 348 pixels (25% of the original size), frame rate: 5 s⁻¹. Experimental sampling interval: 10 s. Total experiment duration: 590 s.

M3.avi

Movie size: 228 x 172 pixels (25% of the original size), frame rate: 5 s⁻¹. Experimental sampling interval: 10 s. Total experiment duration: 890 s.

C1.avi

Movie size: 200 x 400 pixels (original size), frame rate: 5 s⁻¹. Experimental sampling interval: 5 s. Total experiment duration: 600 s.

M2kinetic.avi

Animated maps of F-actin turnover in experiment M2, stored at 5 maps/s. Each map relies on speckle events integrated over 10 frames of the original movie.

M2speed.avi

Animated maps of F-actin flow speed in experiment M2, stored at 5 maps/s. Each map relies on speckle trajectories integrated over 10 frames of the original movie.

M2flow.avi

Animated F-actin flow vector fields in experiment M2, stored at 1 map/s. Each map relies on speckle trajectories integrated over 10 frames of the original movie. For space reasons, each movie frame corresponds to 10 successive, non-overlapping time points.

Acknowledgments

When I finished my biology studies at the ETH Zurich I had already collected some experience in the computational approach to biology, but it was only when I met **Gaudenz Danuser** that I decisively put pipettes and Petri dishes aside and started looking at biological problems from the point of view of the modeler and the programmer. Because I had never felt completely comfortable with the classical tools of biology, but in contrast I had had a rather long experience in computer programming, this opportunity was for me the best way to combine knowledge, skills, and fun. I am grateful to Gaudenz for the great opportunity he gave me when he accepted me in his group – which was one of the first real interdisciplinary groups at the ETH Zurich – and allowed me to enter a field which is gaining increasing importance as scientists all over the world start realizing that the future of science is in the unified efforts from natural and technical sciences. Of course, I thank Gaudenz also for his help, advice, and brain, without which this work would not have been possible (or at least only partially).

The second person I would like to profoundly thank is **Clare Waterman-Storer**, who – in the unlikely case she needs to be introduced – is associate professor at the department of cell biology at the Scripps Research Institute in San Diego, CA. FSM is her baby, and the enthusiasm she puts in her research is matched probably only by Gaudenz's. I spent three great weeks working at her lab during my Ph. D. and I liked it so much that I'm moving there for a post-doctoral position in a few weeks.

The third, important *thank you* goes to **Wendy Salmon**, who used to work in Clare's lab and whose FSM skills were (slightly) inferior only to Clare's. Wendy is one of the reasons why FSM has become that good over the last few years. She assured a constant input of great data analyzing which our software could only get better.

Many other people need to be thanked. My friends and colleagues of BMMG and the Laboratory for Biomechanics, all the people who collaborated actively with me during my Ph. D (some of them pop up as authors in my articles). **Luca Baldini** for his implementation of the collocation method but mostly for the intense *Töggele* matches (just kidding). All the friends outside my current scientific environment, my parents, who are highly responsible for most I have been doing throughout my life having put me on this planet, and – yes, my brother.

Curriculum vitae

Education

- 2000 – 2003** Ph. D. at the BioMicroMetrics Group, Department of Mechanical and Process Engineering, ETH Zurich
- 1999** M. Sc. in biotechnology (Dipl Natw.) ETH Zurich
- 1994 – 1999** ETH Zurich, faculty of biology
- 1990 – 1994** High School in Trevano (TI)

Continued Education

- 2001** EMBO Course: “Microinjection and detection of probes in cells” at EMBL, Heidelberg (Germany)

Research and Professional Experience

- 2000-2003** Ph. D. project: High-Resolution Analysis of F-Actin Meshwork Kinetics and Kinematics using Computational Fluorescent Speckle Microscopy
- 2000** HTML programmer, at CREALOGIX AG, Rosengartenstrasse 6, CH-8608 Bubikon, Switzerland
- 2000** Matlab programmer, at the Institute of theoretical computer science, ETH Zurich
- 1998 – 1999** Diploma thesis at the Institute of Biotechnology, ETH Zurich
Metabolic flux analysis in Escherichia coli augmented by mass spectrometry
- 1997** Semester work at the Institute of Biotechnology, ETH Zurich

Publications

Full papers

Vallotton P., **Ponti A.**, Waterman-Storer C.M., Salmon E.D., and Danuser G. Recovery, visualization, and analysis of actin and tubulin polymer flow in live cells: A Fluorescent Speckle Microscopy study, *Biophys J.* 85: 1289–1306

Ponti A., Vallotton P., Salmon W.C., Waterman-Storer C.M. and Danuser G. 2003. Computational Analysis of f-Actin Turnover in Cortical Actin Meshworks using Fluorescent Speckle Microscopy. *Biophys J.* 84:3336–3352

Emmerling, M., Dauner, M., **Ponti, A.**, Fiaux, J., Hochuli, M., Szyperski, T., Wüthrich, K., Bailey, J. E., Sauer, U. 2002. Metabolic Flux Responses to Pyruvate Kinase Knockout in *Escherichia coli*. *J. Bacteriol.* 152-164

Papers in review

Ponti A., Matov A., Waterman-Storer C. M., and Danuser G. Computational Fluorescent Speckle Microscopy II: High-Resolution Co-Mapping of F-Actin Flow and Turnover in Migrating Cells. Submitted to *Biophys J*

Conference papers

Ponti, A., Csucs, G., Waterman-Storer, C.M., Danuser, G., Measurement of f-actin assembly and turnover in vivo by fluorescent speckle microscopy (FSM). *Biophys. J.* 82(1):176a, 2002

Ponti, A., Salmon, W.C, Waterman-Storer C.M., Danuser G., Quantitative fluorescent speckle microscopy (FSM) of actin polymerization/depolymerization activity in living cells, *Mol. Biol. Cell.* 12:421a, 2001

Abstracts

Ponti, A., Vallotton, P., Matov, A., Waterman-Storer, C. M., Salmon, E. D., Danuser, G. Computational Fluorescence Speckle Microscopy. Biophysical Society, 47th Annual Meeting, San Antonio, TX, March 1-3, 2003

Ponti, A., Csucs, G., Waterman-Storer, C. M., Danuser, G.. Measurement of F-actin assembly and turnover in vivo by fluorescent speckle microscopy (FSM). Biophysical Society, 46th Annual Meeting, San Francisco, CA, February 23-27, 2002

Ponti, A., Salmon, W. C., Waterman-Storer, C. M., Danuser, G.. Lamellipodial actin dynamics measured by fluorescence speckle microscopy. The American Society for Cell Biology, 41st Annual Meeting, Washington, DC, December 8-12, 2001

Ponti, A., Salmon, W. C., Waterman-Storer, C. M., Danuser, G.. Quantitative Fluorescent Speckle Microscopy of Lamellipodial Actin Meshwork Activity: Introduction to a generic framework for speckle analysis and first results. Gordon Research Conference on “Motile and Contractile Systems”, June 13th 2001, New London, NH

Talks

Ponti, A., Computational Fluorescence Speckle Microscopy (cFSM), Joining Forces: Intersections between Biology, Chemistry, Engineering and Informatics, Mini-Symposium ETH Zurich, March 18th, 2003, Zurich

